Preparation and Characterization of $Y\ Ba_2\ Cu_3\ O_{7-X}$ High – T_C Superconductor

by

Mohammed Abdel-Raouf Redwan

A Thesis Presented to the

FACULTY OF THE COLLEGE OF GRADUATE STUDIES

KING FAHD UNIVERSITY OF PETROLEUM & MINERALS

DHAHRAN, SAUDI ARABIA

In Partial Fulfillment of the
Requirements for the Degree of

MASTER OF SCIENCE

In

PHYSICS

July, 1991

Order Number 1354112

Preparation and characterization of $YBa_2Cu_3O_{7-x}$ high-T_c superconductor

Redwan, Mohammed Abdel-Raouf, M.S.

King Fahd University of Petroleum and Minerals (Saudi Arabia), 1991

U·M·I
300 N. Zeeb Rd.
Ann Arbor, MI 48106

PREPARATION AND CHARACTERIZATION OF $Y Ba_2 Cu_3 O_{7-x}$ HIGH-T_c SUPERCONDUCTOR

BY

MOHAMMED ABDEL-RAOUF REDWAN

A Thesis Presented to the

FACULTY OF THE COLLEGE OF GRADUATE STUDIES

KING FAHD UNIVERSITY OF PETROLEUM & MINERALS

DHAHRAN, SAUDI ARABIA

In Partial Fulfillment of the
Requirements for the Degree of

MASTER OF SCIENCE

In

PHYSICS

JULY 1991

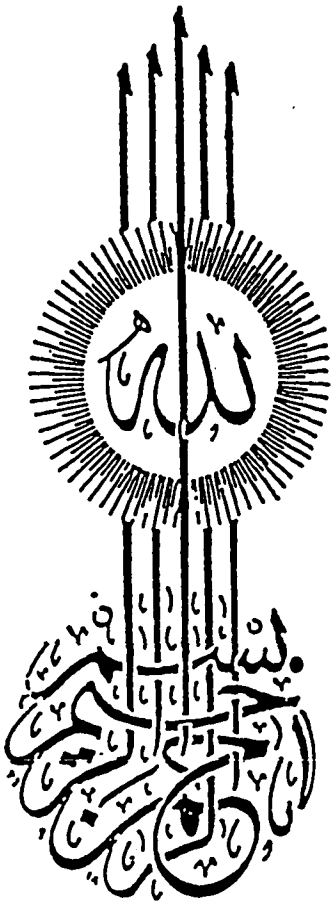

KING FAHD UNIVERSITY OF PETROLEUM & MINERALS

DHAHRAN, SAUDI ARABIA

COLLEGE OF GRADUATE STUDIES

This thesis, written by **MOHAMMED ABD EL-RAOUF REDWAN** *under the direction of his Thesis Advisor, and approved by his Thesis Committee, has been presented to and accepted by the Dean of the College of Graduate Studies, in partial fulfillment of the requirements for the degree of* **MASTER OF SCIENCE IN PHYSICS.**

Thesis Committee

O. B. Dabbousi
Chairman (Professor O. B. DABBOUSI)

Member (Dr. N. A. SALIM) Co-Chairman

E. E. Khawaja
Member (Dr. E. E. KHAWAJA)

A. B Hallak
Member (Dr. A. B. HALLAK)

Zakir Hussain
Member (Dr. Z. HUSSAIN)

Member (Dr. R. AVCI)

Department Chairman

Dean College of Graduate Studies

Date : 20.10.91

إلى والديّ

مع حُبي و تقديري

محمد

To my Parents
With Love and Gratitude

Mohammed

ACKNOWLEDGEMENT

Praise to *"ALLAH"* Lord of the worlds, the ALMIGHTY, with whose gracious help it was possible to accomplish this work and Peace Be Upon Prophet *MOHAMMED*, who encourages us as moslems to seek science wherever it can be found.

Acknowledgement is due to *King Fahd University of Petroleum and Minerals* and the Physics Department for support of this research.

I would like to express my sincere thanks to my thesis advisor *Professor O. B. Dabbousi* and my thesis acting advisor *Dr. M. A. Salim* for their guidance, encouragement and support. I wish also to express my gratefulness to the committee members *Dr. E. E. Khawaja* and *Dr. A. B. Hallak* for their valuable suggestions, helpful remarks and their kind cooperation. Thanks are also due to the other committee members *Dr. Z. Hussain* and *Dr. R. Avci*, for their valuable comments.

Thanks are to *Mr. P. Sobingsobing* for his assistance in the experimental work. Thanks are also to *Mr. N. Hamdan* for the help in analyzing XRD results. Special thanks are to *Dr. D. S. Redwan* for his encouragement and support, and to *Mr. F. M. Al-Shamali* , and other colleagues in the Physics Department.

Finally, my sincere thanks are to my *family*, all my *friends*, and many others for the memorable days we shared together.

TABLE OF CONTENTS

LIST OF TABLES

LIST OF FIGURES

List of Acronyms

AES	Auger Electron Spectroscopy.
BCS	Bardeen-Cooper-Schrieffer (theory).
CAE	Constant Analyzer Energy.
CAT	Constant Analyzer Transmission.
CDW	Charge-Density Wave.
CI	Configuration Interaction.
CRR	Constant Retard Ratio.
DOS	Density of States.
EDC	Energy Distribution Curve.
EPMA	Electron Probe Micro Analysis.
ESCA	Electron Spectroscopy for Chemical Analysis.
I_s/I_m	Ratio of satellite peak intensity (I_s) to the main peak intensity (I_m).
LAPW	Linear Augmented Plane Wave (method).
LDA	Local Density Approximation.
LEED	Low Energy Electron Diffraction.
PES	Photo Electron Spectroscopy.
RVB	Resonating Valence Bonds (model).
TEM	Transmission Electron Microscope.
T_c	Critical transition temperature.
UHV	Ultra-High Vacuum.
UPS	Ultra-violet Photoelectron Spectroscopy.
UV	Ultra-Violet.
VB	Valance Band.
XAES	X-ray induced Auger Electron Spectroscopy.
XRD	X-Ray Diffraction.
XPS	X-Ray Photoelectron Spectroscopy.
Y123	$Y Ba_2 Cu_3 O_{7-x}$, $0 \leq x \leq 1$.

ملخص الرسالة

إسم الطالب : محمد عبدالرؤوف ابراهيم رضوان

عنوان الدراسة : تحضير وتوصيف عينات من مادة $YBa_2Cu_3O_{7-x}$ فائقة الموصلية ذات درجة حرارة حرجة مرتفعة .

التخصص : فيزياء

تاريخ الشهادة : يوليو ١٩٩١م

تم تحضير عينات من مادة $YBa_2Cu_3O_{7-x}$ ذات الموصلية الفائقة بطريقتين مختلفتين . وقد أظهرت القياسات بواسطة حيود الاشعة السينية والمسح المجهري الالكتروني والتحاليل الدقيقة بالمجس الالكتروني وكذلك قياس المقاومة الكهربائية بطريقة المجسات الأربعة ، اظهرت تجانس العينات في تركيبها البللوري ، وانها ذات تركيب بللوري معيني عمودي ، ولها درجة حرارة حرجة تبلغ ٩٢ كلفن .

وتم كذلك دراسة العينات بواسطة مطيافية الالكترونات بالأشعة السينية والأشعة فوق البنفسجية ، حيث حُضرت أسطح نظيفة ممثلة للعينات بإزالة الطبقات السطحية لها في غرفة القياس . وقد أظهرت مطيافية الكترونات نطاق التكافؤ وجود كثافة مستويات الكترونية منخفضة عند مستوى فيرمي (Fermi) ، وتجهين قوي لمستوى الطاقة 2p للاكسجين (O 2p) ومستوى الطاقة 3d للنحاس (Cu 3d). وقد اظهر وضع وشكل وملحقات الإنبعاث (الإنبعاث المرافق) من مستوى 2p للنحاس (Cu 2p) وجود مزيج من حالتي التكافؤ الأحادية (Cu^{1+}) والثنائية (Cu^{2+}) . وأوضح الإنبعاث من مستوى الطاقة 1s للاكسجين (O 1s) وجود مركبتين اصليتين وأن احداهما ذات الطاقة ٥٣١ الكترون فولت تنشأ بسبب وجود فجوة الاكسجين (O^-) . كما ان لانبعاث الالكترونات الداخلية للباريوم (Ba) مركبتان ، مما يُرجح وجود تشكيلين رئيسيين لأكسيد الباريوم (Ba - O) بسبب غياب بعض ذرات الاكسجين في محيطه . ويوضح شكل ووضعية طيف الإنبعاث المزدوج للايتيريوم (Y) التفاعل التبادلي الضعيف بين الايتيريوم والاكسجين (Y - O) .

يُسبب تعريض العينات للتاثير الحراري تحت ظروف التفريغ الفائق زيادة في غياب الاكسجين (O^{2-}) وانخفاضاً في النحاس ثنائي التكافؤ (Cu^{2+}) . كما يؤدي تعريض العينات للماء الى تكوين طبقة سطحية من الهيدروكسيد ، في حين لم يؤدي تعريضها للاكسجين الى اي أثر ملحوظ .

درجة الماجستير في العلوم

جامعة الملك فهد للبترول والمعادن

الظهران - المملكة العربية السعودية

يوليو ١٩٩١م

ABSTRACT

STUDENT NAME : *MOHAMMED ABD EL-RAOUF REDWAN*

TITLE OF STUDY : *PREPARATION AND CHARACTERIZATION OF* $YBa_2Cu_3O_{7-x}$ *HIGH* T_c *SUPERCONDUCTOR.*

MAJOR FIELD : *PHYSICS*

DATE OF DEGREE : *JULY 1991*

Superconductor samples of $YBa_2Cu_3O_{7-x}$ were prepared by two different methods. Measurements using XRD, SEM, EPMA, and four probe method indicated single phased samples with orthorhombic structure and transition temperature of 92 K.

Samples were further studied by XPS and UPS techniques, where representative clean surfaces were prepared by in-situ scraping. Valence band spectra show low density of states at Fermi level and strongly hybridized O 2p and Cu 3d states. The position, shape, and satellite emission of Cu 2p indicate a mixture of Cu^{1+} and Cu^{2+} valencies. The O 1s two components are intrinsic and the 531 eV peak is related to oxygen hole states (O^-). Ba core levels show a two component structure, suggesting two principal Ba-O configurations due to oxygen vacancies. The position and shape of Y doublets indicate weak Y-O interactions.

Annealing in UHV causes an increase in O^{2-} vacuncies and a reduction of Cu^{2+} valency. Water exposure causes the formation of hydroxides at the surface, while oxygen exposure has no significant effect.

MASTER OF SCIENCE DEGREE

KING FAHD UNIVERSITY OF PETROLEUM AND MINERALS

Dhahran, Saudi Arabia

July 1991

CHAPTER 1

INTRODUCTION

The phenomenon of superconductivity is one of the most unusual phenomena of solid-state physics. The vanishing of the resistance in itself is surprising enough, but since it is associated with other equally remarkable effects, superconductivity has been the source of a wealth of experimental and theoretical work.

1.1 Overview

The field of superconductivity began with the discovery of zero resistance by Onnes [1] in 1911, while he was investigating the electrical properties of extremely cold metals. He passed a current through a mercury wire, then measured the resistance of the wire as he chilled it. At 4.2 K the resistance suddenly vanished. He wrote "mercury has passed into a new state, which because of its extraordinary electrical properties may be called the superconductive state". Shortly afterwards the

superconductivity phenomenon was also discovered in other metals such as tin, lead, indium, aluminium, niobium, etc.

Whether the resistance in the superconducting state is really zero, or it is just very small, has become a field of various experimental work. In one key experiment, Onnes started a current flowing in a loop of lead wire cooled to 4 K. A year later the current was still flowing undiminished. File and Mills [2] in 1963, showed that the current life time in a superconducting ring is about 10^5 years.

Until 1933 it was assumed that, zero resistivity was the essential property of superconducting material. In 1933 Meissner and Ochsenfeld [3] showed that, the superconducting state possesses the additional and entirely independent property of excluding all magnetic flux when cooled through the superconducting transition, that is, they are also perfect diamagnets. This phenomenon is called the Meissner effect.

Many trials have been made to explain superconductivity. Based on Meissner effect, London brothers [4] in 1935 introduced the first phenomenological theory of superconductivity appropriately known as London theory. London Theory accounted for zero resistance and Meissner effect, and predicted a penetration depth (λ) for the magnitude that an external magnetic flux can penetrate into a superconductor. Assuming that inside a massive superconductor the magnetic induction (B) is zero, London brothers developed a hypothesis ($J = -(c/4\pi\lambda^2)A$) about a local relation between the density of superconducting current (J)

and the vector potential of a magnetic field (A). Combining Maxwell equation (curl $B = \frac{4\pi}{c} J$) with the London equation resulted in the finding that, the magnetic field decreases exponentially from the surface toward the interior of a superconductor.

In terms of the density of superconducting electrons (n_s) the penetration depth (λ) is defined by $\lambda^2 = mc^2/4\pi n_s e^2$, where m and e are the mass and charge of the electron, and c is the speed of light. As the temperature increases the concentration of superelectrons decreases and the penetration depth increases according to the relation $\lambda = \lambda_o \{1 - (T/T_c)^4\}^{-1}$.

Another important parameter used to characterize superconductors is the coherence length (ξ) which was first introduced by Rippard [5] in 1953. The coherence length is a measure of the distance within which the superconducting electron concentration is not changing drastically in a spatially-varying magnetic field. The intrinsic coherence length (ξ_o) is taken to be $\xi_o = 2\hbar v_F/\pi E_g$, where h is Plank's constant, E_g is the energy gap and v_F is the electron velocity at the Fermi surface.

Later in 1950 Ginzburg and Landau [6] introduced their famous theory of superconductivity, which described superconductivity in terms of a macroscopic wave function (order parameter) and provided a derivation of the London equations. The theory was based on the assumption that, some part of conduction electrons in a superconducting state of metal

forms a peculiar superfluid liquid (condensate), distributed with local density $\rho_s(r)$ over the whole volume of a crystal. The superfluid is capable of moving as a whole with local velocity $v_s(r)$. As the temperature rises, part of the electrons "evaporates" from the condensate and forms a "weakly excited gas" - a normal fluid - which is also distributed over the whole volume of a crystal with local density $\rho_n(r)$ and capable of moving with local velocity $v_n(r)$. In this case $\rho_n(r) = n(r) - \rho_s(r)$.

Ginzburg and Landau made an important step towards constructing quantum theory of superconductivity. They made the postulate, that the density of superconducting electrons $\rho_s(r)$ is proportional to the squared modulus of some wave function (order parameter) $\psi_s(r)$ of a superconducting state, which is dependent only on one coordinate. At the equilibrium state, when $T > T_c$, this function is equal to zero, and when $T < T_c$, it is different from zero.

One of the most remarkable achievements of the Ginzburg-Landau (G-L) theory was the introduction of the important dimensionless parameter $\kappa = \lambda/\xi_0$ whose value determines the type of the superconductor

In 1957, Abrikosov [7] showed that the G-L theory implied that, two groups of superconductors are possible. Superconductors with $\kappa < 1/\sqrt{2}$ were referred to as superconductors of the first kind. In these superconductors, when the applied external magnetic field (H) is less than the critical field (H_c) the mean magnetic field inside the sample (B) is

equal to zero. As the external magnetic field increases there is an abrupt (within the limits of one or two gauss) destruction of superconductivity.

The second group of superconductors are those in which the field partially penetrates into a massive superconductor within some range of magnetic fields. This group of superconductors with $\kappa > 1/\sqrt{2}$, which are called superconductors of the second kind. In such superconductors a magnetic field does not penetrate into a massive specimen (upto field $H = H_{c1}$). As the external field increases from H_{c1} to H_{c2}, the field partially penetrates the specimen so that the field induction increases and, at H_{c2}, it approaches a value characteristic for normal metal. The resistance of the specimen (up to H_{c2}) , remains zero.

In the 1950's experiments were going on to examine the effect of changing the isotopic mass of a superconductor on its transition temperature. In these experiments [8] the transition temperature was found to rise as the inverse square root of the isotopic mass of the element. This effect provided support for the electron-phonon interaction to be responsible for superconductivity.

The conceptual and practical understanding of superconductivity were not yet clear until Bardeen, Cooper and Schrieffer in 1957 [9] proposed their theory (referred to as the BCS theory). According to the BCS theory, all the electrons condense into a single state and they flow as a totally frictionless fluid, the interaction between electrons and phonons lead to pairing of electrons (Cooper pairs). At low temperatures Cooper

pairs condense into a superconducting state with an energy gap between this state and the normal electron states. The Landau-Ginzburg and London results fit well into the BCS formalism.

Associated with the systematic search for theoretical understanding of superconductivity, many new materials were discovered with superconductivity at temperatures as high as 20 K. While studying the properties of one of these materials Kunzler and co-workers found that, (Nb_3Sn) sustained superconductivity to very high current densities and very high magnetic field. This discovery confirmed Abrikosov prediction in 1957 that there are two types of superconductors. The practical field of superconducting magnets and all large-scale applications of superconductivity grew out of this discovery.

The theoretical basis for electronic applications appeared in the early 1960's. While Josephson [10] was examining the superconducting tunneling using BCS theory, he found that not only single electrons could tunnel, but also Cooper-pairs could tunnel as well. He also found that a voltage across the barrier would create a high-frequency alternating super current.

In the years between 1960 and 1986, the electron-phonon mechanism of superconductivity has been confirmed and superconductivity was discovered at low temperatures in many materials. The highest transition temperature was found in 1973 by Gavaler [11] in Nb_3Ge at 23 K which still requires liquid helium or liquid hydrogen cooling.

In January 1986 Alex Mueller and George Bednorz found indications for superconductivity at approximately 30 K in barium lanthanum copper oxide. These findings were reported to a German journal in April 1986, the paper was published in September [12]. This publication activated researchers around the world. Bednorz and Mueller's findings were confirmed and the highest achieved transition temperature began a rapid rise. By the beginning of 1987 the La-Sr-Cu-O system was fabricated and its transition temperature was found to be close to 40 K at atmospheric pressure [13] and around 52 K under higher pressure [14]. Soon thereafter, Chu and co-workers in 1987 [15] announced superconductivity at 90-95 K in the yttrium-barium system. One year later, the bismuth and thallium systems raised transition temperature to the 110-120 K level [16]. From time to time there are still unconfirmed reports of higher onsets of superconductivity. Fig. 1.1 illustrates the time development in the field of superconductivity.

1.2 High-Temperature (T_c) Superconductors

Recently various superconductors of metal oxides were prepared. Most of these superconductors were prepared by the solid state reaction method, coprecipitation solid-diffusion method or the sol-gel technique.

A number of different, but related systems, have been prepared. To date, at least six major groups of high T_c superconductors can be

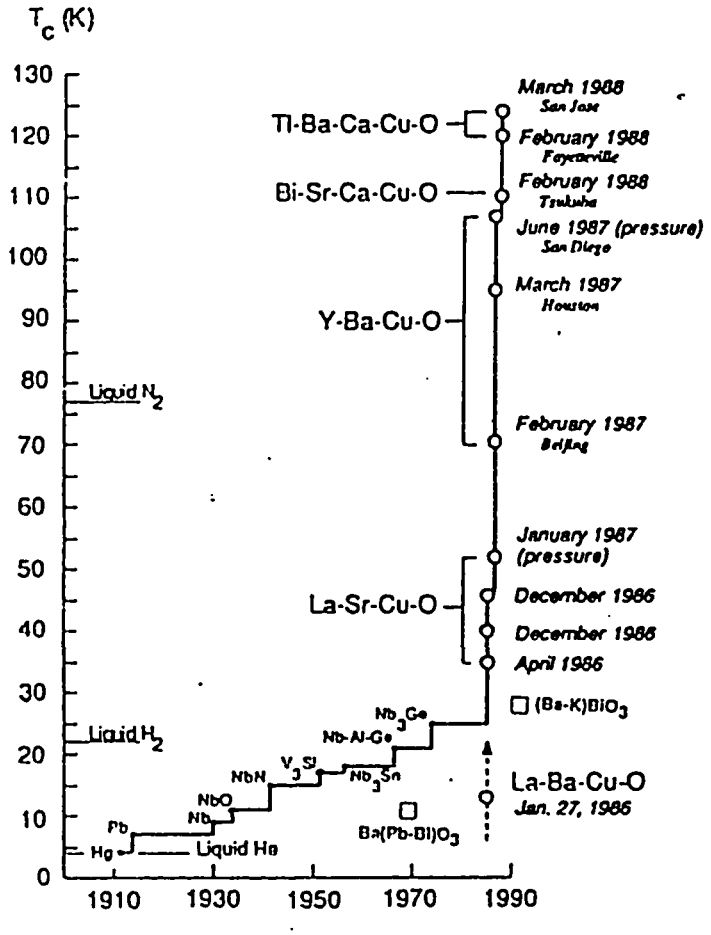

Fig. 1.1 Time development of the field of superconductivity.

normally distinguished:

1) The $La_{2-x}Ac_xCuO_4$ (214) system based on the first high-temperature superconductor discovered by Bednorz and Mueller, where Ac is alkaline earth atom (Ba, Sr, or Ca) with maximum T_c of 40 K.

2) The $YBa_2Cu_3O_{7-x}$ (123) system, where Y can be replaced by other rare earth metals with a maximum T_c of 93 K.

3) The $Bi_2Sr_2CuO_6(CaCuO_2)_n$ systems, with n = 0, 1, 2 and maximum T_c of 105 K.

4) The $Tl_2Ba_2CuO_6(CaCuO_2)_n$ systems, with n = 0, 1, 2 and maximum T_c of 125 K.

5) The (Ba, K) BiO_3 system with a maximum $T_c \sim 30k$.

6) The $(Nd, Ce)_2 CuO_4$ system having a maximum $T_c \sim 30k$.

Table 1.1 summarizes all the observed families with their transition temperatures.

The crystal structure of ceramic superconductors has received a lot of interest, and several models for superconductivity in these materials assume that the lattice structures play an important role in the underlying mechanisms of superconductivity. One of the most striking characteristics of all presently known ceramic superconductors, with the exception of

Material	$T_c(K)$
$La_{1.8}Sr_{0.2}CuO_4$	40
$YBa_2Cu_3O_{6.9}$	95
$Bi_2Sr_2CuO_6(CaCu_2)_n$	10,85,105; n=0,1,2
$Tl_2Ba_2CuO_6(CaCu_2)_n$	85,110,,125; n=0,1,2
$(Ba,K)BiO_3$	30
$Nd_{1.8}Ce_{0.2}CuO_4$	30

Table 1.1 Different families of high-T_c superconductors.

$BaBiO_3$, is the presence of Cu-O sheets (and occasionally chains) that are believed to be the key elements necessary for the occurrence of superconductivity above 30 K.

In fact, all ceramic superconductors, that display superconductivity well above 30 K, contain CuO_2 planes. The crystal structure of La_2CuO_4 system (the parent compound of the first family of high-temperature superconductors) exhibits Cu-O sheets separated by La layers. [17]. However, in the unit cell there is one copper sheet. The crystal structure shows also that, there is a single Cu site and two inequivalent O sites.

The crystal structure of the Y123 system is more complex. Again, the Cu-O planes are separated from each other by Ba-O and Y planes, that are believed to act as insulating planes. [18]. From the crystal structure of the orthorhombic phase it is evident that the superconducting Y123 compound possesses two adjacent Cu-O sheets per unit cell, four inequivalent oxygen sites, and two different copper sites. Also, it has Cu-O chains which is thought to play an important role in some superconductivity models.

The crystal structures of the Bi-Sr-Ca-Cu-O and Tl-Ba-Ca-Cu-O systems are closely related. In both systems, the Cu-O layers are separated from each other by insulating layers of either Ca, Sr-O, or Ba-O. [19,20]. An interesting correlation between the number of Cu-O layers and the transition temperature for superconductivity occurs in these systems. The

transition temperature increases as the number of Cu-O layers increases [21].

For the $BaPb_{1-x}Bi_xO_3$, one of the copper free superconductors; in contrast to copper-based superconductors, superconductivity occurs within the framework of the three dimensionally connected bismuth-oxygen array (not in a 2-d array as in the Cu-O based compounds).

The superconductor based on the $(Nd,Ce)_2CuO_4$ system possesses an interesting property, the charge carriers in this superconductor are electrons rather than holes, which are the charge carriers in all the other high-temperature superconductors discovered to date [22]. Of interesting is also its crystal structure. It was found to be similar to that of $(La, Sr)_2CuO_4$ [23]. Furthermore, it has similar superconductive properties, specially the transition temperatures. Hence the crystal structure of these materials seems to play an important role in their superconductivity, regardless of the polarity of the charge carriers.

The questions of how the electronic and structural properties are related to the mechanisms of superconductivity seems to be relevant. Large number of investigators suggest that, superconductivity in these materials is intimately related to their complex crystallographic structures. Apparently, the onset of superconductivity seems to be sensitive to the valence charge in the insulating layers as seen in $(La, Sr)_2CuO_4$ and $(Nd, Ce)_2CuO$ systems, which need partial replacement of La with Sr and Nd with Ce for superconductivity to occur. The same

thing is for the oxygen contents and the oxygen vacancies in the Y123 system. Further evidence for the relationship between the crystal structures and superconductivity is provided by the correlation between the transition temperature and the number of Cu-O layers in Bi-Sr-Ca-Cu-O and Tl-Ba-Ca-Cu-O systems.

Another important question seems to be concentrated on the most critical element to superconductivity. Since all high-temperature superconductors contain oxygen and all except one contain copper, it is conceivable, that the key element is either oxygen or copper, or perhaps both. Photoemission spectroscopy can play an important role in answering the question of the key element for superconductivity.

1.3 Objectives Of The Thesis

Numerous photoemission studies of the high $-T_c$ superconductors been reported since the first discoveries in 1986 [24,25]. Many X-ray photoelectron spectroscopy (XPS), and ultraviolet photoelectron spectroscopy (UPS) investigations have been performed on the compounds of the Y123 high $-T_c$ superconductor. In these investigations the ground state electronic configuration, the valency of copper ions, the strength of electron-electron correlation, and the nature of hole states, which may lead to superconductivity, are determined. Unfortunately, there was a lack of agreement among the various results. It has become apparent, that this is

partly due to poor preparation of surfaces, and partly due to the instability of these materials under ultrahigh vacuum conditions. In addition, photoelectron spectroscopy (PES) can improve our understanding of superconductivity, in particular, surface superconductivity and its modification by the deposition of different gases and metallic overlayers as means of making contacts.

In this work the electronic structure of Y123 samples was studied by XPS and UPS. Both core level and valence band emission were studied. The different chemical states in the compound and the correlation effects were invistigated by analyzing multiple core level peaks and satellite peaks in the photoemission spectra. The nature of the valence band features was also studied and compared with the theoretically calculated ones. Moreover, the effect of the interaction of gases such as O_2 and H_2O on the electronic structure of the samples, the role of ultrahigh vacuum in sample degredation, as well as the effects of heat treatment, in situ, were studied. The study was carried out using the VG-Scientific ESCA Lab set-up at the Surface Science Laboratory of the Department of Physics, King Fahd University of Petroleum and Minerals.

The samples were prepared by two different methods. The critical temperature T_c, the composition, and the crystal structure of the prepared samples were ascertained using four probe method, X-ray diffraction (XRD), scanning electron microscopy (SEM) and electron probe micro analysis (EPMA),respectively.

CHAPTER 2

THEORETICAL BACKGROUND

Understanding the origin and nature of the high T_c superconductivity - in the new oxide compounds - constitutes one of the most important and challenging scientific problems that has emerged in recent years. The mechanism responsible for superconductivity was intensively studied [26]. However, there is no confirmed theory that explains all aspects of this phenomenon till now.

In this chapter a brief review of the theoretical attempts aiming to explain the specific features of high T_c superconductors is presented along with a brief review of the BCS theory. Also crystallogragraphic structure and electronic band structure calculations are briefly discussed.

2.1 Bardeen-Cooper-Schrieffer (BCS) Theory

The basis of the quantum theory of superconductivity was put

forth by Bardeen, Cooper and Schrieffer in their BCS theory in 1957 [9]. The BCS theory has gained a universal acceptance, because it has proved to be capable in explaining the observed phenomena in superconductivity.

According to BCS theory, superconductivity depends on the existence of an attractive force acting between electrons, strong enough to overcome their mutual electrostatic repulsion. An attractive force arises from electron-phonon interactions. Fig. 2.1 illustrates a classical model of this theory [27]. One electron pulls ions in its vicinity from their equilibrium sites and, as a result, the region around the electron contains more positive charge than otherwise. The region remains positive for a while after the electron leaves and a second electron is attracted toward it. In quantum mechanical description, the first electron changes the number of phonons in one or more vibrational modes and, in turn, they influence the wave function of a second electron.

The attractive force is maximum when the two electrons have propagation vectors that are equal in magnitude but opposite in direction and also have spins that are in opposite directions. Pairs of electrons, that meet these conditions (called Cooper pairs) are the fundamental building blocks of the BCS theory.

A Cooper pair has zero net momentum, and it may be considered as a single particle with zero spin and charge -2e. Such a particle may occupy the lowest energy state. This can lead to a ground state separated from excited states by an energy gap. The critical field, the thermal

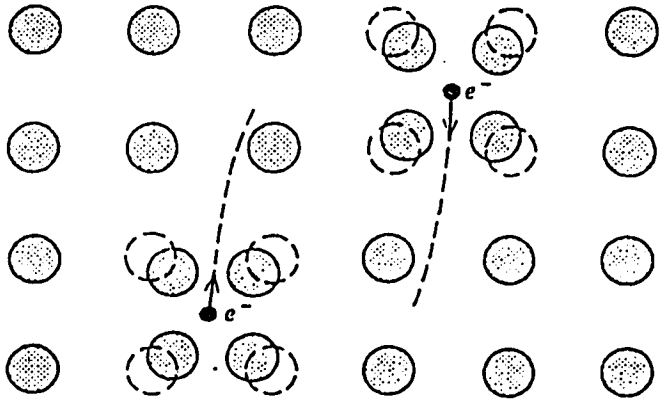

Fig. 2.1 A Classical model of an attractive electron-electron interaction, mediated by the ions of the sample. Each electron pulls surrounding ions from their sites and leaves a wake of positive charge, which attracts another electron. Dotted circles represent the equilibrium positions of ions which have been displaced, [ref. 27].

properties, and most of the electromagnetic properties are all consequences of the energy gap. In special circumstances, superconductivity may occur without an actual energy gap.

The BCS theory makes the following predictions which are comparable with experimental observation for a number of superconductors [28,29]:

a) The energy gap (E_g) is proportional to the transition temperature through the expression

$$E_g \approx 3.53\, k_B T_c$$

(except for the gapless superconductors).

b) The penetration depth and the coherence length emerge as natural consequences of the BCS theory. Also, the London equation is a consequence of the BCS theory, and hence one will expect the state of perfect diamagnetism to exist below T_c with a magnetic susceptibility

$$\chi = -1/4\pi$$

c) The transition temperature is related to the Debye temperature (θ_D), the electron lattice interaction (U) and the density of states { $N(E_F)$ } at the Fermi surface as

$$T_c = 1.134\, \theta_D \exp[-1/\Lambda]$$

where $\Lambda = UN(E_F)$ is called the electron-phonon coupling constant and $\Lambda << 1$.

d) Magnetic flux is quantized with the value $\Phi_o = hc/2e$, where Φ_o is called the flux quantum or fluxoid.

e) For phonon coupling the transition temperature depends on the average isotopic mass (M) through the relation

$$T_c \approx M^{-1/2}$$

2.2 New Models

With the discovery of high T_c oxide superconductors [12,15], the question has been raised whether the pairing theory continues to be applicable, but with an exceptionally strong pairing interaction, or a new totally different framework must be developed. Because of experimental uncertainties as well as incompleteness of the theories, this question has not yet been fully answered. Suggestions on the non applicability of the BCS theory to the present oxide superconductors [30], were countered by others supporting it [31-33]. The evidence that, some variant of the BCS theory is applicable to the present oxide superconductors stems from a number of experimental observations:

1) Josephson tunnelling experiments [34,35] showed electron pairing in Shapiro steps. These steps have the voltage spacing

hν/2e , which is expected for electrons bound in Cooper pairs. Also the flux quantum has been measured [36-38] and it was found to be hc/2e indicating pairing.

2) The temperature dependence of the electromagnetic penetration depth, measured by mean spin resonance, [39,40], has the qualitative features predicted by the BCS theory.

3) Josephson tunnelling has been observed to occur between Pb-Sn alloy and $YBa_2Cu_3O_{7-x}$ [41]. Since a Pb-Sn alloy is singlet-paired. $YBa_2Cu_3O_{7-x}$ is also thought to be singlet-paired, as predicted by the BCS theory, because tunnelling is believed to be impossible between a singlet-paired and triplet-paired superconductor [41].

On the other hand, the new high-temperature superconductors have several unusual experimental features:

1) They are oxygen-deficient perovskites exhibiting low-dimensional characteristics such as well-defined CuO_2 planes and Cu-O chains in Y123 [42,43]. They have very low carrier density $\sim 10^{21}\,cm^{-3}$ and show a strong polarization of the structure.

2) They usually display narrow bands for which electron correlations are important. However, they are close to the metal non-metal transition.

3) The values of T_c exceed the BCS upper limit.

4) They exhibit an isotropic superconductivity with a very short coherence length (ξ) [44-47]. For Y123 single crystal ξ is $\sim$ 16Å in CuO_2 planes and $\sim$ 3Å along the c axis [48].

5) Their superconductivity is extremely type II with the Ginzburg-Landau parameter $\kappa << 1$ (for Y123 $\kappa_{ab} \sim 26$Å and $\kappa_c \sim 240$Å [49] with very large H_{c2} [49-51].

6) Changes in speed of sound at T_c indicate that, states far from Fermi surface are involved in pairing [52,53,56].

7) According to different energy gap measurements [54-56], the pairs are strongly coupled in Y123 $E_g/k_BT_c \approx 8.3$ for Cu(1) and ≈ 2.4 for Cu(2).

8) The magnitude of the observed isotopic effect is very small [57-60] much lower than that predicted by the BCS theory.

9) Spectroscopic and other measurements indicate mixed valence states of Cu and O (Cu^{1+}, Cu^{2+}, Cu^{3+}..., O^{2-} O^{1-}, O^0,...), and very low density of states at the Fermi level [61-64].

10) Changing the oxygen stoichiometry or dopant concentration dramatically affects superconductivity, antiferromagnetism and transport properties.

11) A linear term in the specific heat vs temperature was observed in the La, Y, Bi and Tl compounds at low temperatures [65-68] whereas the BCS theory predicts an exponentially small electronic specific heat if $T << T_c$.

12) Data obtained from Raman scattering experiments indicate that $YBa_2Cu_3O_{7-x}$ may have an energy region which is partially depleted of states, but is not entirely empty [69]. This conclusion was confirmed by infrared absorption measurements [70-72].

To account for the observed experimental features, various mechanisms [73-91] were proposed, based on different models of the electronic structure. Some of these models use the density-functional band calculation to discuss the pairing in a conventional way. Others [73-76, 84-86] employ a Hubbard Hamiltonian for the Cu 3d electrons and emphasize electron-electron correlation effects in a non-conventional mechanism. Other non-conventional mechanisms [90-93] proceed from an extended Hubbard-Hamiltonian model including both the Cu 3d electrons and the oxygen 2p electrons.

In the following sections some of the common proposed mechanisms will be discussed.

2.2.1 Resonating Valence Bonds Model

One of the non-conventional models used for describing high temperature superconductors is the resonating valence bonds (RVB) model proposed by Anderson in 1987 [73]. The model was further developed in many subsequent research papers [74,76,107].

Considering that Cu-O planes play a major role in superconductivity, Anderson used the square lattice at the sites of which a copper ion and two oxygen ions are located, as a model for the undoped La_2CuO_4 ceramic. In the ground state, each site of the square lattice is characterized by an uncompensated spin on the copper ion. These spins seem to form an antiferromagnetic lattice; however, all sites are joined in spinless pairs by valence bonds. Such pairs can not move in an undoped crystal and transfer the electric charge, since free sites are not available. The doped crystal admits excited states with several dimerized state domains divided by walls. The domain wall has no electric charge. but it is characterized by an unpaired spin 1/2 (spinon), Fig. 2.2 a. The effective spinon mass is in the order of magnitude of the electron mass.

Spinons, in Anderson's model, can move due to the resonance of valence bonds. One dimensional example is shown in Fig. 2.2 b. In this figure valence bond (wavyline) of the bound pair situated near the spinon in position 1 can be shifted to the left in position 2. This process will correspond to the neutral spinon transfer to the right.

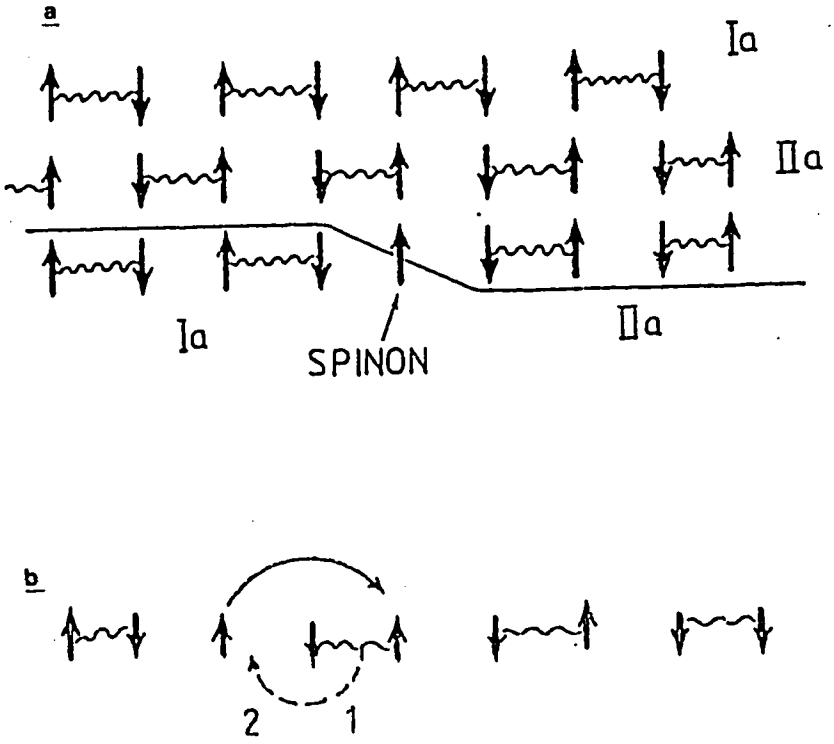

Fig. 2.2 a) Two kinds of the bound pairs (domains) in the one-dimensional lattice; Ia and IIa. The domain wall (spinon) divides th two domains Ia and IIa. b) Illustration of spinon motion (solid arrow). The valence bond (wavy line) is shifted from position 1 to position 2, [Ref. 26].

The Anderson RVB model predicts (or is compatible with several) experimental results, some of which are:

1) The absence of gaps.

2) Insulating and/or antiferromagnetism of undoped or weakly doped Cu-O compounds.

3) The absence of isotopic effect, low temperature specific heat and elastic properties dominated by electronic energies.

4) Anomalous temperature dependence of the normal state resistivity and the carrier density versus Hall-Seebeck coefficients.

5) Effective mass $m^* \approx m_e/\delta \approx 10m_e$, where δ is the doping fraction.

2.2.2 Other Models

In the discussion of the BCS theory, it was mentioned, that superconductor pairs are formed through electron-phonon interaction. Most of the conventional superconductors have weak coupling which means that they satisfy the condition $\Lambda << 1$.

If the new copper oxide superconducts are phonon mediated types, they must have large values of Λ [92-93], because they have a

strongly coupled pairs. The measured value for Y123 was found to be $\Lambda = 2.5$ [94].

Zacher showed [95] in 1987 that, by using highly anisotropic potentials, high transition temperatures can be accommodated in the electron-phonon interaction mechanism. Also, the possible contribution of charge-density wave instabilities to the electron-phonon matrix elements in increasing T_c has been reported [96,97].

Exciton is any type of electronic excitation other than the usual vibrational or phonon ones. The exciton mechanism of high-temperature superconductivity was suggested by Gaididei and Loktev in 1988 [98] when they studied the electronic structure of ceramic superconductors. It was shown, that an extra hole is situated, mainly, on the oxygen site in the unit cell. While moving (in it) the hole interacts with low frequency electron d-d transitions in Cu^{2+} ions. Behaving approximately as Bose particles, they provide, according to Gaididei and Loktev, the pairing between p-holes. Phonon-exciton mechanism was able to explain the E_g/kT_c ratios and the isotopic effect observed in La Sr CuO [99].

An evidence against the presence of excitonic mediated pairing has been deduced from the absence of sharp absorption peaks from the mid-IR through the UV spectral regions [100]. However, some experiments, as suggested in [101], indicate the presence of excitons.

The magnon pairing mechanism of high T_c superconductors was

studied by many researchers [102-105]. It was assumed that, the pairing is realized due to the exchange of spin excitations (magnons). Calculations were made using the Holstein-Primakoff representation for the spin wave operators within the strong coupling approximation. These studies showed that the usual, magnons without the other excitations, do not result in a sufficiently strong attraction.

Plasmon and other bosonic mechanisms were also discussed [106,107]. It was concluded [108-110] that, high T_c arises from combination of 2-D plasmons and strongly coupled phonons. Plasmons were detected by IR-Raman in Y123 [111] and La Sr CuO [112].

The bound state of an electron with a local lattice polarization is called polaron. In attempts to explain high T_c superconductivity, the effect of polarons (bipolarons) was studied [113-117]. Theory of polarons (bipolarons) is based on the electron self-localization in an ionic crystal because of its interaction with the longitudinal optical vibrations of the local polarization created by the electron itself. The electron is kept in the polarization potential well and supports it by its field.

According to biplaron theory, the pairing is realized by virtual optical vibrations that characterize local deformation in the oxygen environment of transition metal in the crystal.

Photoconductivity data indicate that, an ensemble of polarons and excitons play a substantial role in the mechanism of high temperature

superconductivity [119]

The superconducting behavior of the oxides was described in terms of models different from both the phonon BCS and the RVB models. Some of the proposed models involve multiple mechanisms which may include BCS or RVB.

Varma et al [80] have described the behavior of the oxides in terms of charge transfer resonance, where both longitudinal and transverse resonances are included.

Chain and one-dimensional correlation models were postulated. In these models, superconductivity was claimed to be located in the Cu-O planes with T_c raised by the charge-density wave (CDW) instability of the neighbouring Cu-O chains [97]. The discovery of bismuth and thallium superconductor with their lack of chains has caused many researchers to lose interest in the chain model.

Emery suggested that it is important to deal with largest energy in the problem [82]. His model for La_2CuO_4 has an antiferromagnetic insulating limit. The holes reside on O-2p states and not on Cu-3d states because of the short-range repulsion being better screened by oxygen than by copper. Thus the pairing is produced by strong coupling to local spins on the copper sites. This mechanism does not involve Cu^{3+} state [120].

Two spin-polaron models for high T_c superconductivity have been proposed [121]. The first model [122] suggests that, holes introduced by

doping of La_2CuO_4 with Ba or Sr, are located predominantly on the Cu ions so that Cu d^8 configuration plays a crucial role. Accordingly pairing occurs when the holes are on the first-nearest-neighbour Cu sites. In the other model [123] doping with Sr introduces valence-band holes which are assumed to be moved on the O sub-lattice and to avoid the Cu sites. Thus, Cu d^9 is required in this model.

2.3 Crystallographic Structure

Our understanding of the mechanism for high T_c superconductivity is closely related to the detailed knowledge of the structure of these materials. Moreover, it is important to explore possible connections between structural and superconducting properties of the material and establish certain general structural principles to guide our search for new compounds with the same or higher T_c's. Many structural studies were carried out aiming to determine the dimensions of the unit cell, the locations of the atoms in this cell, electronic charge distributions, and the possible presence of atomic irregularities.

The structures are refined from X-ray single-crystal, X-ray powder diffraction and neutron powder diffraction. The crystal structure of high $-T_c$ superconductors share certain features. One common feature is the presence of one or more planes of Cu atoms with four strongly bound O atoms.

The $Y Ba_2 Cu_3 O_{7-x}$ compound exists in two forms, which differ from each other according to the overall oxygen content and the ordering of the oxygen vacancies. The orthorohomic phase, which is usually superconducting, can be formed over a range of compositions $0 < x < 0.5$, while the tetragonal phase, which is usually non-superconducting, occurs when $0.5 < x < 1$. The two phases will be described in turn with a discussion of phase transition.

2.3.1 Orthorhombic Structure

The structure of $Y Ba_2 Cu_3 O_{7-x}$ with $-0.13 < x < 0.61$ was extensively studied [124,125]. Electron and X-ray diffraction studies [126-133] identified the structure to be related to a cubic perovskite with one of the cube axes tripled. Refinements of the cell parameters in several studies [126-128, 131,132,134] indicated that the unit cell was orthorohomic with b-axis slightly larger than a-axis. Neutron diffraction data [135-145] showed unambiguously that the oxygen atoms in the basal copper plane of the unit cell were ordered in the orthorohomic structure.

The essential features of the orthorohomic structure are shown in Fig. 2.3, and the atomic coordinates and thermal parameters for each atom are given in Table (2.1) [146]. The orthorohomic structure was assigned to the space group Pmmm (D^1_{2h}, No.47), with one formula unit per unit cell.

The structure is usually described in terms of Cu - O planes and

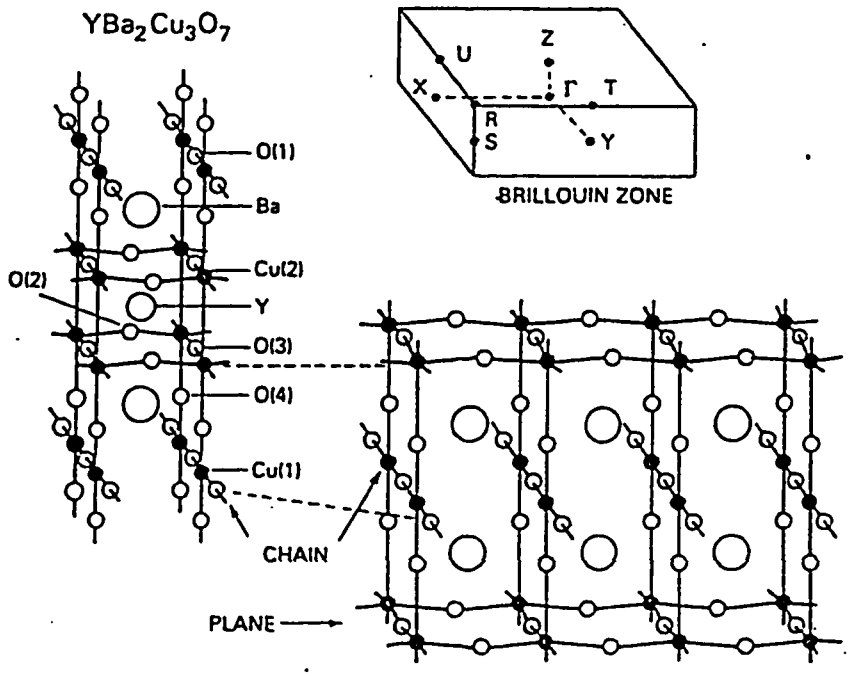

Fig. 2.3 Orthorhombic structure of $YBa_2Cu_3O_7$ with in equivalent sites identified and labelled. Solid bars denote Cu-O coordination and help to illustrate the chain and plane configurations. The inset shows the corresponding Brillouin zone, [Ref. 166].

SPACE GROUP P4/m mm, a = 3.82030 Å, b = 3.88548 Å, c = 11.68349 Å					
Atom	x	y	z	Biso (Å)	OCCUPANCY
Y	0.5	0.5	0.5	0.49	1
Ba	0.5	0.5	0.18393	0.64	1
Cu(1)	0	0	0	0.51	1
Cu(2)	0	0	0.35501	0.52	1
O(1)	0	0.5	0	0.75	0.91
O(2)	0.5	0	0.37819	0.62	1
O(3)	0	0.5	0.37693	0.64	1
O(4)	0	0	0.1584	1.12	1

Table 2.1 Structural parameters for orthorhombic $Y_1Ba_2Cu_3O_{6.91}$ determened from a joint refinment of X-Ray and neutron powder diffraction data taken at 297 K. [Ref.149]

Cu - O chains. The chains consist of Cu1 atom at (0, 0, 0) and O1 atom at (0, 1/2, 0) along the b axis. A neutron diffraction study [145] suggested that the chains may not be perfectly linear. The O4 atom lies above and below the Cu1 atom at $(0, 0, Z_{O4})$ position and the Cu1 - O4 separation (1.834 Å) is the smallest Cu - O distance in the structure. The Cu1 atom is fourfold coordinated with O ions.

The planes consist of Cu2 atoms at $(0, 0, Z_{Cu2})$ neighboured by O2 and O3 atoms at $(1/2, 0, Z_{O2})$ and $(0, 1/2, Z_{O3})$. The Cu - O layers are dimpled, with the oxygen atoms O2 and O3 being nearly coplanar, but with the Cu2 site lying out of this plane by ~ 0.25 Å. The Cu2 displacement out of the O2-O3 plane is toward the O4 site. However, the Cu2 - O4 bond length (2.341 Å) is still greater than that of the Cu1 - O4 bond length. The long Cu2 - O4 distance suggests that the coppers in the planes are weakly linked to those in the chains.

The yttrium ion lies at the center of the cell (1/2, 1/2, 1/2), and is coordinated by eight nearest oxygen atoms that form a slightly distorted square prism. The barium ion at $(1/2, 1/2, Z_{Ba})$, with $Z_{Ba} = 0.1938$ Å, is ten-fold coordinated and is slightly shifted towards the Y ion relative to its position in the ideal perovskite structures.

Selected bond lengths and angles for the orthorohomic structure are given in Table 2.2 [147]. The structure has four oxygen sits O1, O2, O3 and O4, with three of the oxygen sits (O2, O3, O4) are fully and one (O1) is partially occupied. A possible fifth oxygen site O5 in the structure at

Y-O(2)	4*2.418	Cu(1)-O(1)	2*1.947
Y-O(3)	4*2.399	Cu(1)-O(4)	2*1.834
Ba-O(1)	2*2.891	Cu(2)-O(2)	2*1.929
Ba-O(2)	2*2.980	Cu(2)-O(3)	2*1.961
Ba-O(3)	2*2.948	Cu(2)-O(4)	2.341
Ba-O(4)	4*2.750		
O(1)-Cu(1)-O(4)		90	
O(4)-Cu(1)-O(4)		180	
O(1)-Cu(1)-O(1)		180	
O(3)-Cu(2)-O(3)		166.3	
O(2)-Cu(2)-O(2)		165.3	
O(2)-Cu(2)-O(3)		89.1	
O(4)-Cu(2)-O(3)		96.9	
O(4)-Cu(2)-O(2)		97.4	

Table 2.2 Selected Bond Lengths (Å) and Angles (°) in Orthorhombic $YBa_2Cu_3O_7$. [Ref. 147] .

(1/2, 0, 0) is usually empty at room temperature.

2.3.2 Tetragonal Structure

Refined atomic parameters on the non-superconducting samples of $Y Ba_2 Cu_3 O_{7-x}$ with $0.24 < x \leq 1$ were reported by many X-ray single crystal diffraction studies [148,149], as well as from neutron single crystal diffraction and neutron powder diffraction [140,150,151]. The structure assumes a tetragonal symmetry with the space group P4/mmm (D^1_{4h}, No.123).

The ideal symmetry of the tetragonal phase can be described in terms of composition of $Y Ba_2 Cu_3 O_6$ ($x = 1$), whose structure differs from the orthorohomic structure by the removal of the O1 ion from the chain. The resulting structure is shown in Fig. 2.4. It contains one yttrium site, one barium site, two copper sites, Cu1, Cu2, and three oxygen sites, O1, O2, O4. The O 1 oxygen site is partially occupied or empty. The cation arrangement is basically the same as that in the orthorohomic structure. However the oxygen distribution is different. Refined cell parameters, atom coordinates, and selected bond lengths for this structure are given in Tables 2.3 and 2.4. [152].

2.3.3 Phase Transition

Orthorohombic $Y Ba_2 Cu_3 O_{7-x}$ is structurally unstable with respect to oxygen removal, temperature, pressure, and irradiation. As the oxygen is decreased the cell volume increases, the orthorohomic strain

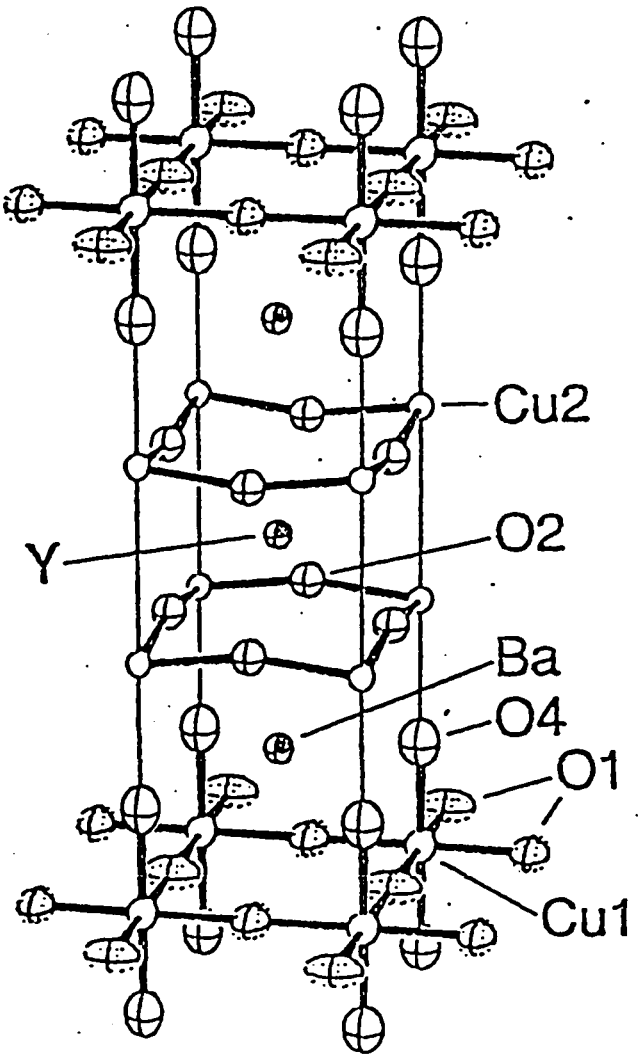

Fig. 2.4 Tetragonal structure of $YBa_2Cu_3O_6$, the oxygen atoms on sites denoted by the dashed ellipsoid are missing, leaving Cu $(O4)_2$ dumbels oriented along the c axis [Ref. 17].

SPACE GROUP P4/m mm, a = b = 3.8570 Å, c = 11.8194 Å					
Atom	x	y	z	Biso(Å)	OCCUPANCY
Y	0.5	0.5	0.5	0.73	1
Ba	0.5	0.5	0.1952	0.5	1
Cu(1)	0	0	0	1	1
Cu(2)	0	0	0.3607	0.49	1
O(1)	0	0.5	0	0.9	0.028
O(2)	0	0.5	0.3791	0.73	1
O(4)	0	0	0.1518	1.25	0.99

Table 2.3 Atom positions and occupancies for Tetragonal $Y_1Ba_2Cu_3O_6$. The O(2) and O(3) positions are pquivalent in the Tetragonal structure. [Ref. 152]

Y-O(2)	8*2.4004
Ba-O(2)	4*2.905
Ba-O(4)	4*2.7751
Cu(1)-O(4)	2*1.795
Cu(2)-O(2)	4*1.9406
Cu(2)-O(4)	2.469

Table 2.4 Selected bond lengths (Å) in Tetragonal $Y_1Ba_2Cu_3O_{6.06}$. [Ref. 152]

decreases and the structure transforms gradually to the tetragonal form.

The orthorohombic-to-tetragonal transition was initially identified by electron beam heating in a transmission electron microscope (TEM) [153], then further studied in-situ by numerous techniques [154-159]. Hot-stage X-ray diffraction [155,156] showed that lattice parameters of Y123 expands linearly up to 500°C. Above 500°C, the oxygen from O1 at (0, 1/2, 0) site is removed causing negative thermal expansion of the b-axis. Part of the removed oxygen goes on the normally vacant O5 at (1/2, 0, 0) site, leading to enhanced expansion along the a-axis. Finally, the a and b axes become equal and Y123 becomes tetragonal. The temperature at which the orthorohombic-to-tetragonal transition occurs is very dependent on the oxygen partial pressure [140,159]. Furthermore, the oxygen stoichiometry at the transition varies with oxygen partial pressure [159].

The orthorohombic-to-tetragonal transition is an order-disorder transformation. The oxygen arrangement changes from fully ordered (at room temperature) to partially ordered (at high temperatures) in the orthorohomic phase, to completely disordered (at higher temperatures) in the tetragonal phase. However, it is not yet clear whether the phase change is a first-order [155,157] or second-order phase transformation [140,158,159].

2.4 Band Structure

The local-density band structure of the Y123 compound has been calculated by several groups with a variety of methods of calculation [160-167]. The results obtained were weakly dependent on the calculation method and the bands were generally the same, except some small details.

For $Y Ba_2 Cu_3 O_6$, there are no oxygen atoms in the x-y plane of the Cu1 atom, which is connected to the Cu2 planes by Cu2-O4-Cu1-O4-Cu2 chains (Fig. 2.4). The energy-band structure for this compound is shown in Fig. 2.5 . Only two Cu d bands lie partly above Fermi level (E_F), so Cu1 is essentially in a $3d^{10}$ state, or Cu1 has formal valency 1+. The coupling of Cu2 planes via O4 2p and Cu1 4s is relatively large (0.6 eV) and the overall band width is 3 eV. This leaves Cu2 in 2+ state with the two semiconductive half-filled Cu2 bands.

The $Y Ba_2 Cu_3 O_7$ has two CuO_2 layers which are weakly coupled to the CuO chain, so a pair of layer-derived CuO_2 pdσ bands is expected to cross E_F similar to the corresponding bands in $Y Ba_2 Cu_3 O_6$. Moreover the Cu1, O1 and two O4 atoms form in the first approximation a one-dimensional system, hence, chain derived bands with roughly one-dimensional dispersion are also expected. The conduction bands in $YBa_2Cu_3O_7$ are ≈ 9 eV wide and arise predominantly from strongly hybridized Cu d - O p states. The 36 bands in this complex are filled by 68 electrons including the valence electrons of Y and Ba. The resulting

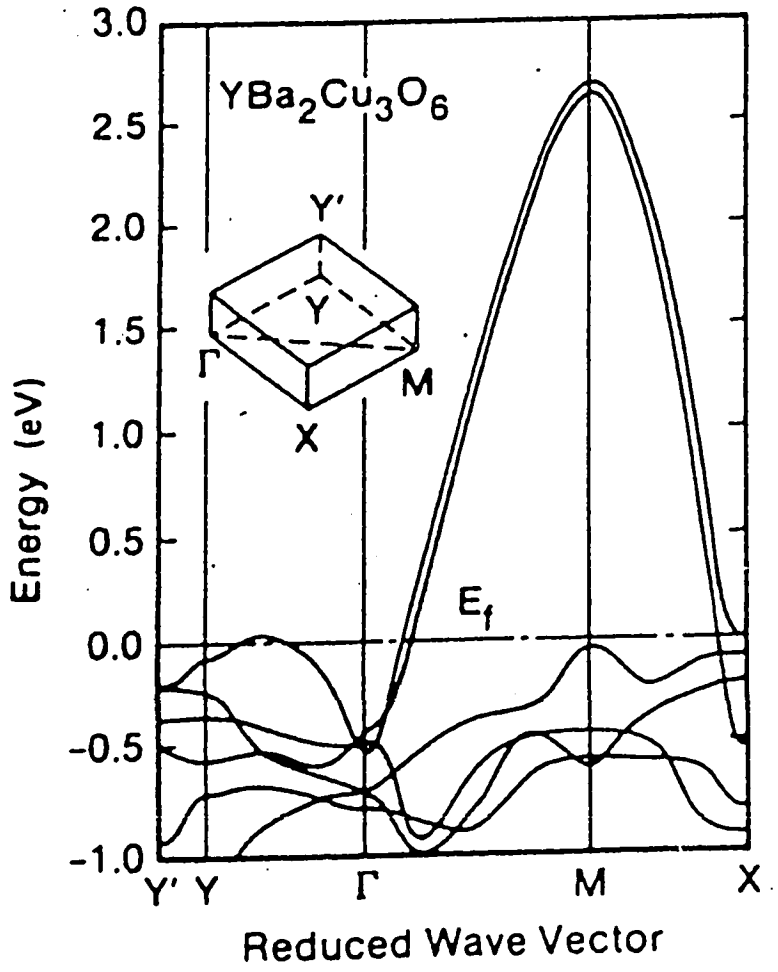

Fig. 2.5 Energy band structure of $YBa_2Cu_3O_6$. Only the six highest Cu 3d - O 2p bands are shown, [Ref. 162].

Y^{3+} and Ba^{2+} states contribute primarily to unoccupied bands separated by a gap from the Cu - O complex. The absence of significant valence charge in the Y layers produces a negligible dispersion along k_z (< 0.1 eV) in the Cu - O bands.

Fig. 2.6 shows bands calculated by using the Linear Augmented Plane-Wave (LAPW) method for $Y Ba_2 Cu_3O_7$. The bands are plotted in the basal plane of the Brillouin zone defined by the high symmetry points $\Gamma(0,0,0)$, $X(\pi/a,0,0)$, $Y(0,\pi/b,0)$ and $S(\pi/a, \pi/b,0)$. There are four bands that intersect the Fermi level. Two of these bands (2) and (3) exhibit dispersion along X-S and Y-S indicative for two-dimensional behavior. The other two (1) and (4) are strongly dispersed along X-S but their relatively flat variation along Y-S suggests a more one-dimensional character.

Bands (2) and (3) are associated primarily with the $Cu-O_2$ planes and are derived from pdσ antibonding combinations of Cu2 $d(x^2 - y^2)$, O2 p_x and O3 p_y orbitals. Bands (1) and (4), on the other hand, originate in the Cu - O chains. Like the plane bands, band (1) represents a pdσ antibonding combination of Cu1 d and neighbouring O pσ states. This band consists of a Cu1 $d(y^2 - z^2)$ orbital, an O1 p_y orbital and O4 p_z orbitals above and below the chain. Band (4) is derived from Cu1 d(zy), O1 p_z and O4 p_y orbitals. It is assumed to result from nearest-neighbour pdπ interactions [168] with contribution from ppσ interactions between O1 and O4 orbitals [166]. The bands that are strongly

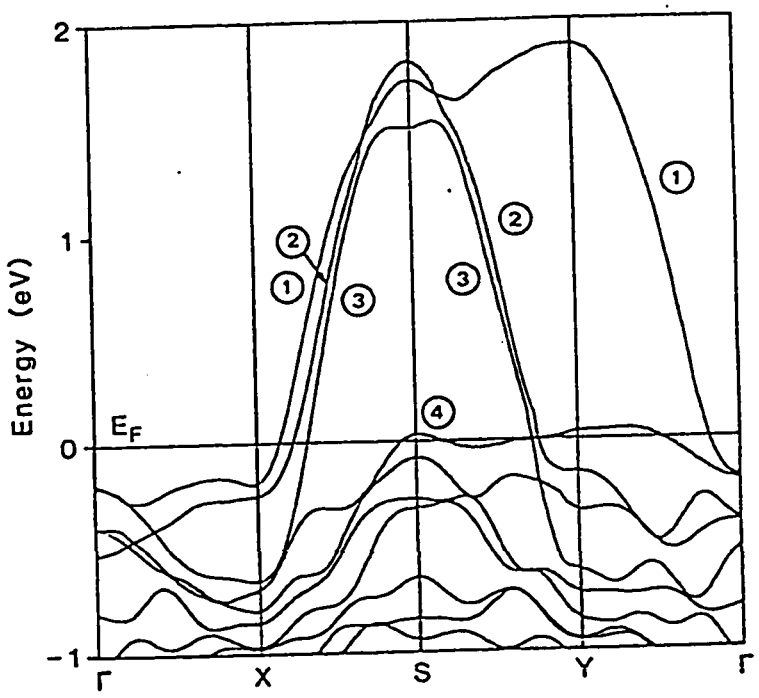

Fig. 2.6 Calcul ated LDA energy band for $YBa_2Cu_3O_7$ at the top of Cu-O complex in central plane of Brillouin zone [After J. Yu, S. Massida, and D.D. Koelling, *Phys. . A*122, 203 (1987)].

associated with the chains, (that is the Cu O1 and O4 atoms) are emphasized in Fig. 2.7 a, while in Fig. 2.7 b the bands associated with the layers (Cu2 , O2 and O3 atoms) are emphasized. As noted in Fig. 2.7 a , the majority of bands within 0.6 eV below E_F is associated with the chain.

The large number of bands crossing the Fermi level in $Y Ba_2 Cu_3 O_{7-x}$ gives rise to a complicated Fermi surface. The states above E_F can accommodate four holes that are distributed unevenly among bands (1) - (4). Bands (2) ((3)) is slightly less (more) than half full while band (1) ((4)) is almost completely empty (full). The flatness of band (4) makes both Fermi surface and the value of $N(E_F)$ difficult to be calculated accurately and strongly dependent on x.

The total and partial densities of states (DOS) of $Y Ba_2 Cu_3 O_7$ are shown in Fig. 2.8 a with an enlargement at E_F in Fig. 2.8 b. The Fermi level falls just above the high-DOS region, and lies 0.1 eV above the very sharp peak of chain derived O1-O4 states. Theoretical $N(E_F)$ values [160-167] for this compound range from 3.4 to 6.6 states/eV-cell. The main contribution to the total DOS comes from the p electrons of oxygen and the d electrons of copper with O p character dominating near the Fermi energy. Among the other notable features from the partial DOS in Fig. 3.8 a,b is the nearly identical densities of states of O2 and O3 indicating the small effect of orthorhombicity on the electronic structure of the Cu - O layer. The DOS of the chain O1 and O4 atoms are also similar to each other but their spectral weight is shifted to higher energies relative

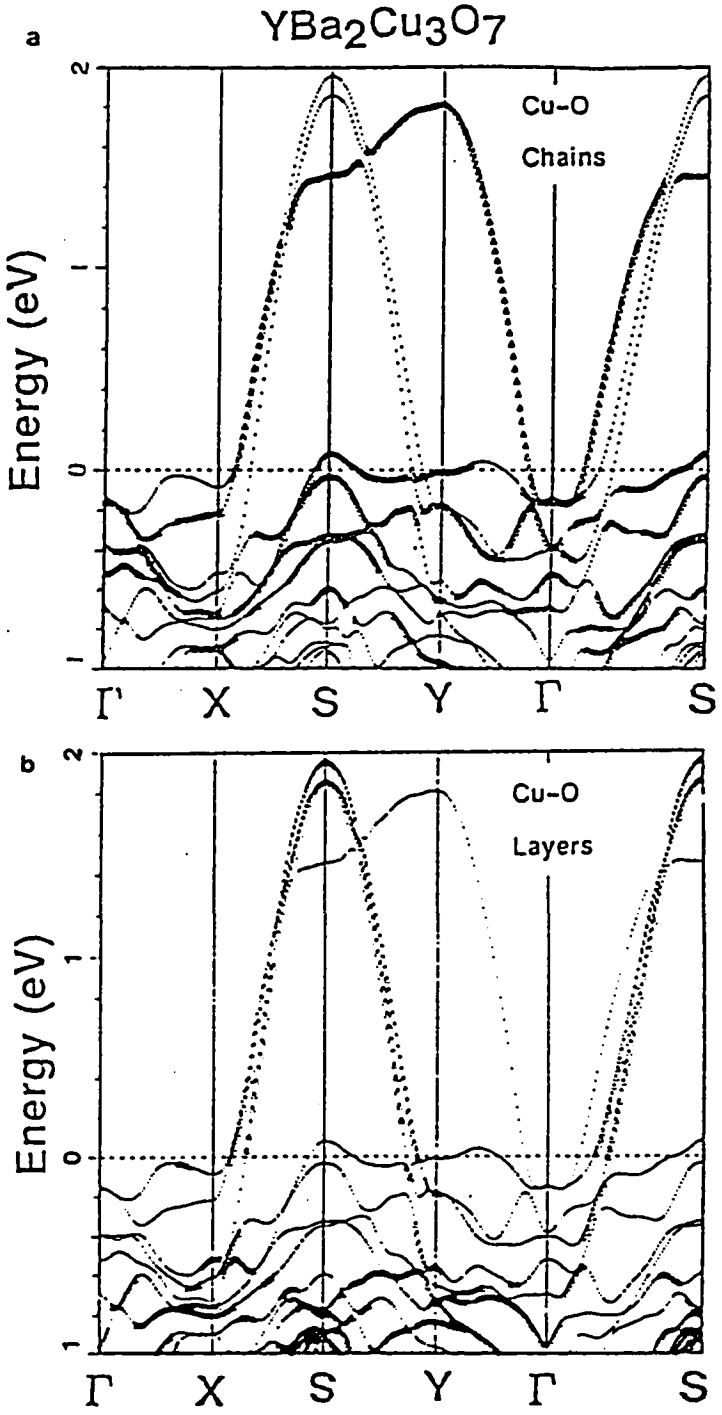

Fig. 2.7 a) Band structure in the $k_z = 0$ plane near the Fermi level $E_F = 0$ with states having more than 60% of their weight on the two Cu(2)-O(2)-O(3) layers. Note that most of the states within 0.5 eV below E_F are chain-related states, [Ref. 166].

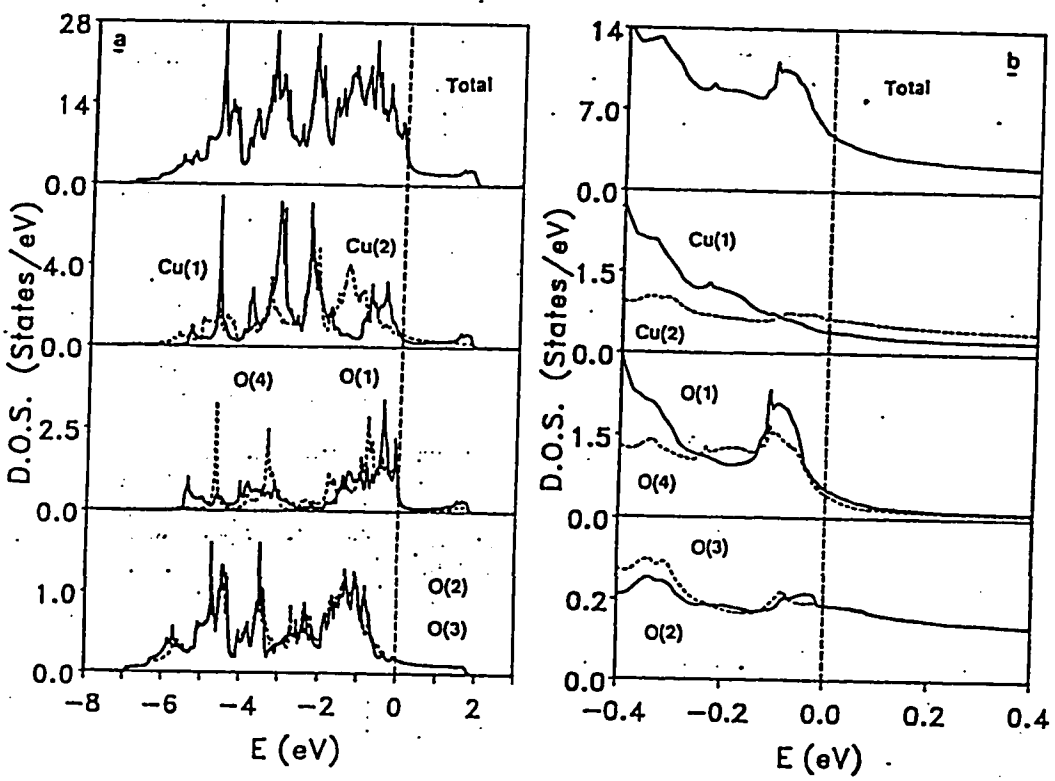

Fig. 2.8 a) Total and partial densities of states (DOS) of $YBa_2Cu_3O_7$. Top panel, total DOS; second panel, O1 (solid) and O4 (dashed DOS; third panel, O1 (solid) and O4 (dashed) DOS; bottom panel, O2 and O3 DOS, which are nearly identical. b) Enlargement of the densities of states of Fig. a near the Fermi level. Note that the striking peak just below E_F involves only chain oxygen (O1 and O4) states. [Ref. 166]

to O2 and O3. The chain Cu1 atom has a considerable weight within 1 eV of E_F, whereas the corresponding weight of Cu2 appears to be shifted downward by 1 eV.

CHAPTER 3

EXPERIMENTAL DETAILS

3.1 Sample Preparation

It is not difficult to synthesize copper oxide superconductors with purity sufficient to exhibit zero resistivity or to demonstrate levitation. Nevertheless, the superconducting properties of copper oxide superconductors are very sensitive to the method of preparation and annealing. To get high-grade single-phase specimens, a particular attention has to be paid to calcination temperature, annealing time, quenching conditions, oxygen content, annealing cycles, grain sizes and palletizing procedure.

Copper oxide superconductors, in general, can be prepared by three methods, namely, the solid state, the coprecipitation and the sol-gel techniques. In the present work, samples were prepared by the first two methods as discussed below.

3.1.1 Solid State Reaction Method

In this method, superconducting samples are prepared by weighing out the required ratio (Y:Ba:Cu = 1:2:3) from ultra pure powders of Yetterium oxide (Y_2O_3), Barium Carbonate ($BaCO_3$) and copper oxide (CuO). The powders are thoroughly mixed and ground using an alumina mortar and pestle for more than one hour. The mixture is placed in alumina crucible in a furnace and calcined in air at 800°C for five hours. After cooling, the calcined mixture is reground and cold pressed into 2-4 mm thick, 10mm diameter pellets at a pressure of 1000 kg/cm^2. The pellets are then annealed in oxygen atmosphere at 1000°C in a tube furnace equipped with temperature controller, for twelve hours. The pellets are allowed to cool down slowly to room temperature inside the furnace with oxygen flow. Subsequently, the sintered pellets are ground, pelletized, and then annealed as before. The latter process is repeated twice more to achieve single phase superconductor samples.

3.1.2 Coprecipitation Solid-Diffusion Method

In this method, powders of ultra-pure Y_2O_3, $BaCO_3$ and CuO in stoichiometric ratio Y:Ba:Cu = 1:2:3 are dissolved in concentrated HNO_3 and mixed by magnetic stirrer. The resulting blue solution is further stirred as it is evaporated to dryness on a hot plate. The residue blue/white solid is placed in alumina crucible and decomposed in a furnace at 800°C for 30 minutes. After cooling, the resulting black powder is

ground thoroughly and pressed into 2-4mm thick, 10mm diameter pellets at pressure of 1000 kg/cm^2. Subsequently, the pellets are annealed in oxygen atmosphere at 1000°C, following the same steps in the solid state reaction method.

3.2 Transition Temperature Determination

Two classic ways of defining superconductivity can be applied to check the quality of the prepared samples, one is the disappearance of the electrical resistivity and the other is the flux expulsion or the Meissner effect. Flux expulsion shows up as a large negative susceptibility in the susceptibility measurement. In general, the magnetism measurements provide a good experimental indicator of the overall superconductor state, while the resistivity measurement is a good practical guide for application purposes. A sharp high T_c transition is an indicator of a high quality sample.

3.2.1 Resistivity Measurements

The resistance measurements were carried out on the pellets as prepared. The critical temperature was mainly determined by the standard four-probe technique using pressed indium contacts. The sample temperature was monitored by a calibrated copper-constantan thermocouple imbedded in the copper block underneath the sample. A small current (10mA) was supplied to the samples from a Keithley

constant current source and the potential difference was measured by means of a Keithley nanovoltmeter.

The resistance was measured over a temperature range of 50-250 K, starting with the sample slightly over the liquid helium and then slowly brought to higher temperatures. The temperature was changed by changing the height of the sample holder over liquid helium level. At every height, a small period of time was required for the temperature to stabilize. It is required to keep as small as possible the temperature difference between both the ends of the sample and the temperature difference between the sample and the thermometer, and to lower the temperature change rate to avoid hysteresis in the process of temperature rise and fall. When the temperature became stable, the nanovoltmeter reading for both the two directions of current, and the electromotive force (e.m.f.) of the thermocouple was recorded. From these readings the temperature was determined using calibration table of the thermocouple, and the resistance was calculated by ohm's law.

3.2.2 Definitions of Critical Temperature

An important question arises about the operational definition of the transition (critical) temperature T_c. Several different definitions of T_c were adapted by different authors. Some authors describe T_c in terms of the onset, 5%, 10%, 90% and 95% points, others defined T_c in terms of midpoint and zero resistance points. Fig. 3.1 shows some of the definitions on experimental resistivity curve. The first point (1) is T_c (zero-resistivity)

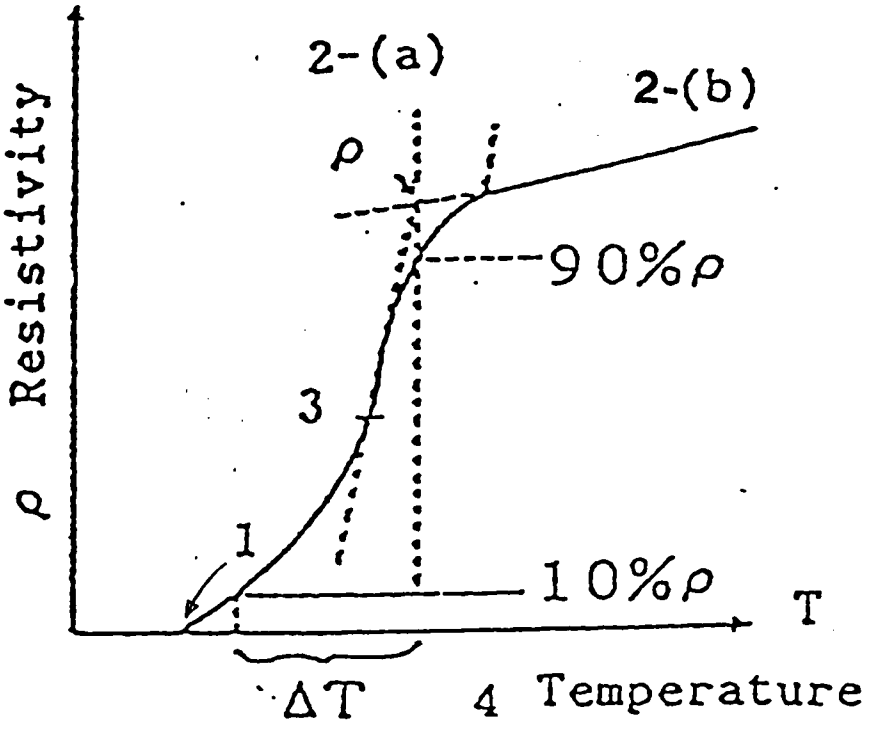

Fig. 3.1 Critical temperature on Resistivity-Temperature curve.

which represents the temperature below it a sample exhibits less than $\pm 1 \mu V$ or precisely 10^{-8} V. The second point is T_c (onset) temperature which can be defined in two ways: (a) temperature at the intersecting point of extrapolating lines between normal state and superconductive-normal transition in resistivity temperature curve, point (2-a), (b) temperature at the deviation point of normal state in resistivity-temperature curve, point (2-b). Another point is T_c (midpoint) defined as temperature at midpoint of the resistivity (ρ) in superconductive-normal transition. Also, the transition temperature is determined from the transition width ΔT which is the temperature space between temperatures at 10% ρ and 90% ρ shown as point (4)in the figure .

3.3 Structural Analysis

In addition to the superconducting properties, it is also of interest to know the structure of the sample. The crystallographic structure can be easily checked by the X-ray powder diffraction (XRD) and powder neutron diffraction methods. From XRD pattern, the phase can be determined and the sample lattice constants a, b, c can be defined. Narrow lines and the absence of spurious signals indicate a good single-phase sample.

Moreover it is important to know the chemical composition of the sample. The nominal composition can be deduced from the relative proportions of the various elements in the starting material. EPMA that is

favorable for low-atomic-weight elements and other chemical analysis techniques can be applied for the compositional analysis. In the next two sections the XRD and EPMA studies are reported.

3.3.1 X-ray Diffraction Study

The crystal structure characterization of the samples was carried out using the X-ray diffraction technique. XRD patterns of the pellet samples was obtained using a computerized PHILIPS diffractometer at the King Fahd University of Petroleum and Minerals Research Institute (KFUPM-RI). Copper Kα radiation of wave length (Average λ = 1.54178 Å) was used with Cu broad focus tube at 45 kv and 30 mA. The angle (2θ) was scanned in the range from 5° to 80° using a scanning speed of 0.01°/sec. The diffraction patterns obtained for the different pellet samples were similar.

3.3.2 Scanning Electron Microscope Study

Sample of Y123 superconductor was examined by both SEM to observe the surface topography and EPMA to identify the elements present. The study was performed with a JEOL JSM-840 scanning electron microscope at Materials Characterization Laboratories (MCL) in the KFUPM-RI.

The analysis was done for as prepared pellets. The samples were stuck onto the SEM specimen holder with carbon paint and the SEM was

operated with an acceleration voltage of 20 kv in the secondary electron image mode.

3.4 Photoelectron Spectroscopy

3.4.1 Introduction

Electrons and photons are the most easily available particles by which matter can be probed. Hence, many spectroscopic techniques involve the use of these two types of particles. In a typical spectroscopic experiment, as shown in Fig. 3.2, an electron or photon of a defined state (energy, direction of propagation, polarization) impinges on a sample. As a result of the impact electrons and/or photons escape from the sample, the state of at least one type of the escaping particles is analyzed with a spectrometer.

Photoelectron spectroscopy (PES) is today known as the common name of a variety of similar experimental techniques that are all based on photon-stimulated emission of electrons from the material. Since the photon energy is known, the energy distribution of the photoemitted electrons bear direct information about the occupied energy levels in the material. Thus, PES's are utilized to determine the electronic structure of materials. A part from the energy, other properties of the ejected electrons may be analyzed, for instance, the distribution of photoelectron intensity with the angle of emission or the orientation of the electron spin.

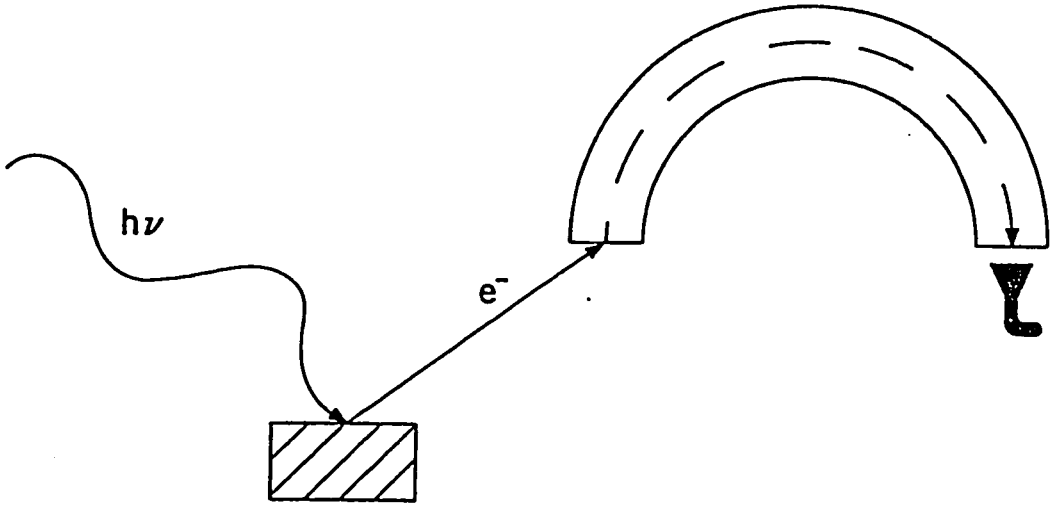

SOURCES	SAMPLES	ELECTRON ANALYZER	DETECT
He I, 21.2 eV } UPS He II, 40.8 eV } UPS	Gases Liquids	Magnetic electrostatic	Energy distribution I(E)
Y M_ζ, 132.3 eV	Solids		Angular distribution A(θ)
Mg Kα, 1253.6 eV } XPS Aℓ Kα, 1486.6 eV } (ESCA)			Electron spin polarization P(σ)
Synchrotron radiation, (10^{-4} eV ≲ hν ≲ 10^4 eV)			

Fig. 3.2 A schematic diagram of photoelectron spectroscopy with the principle features.

PES is an extremely useful spectroscopic tool, because it can be applied to matter in its various states and it is sensitive to all elements. It has by now become a widely-used technique for studying the properties of atoms, molecules, solids, and surfaces. Also, it is established as a powerful technique for the investigation of the electronic structure of materials [169-172].

In essence, the technique involves analysis of electrons ejected from matter by incident radiation. The sample under study is illuminated by nearly mono-energetic photons of well-defined energy. The photons are absorbed in the sample by the process of electron excitation. If the photon energy hv is sufficiently high, electrons within the irradiated sample volume with binding energies less than hv, are ejected. This process is illustrated, in a simplified single-particle picture, in Fig. 3.3 . The kinetic energy (E_{kin}) of the electrons is analyzed and the electron binding energy (E_b^V) as referred to the vacuum level can be determined by the Einstein relation [173]:

$$hv = E_{kin} + E_b^V \tag{3.1}$$

For solid samples, equation 3.1 can be rewritten as [174]:

$$hv = E_{kin} + E_b^F + \Phi_{spec} + V_c \tag{3.2}$$

where Φ_{spec} is the work function of the spectrometer and E_b^F is the binding energy as referred to the Fermi level. V_c is any net electrostatic potential

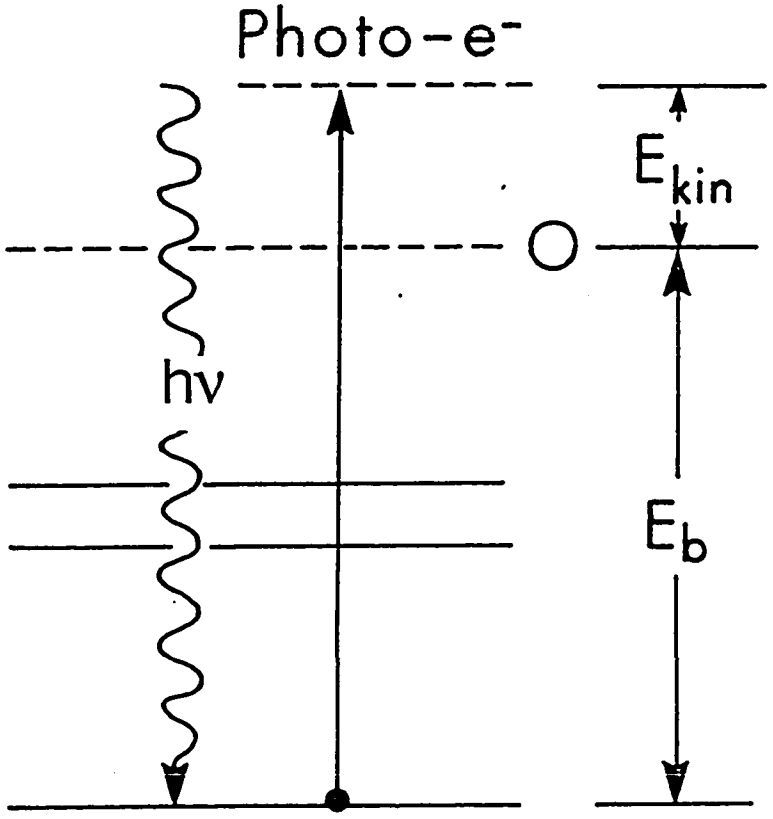

Fig. 3.3 Single-particle picture of photexcitation of electron by photons of energy hν.

on the sample surface with respect to the spectrometer, it may be induced by electron emission and resultant surface charging. Thus, with appropriate photon energies and analyzer settings, any bound electronic state can, in principle, be observed and studied.

Traditionally, PES has been divided into two branches on the basis of the energy of the incident photons used for excitation. The low energy regime (hν = 10-50 eV), is now commonly referred to as Ultraviolet Photoelectron Spectroscopy (UPS), usually employs rare gas resonance lamps as photon sources. A list of the commonly used photon sources is given in Table 3.1. The most common radiations are the He I (hν = 21.2 eV) and He II (hν = 40.8 eV) lines. These lines are sharp (have a small natural width of only a few millivolts), intense, and sufficiently energetic to eject electrons from the lesser bound orbitals (valence electrons) of most molecules. The high energy regime (hν ≥ 1000 eV) is commonly denoted as X-ray Photoelectron Spectroscopy (XPS). The common excitation sources are the characteristic X-ray lines. Table 3.2 lists the energies and widths of a number of characteristic X-rays have been used in XPS. The most common sources are the soft X-ray lines such as MgK_{α} (hν = 1253.6 eV) and AlK_{α} (hν = 1486.6 eV). Radiation in this range provides sufficient energy for the ejection of both valence electrons and core electrons which emerge with a sharply defined values of kinetic energy. However, the resolution is limited because of the line widths which can limit the usefulness of XPS studies. Narrower line widths can be obtained by means of monochromatization.

Source	Energy [eV]	Relative intensity	Linewidth [meV]
He I	21.22	100	3
He II	40.82	20 *	17
	48.38	2 *	
Ne I	16.85	100	
	16.67		
Ne II	26.9	20 *	
	30.5	3 *	
Ar I	11.83	100	
	11.62	80 - 40 *	
Ar II	13.48	16 *	
	13.3	10 *	

* Relative intensities of the lines depend on the conditions of the discharge. Values given are therefore only approximate.

Table 3.1 Commonly used Ultraviolet line sources for photoelectron spectoscopy.

Line	Energy, eV	Width, eV
Y $M\ \zeta$	132.3	0.47
Zr $M\ \zeta$	151.4	0.77
Nb $M\ \zeta$	171.4	1.21
Mo $M\ \zeta$	192.3	1.53
Ti $L\ \alpha$	395.3	3.0
Cr $L\ \alpha$	572.8	3.0
Ni $L\ \alpha$	851.5	2.5
Cu $L\ \alpha$	929.7	3.8
Mg $K\ \alpha$	1253.6	0.7
Al $K\ \alpha$	1486.6	0.85
Si $K\ \alpha$	1739.5	1.0
Y $L\ \alpha$	1922.6	1.5
Zr $L\ \alpha$	2042.4	1.7
Ti $K\ \alpha$	4510.0	2.0
Cr $K\ \alpha$	5417.0	2.1
Cu $K\ \alpha$	8048.0	2.6

Table 3.2 Energies and widths of some characteristic soft X-ray lines.

In the intermediate region between UPS and XPS regimes the continuously-variable synchrotron radiation was used. With proper monochromatization this radiation provides an intense source which is tunable over a wide range of photon energy.

The excitation and emission of a core electron yields an excited ion with a vacancy in an inner shell. This hole can be filled either by a radiative de-excitation, whereby an outer electron drops to fill the hole in the inner orbital giving rise to a characteristic X-ray spectrum, or by an Auger process, in which a second electron is ejected as an outer electron drops in to fill the inner hole. The electrons emitted by the Auger process are observable in the XPS spectrum. The kinetic energy of an Auger electron depends only upon the initial and final state energies and not upon the energy of the exciting radiation, and hence is constant. Auger lines can thus be used as a convenient standard in photoelectron spectrum. Being element specific, those lines may be also used for chemical identification.

A very useful information can be derived from analyzing photoelectron kinetic energy distributions $N(E_{kin})$. This measurement produces an electron spectrum or energy distribution curve (EDC). The physical processes give rise to typical features in the EDC are illustrated in Fig. 3.4 . In the simplest case of the excitation, (diagrams b and d), the entire photon energy hv is absorbed by either a core electron or a valence electron leading to photo ionization process as described by equation (3.1)

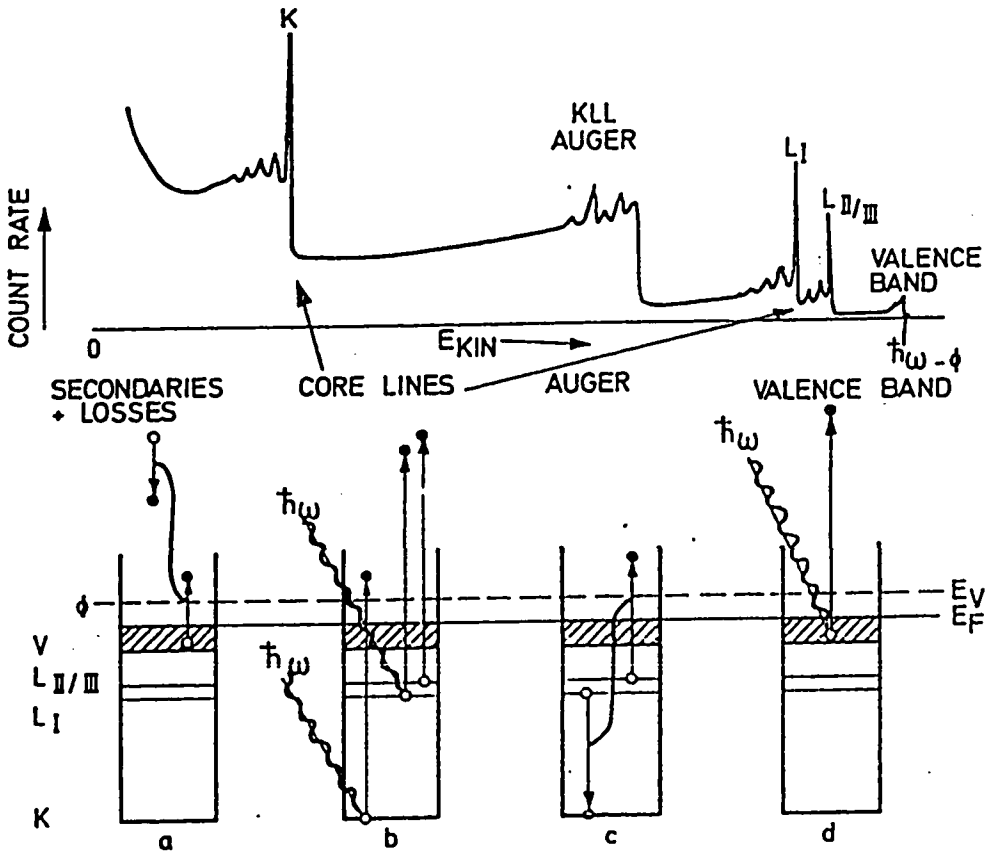

Fig. 3.4 The basic processes contributing to an XPS spectrum (top) include direct optical excitation of core electrons (b) or valence electrons (d), hole deexcitation via the Auger process (c), and inelastic losses (a) giving rise to secondary electrons and plasmon satellites.

or (3.2). Core electrons may excite collective electron oscillations, plasmons, during their excitation or emission, so bulk and surface plasmon loss lines are found in the low kinetic energy side of each sharp structure. This and other such energy loss mechanisms lead to the low energy tails forming the characteristic overall step shape in the spectra. The process of secondary electron emission, where a hot electron loses energy by creating an electron-hole pair in the valence band, is shown in Fig. 3.4a. The secondary electrons give rise to the huge low-energy hump in the spectra. Diagram c in Fig. 3.4 schematically shows Auger process which has been discussed earlier.

3.4.2 Instrumentation

A basic photoemission spectrometer consists of three main parts, the source of monoenergetic photons, the sample, and the electron energy analyzer with its detector. These parts are enclosed in or attached to a vacuum chamber surrounding the sample. The vacuum chamber also houses equipment to prepare and characterize the sample surface.

All of the XPS and UPS experiments reported in this thesis were carried out with a Vacuum Generator (VG) Scientific ESCALAB MKII Spectrometer in the Surface Science Laboratory of the Department of Physics, at King Fahd Univ. of Petroleum and Minerals. A brief description of this system as, well as, a description of the major parts in the system will be given in the following sections.

General Description

The system is a state-of-the-art spectrometer which has the capabilities doing XPS and UPS studies and applying a large number of techniques to carry out the complete surface analysis of a sample under same experimental conditions in one instrument [175]. Fig. 3.5 shows a schematic diagram of the present system and Fig. 3.6 is a photograph of the experimental system. The system consists of five chambers and is specially designed to enable complete control on surface preparation and to quickly transfer samples from a high pressure (upto 30 atmosphere) cell to the analysis chamber ($P \leq 10^{-10}$ mbar) without exposing them to atmosphere, thus avoiding any unwanted surface reactions.

The main analysis spherical vessel is made of mu-metal to reduce earth magnetic field down to 2 milliGauss. This vessel is equipped with dual anode (Aluminum/Magnesium) X-ray source for XPS, X-ray monochrometer with 0.5 meter Rowland circle and twin anode (Aluminum/Silver) X-ray source for high resolution XPS, and ultraviolet radiation from rare gas discharge (He I, He II) for the present UPS study.

An electrostatic energy analyzer also housed in a mu-metal vessel is attached to the analysis chamber. Based on 150mm mean radius spherical sector, the analyzer with two Einsel lenses, adjustable slits, and multi-channel detection (3 independent detectors) provides high efficiency detection of both negative and positive charged particles (electrons and ions) with high angular and energy resolution.

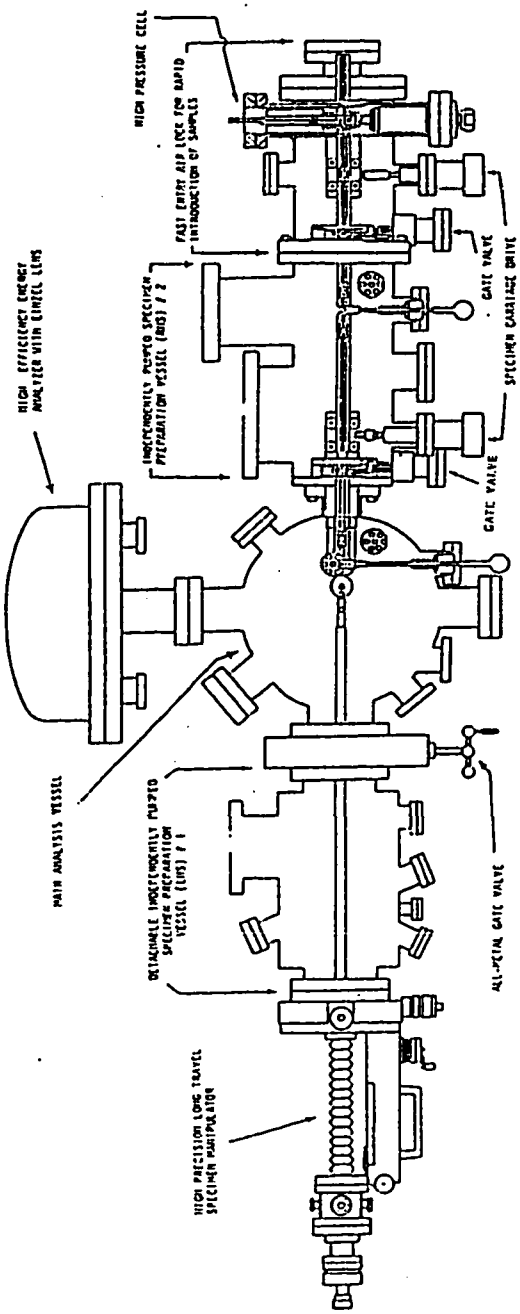

Fig. 3.5 Schematic drawing of the experimental set-up.

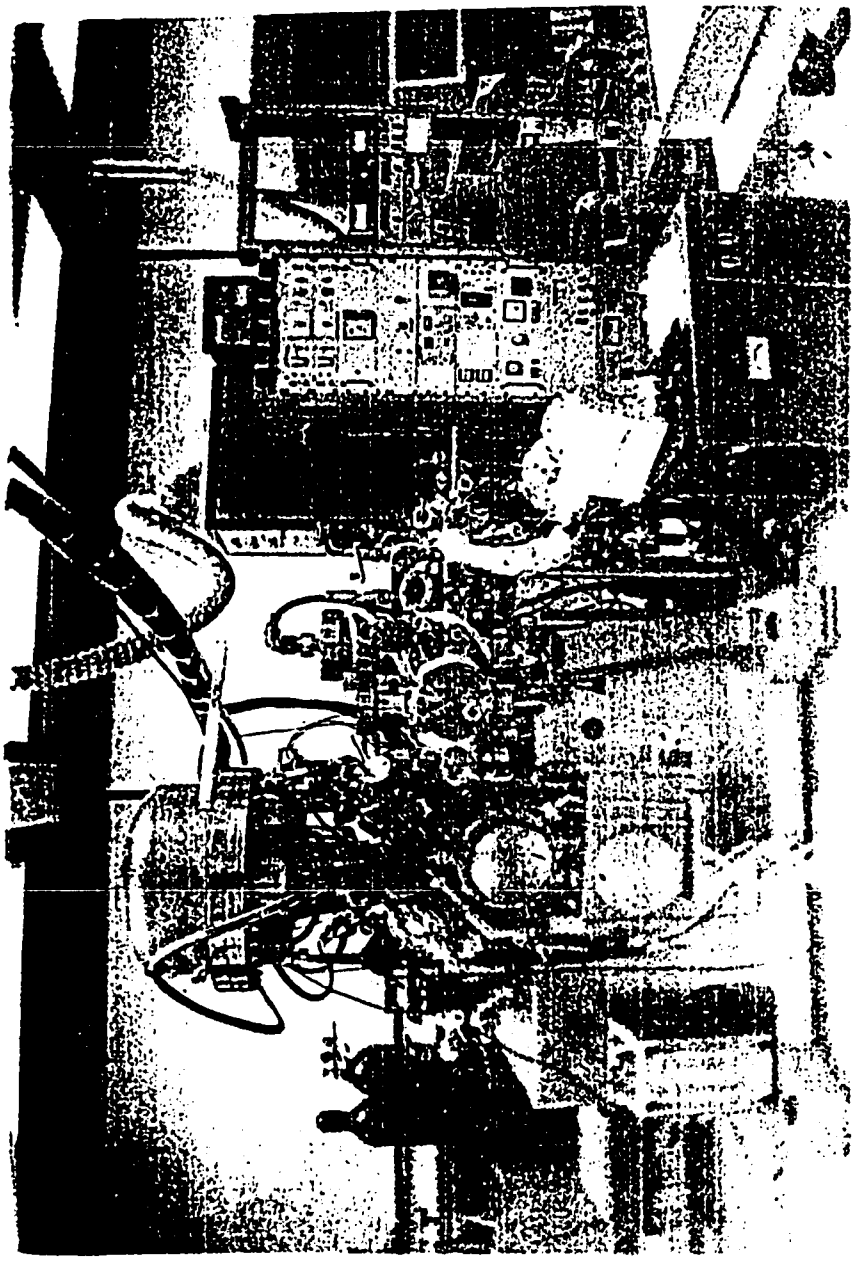

Fig. 3.6 Photograph of the experimental set-up.

The analysis chamber is also equipped with a precision manipulator, a differentially pumped ion gun for sample cleaning and depth profiling using both XPS and AES, and ion scattering spectroscopy (ISS), 10 KeV electron gun with 2000 Å spot for AES and scanning Auger, and electron flood gun for surface charge neutralization of insulator samples.

The left hand side (LHS) preparation chamber is specially designed for preparation of a sample with very well known surface for performing essential basic research. This chamber is mounted on a separate bench and it is attached to LHS of the main chamber via an all metal gate valve. It can be completely separated from the main chamber and can be used as a separate experimental chamber. This chamber is equipped with various special features: a sputtering ion gun, a bakeable gas admission system with three separate gas dosing lines, a quadrupole mass analyzer for gas analysis and thermal desorption spectroscopy (TDS), and a reverse view low energy electron diffraction (LEED) facility. Furthermore, it is equipped with a long travel (600 mm) high precision manipulator with both polar and azimuthal angle rotation of the sample as well as capabilities for keeping a sample at a desired temperature between 100K - 2000K.

The right hand side (RHS) of the system consists of, fast entry air lock, preparation chamber and analysis chamber and can be isolated from each other with built in gate valves. Fast entry air lock attached to the preparation chamber allows rapid introduction of samples without

breaking of vacuum in the system while rack and pinion sample transfer mechanism allows samples of wide range of formats to be transferred from fast entry air lock to the preparation chamber and finally on the precision manipulator in the experimental vessel. There is a facility for parking six samples in the preparation chamber, surface milling and scraping. In addition a high pressure cell has been built in the fast entry air lock unit for sample in-situ treatment.

Vacuum

In photoelectron spectroscopic studies of clean surfaces, the surface must be kept clean over the duration of the experiment, this means that the rate of arrival of reactive species from the surrounding gas phase should be low, also, electrons emitted from the sample surface must have a long mean free path, so that they are not scattered and thereby lost from the analysis. For these reasons photoemission experiments must be performed under ultra-high vacuum (UHV).

In the present experiments, after 100 °C bake out for about 18 hours, a base pressure of 5×10^{-11} mbar in the main chamber is maintained by pumping with a 500 l/s ion pump and titanium sublimation pump (TSP), while a base pressure of 2×10^{-10} mbar is maintained in both RHS and LHS preparation chambers by using a 200 l/s ion pump, a TSP, and a turbomolecular pump. The base pressure of the chambers is measured by BAYARD-ALBERT ionization gauges with VG IGC 26 ION GAUGE controllers.

Excitation Sources

The photon source used for XPS is a soft X-ray source with a dual anode, allowing use of either aluminum K_α (AlK_α, 1486.6 eV) or magnesium K_α (MgK_α, 1253.6 eV) lines by simple external switching. Fig. 3.7 shows a section through the X-ray source. The water-cooled anode has a tapered end with two inclined faces on which films of magnesium and aluminum, respectively, are deposited. There are two filaments one for each face. The source is operated with the filament near earth potential and the anode at a positive potential of up to 15 kV. X-ray photons pass from the vacuum in the source to the vacuum in the analysis chamber through a thin ($1 - 2\ \mu m$) Al window which prevents both stray electrons from the cathode and any possible contamination from entering the analysis chamber.

UPS studies are performed with a helium discharge lamp as a source of UV radiations. Fig. 3.8 shows a diagram of the UV source, in which the discharge is confined by quartz capillary tube and excited by dc power. The source is externally cooled by a fan. The gas is admitted by a bakeable leak valve which gives a fine control to the gas flow rate to the lamp. In order to keep the main chamber base pressure in the range of 10^{-10} mbar during the lamp operation, two stage differential pumping is provided from a roughing pump (1st stage pumping) and the RHS preparation chamber turbomolecular pump (2nd stage pumping). The lamp gas is purified by a liquid nitrogen cooled sorption gas purifier

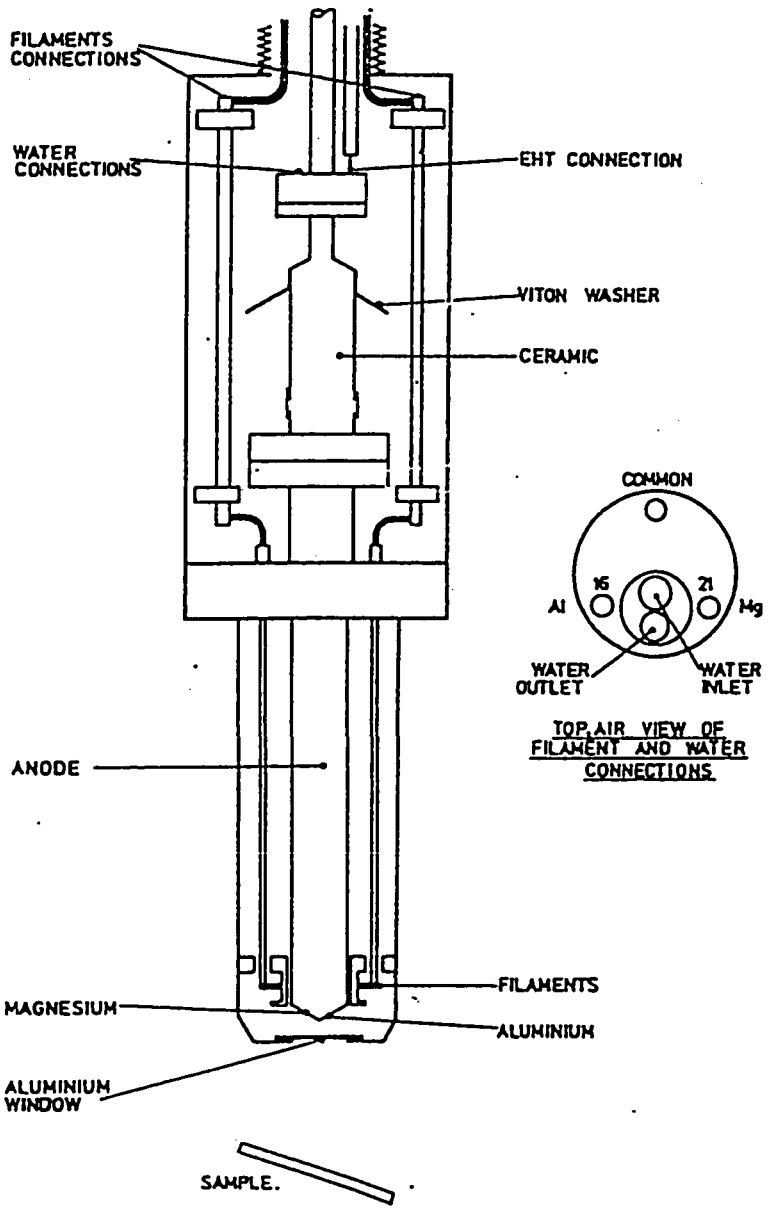

Fig. 3.7 Section through X-ray source.

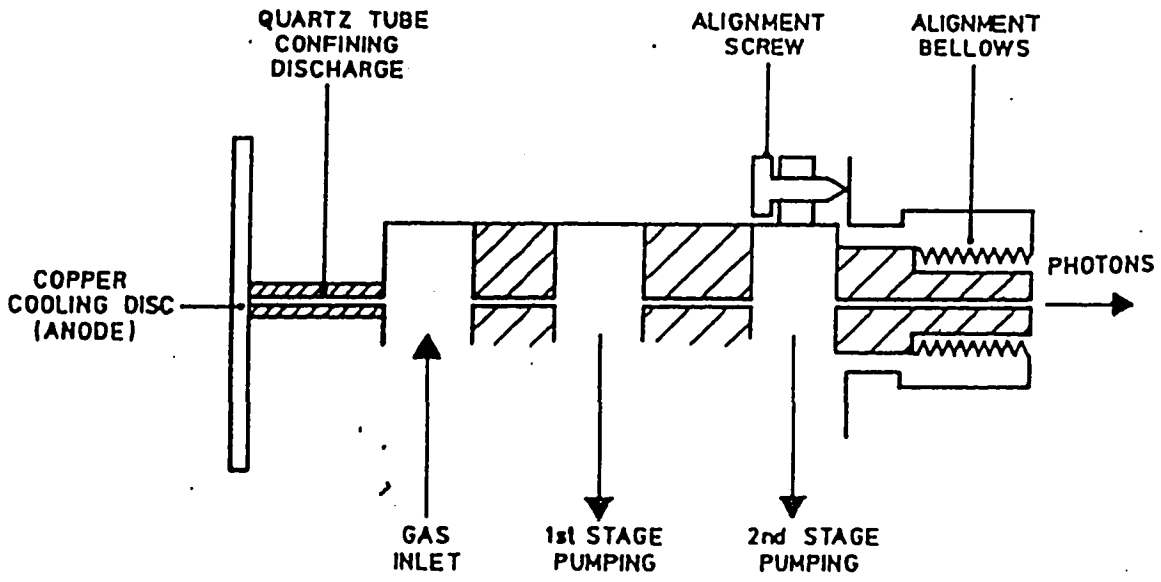

Fig. 3.8 Diagram of UV source discharge lamp.

containing 5A molecular sieve and supplied with a bakeout jacket for regenerating the sieve. The power supply provides 5 kV for starting the discharge and a 1 kV current stabilized supply to run the lamp. The lamp voltage is determined by the discharge characteristics of the lamp itself.

The lamp can operate as a He I source at 21.2 eV with high photon yield and long term stable operation. However, by reducing the gas pressure the relative proportions of the produced He II at 40.8 eV may be increased. In order to optimize the HeII yield, the pressure must be reduced to near the minimum at which the discharge can be maintained. At this optimum the HeII line intensity will be about 30% of the HeI line intensity.

Analyzer Operation and Calibration

The electron energy analyzer is a concentric hemispherical analyzer (CHA). This type of analyzer is always preferred for electron energy analysis, specially for angular dependence measurements and when high-energy resolution is needed [176]. A cross-sectional view of the analyzer with all the major elements from the sample to the detector is shown in Fig. 3.9. The analyzer vessel is made of mu-metal to reduce the magnetic field of the earth. The analyzer acts as a narrow pass filter letting through only electrons with an energy H x D eV, where D is the potential difference between inner and outer hemispheres and H is a

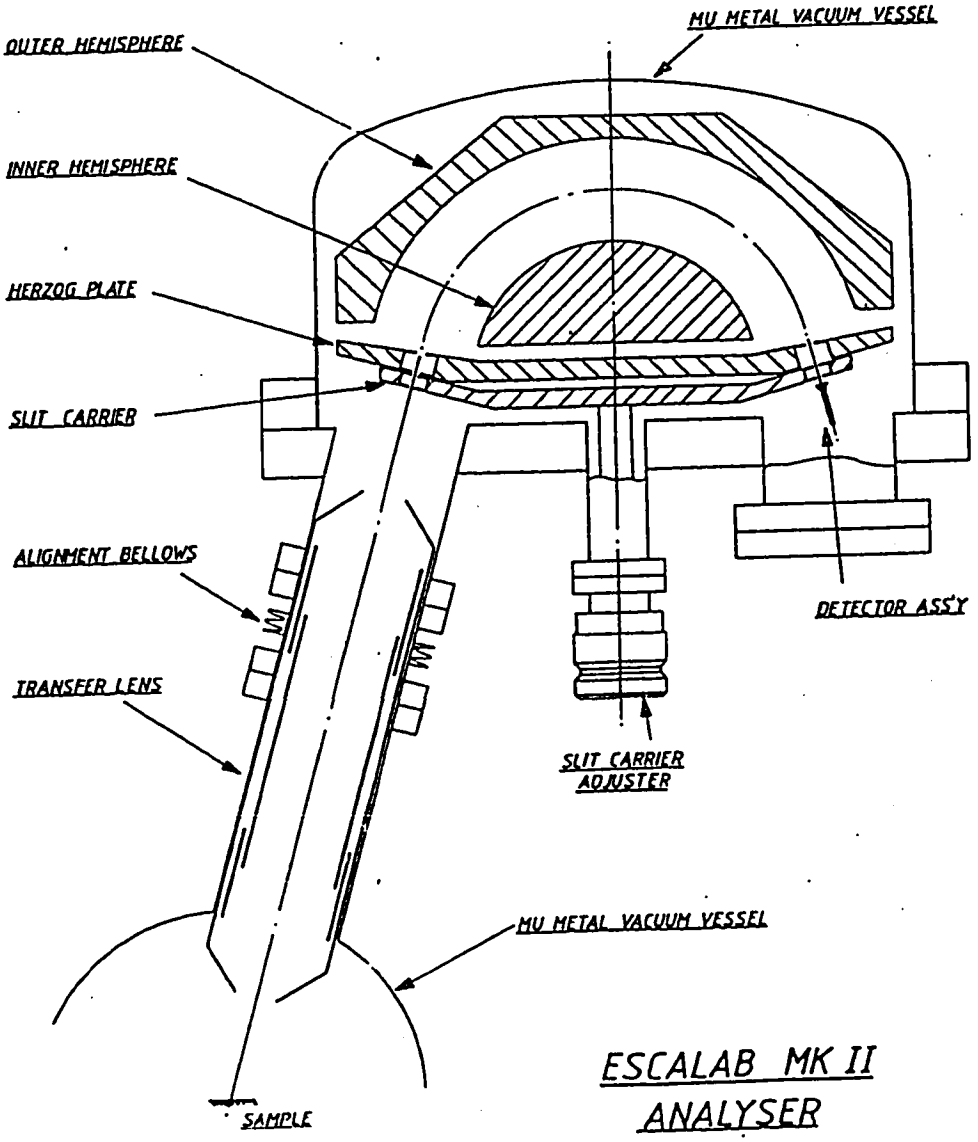

Fig. 3.9 Across-sectional view of the analyser.

constant determined by the geometry of the analyzer. The analyzer operates with the specimen at ground potential and the whole analyzer floats isolated from the ground. Electrons are transmitted from the sample to the analyzer by two Einsel electrostatic lines and retarded in energy by an amount R eV, just before entering the analyzer. If E_{kin} is the kinetic energy with which an electron leaves the sample with respect to the vacuum level, then we have

$$E_{kin} = HD + R + \Phi \tag{3.3}$$

where Φ eV is the work function of the spectrometer.

The analyzer can be operated in either of two retarding modes. In the first mode, electrons are deaccelerated to a constant pass energy, this means that the absolute resolution (ΔE) will be constant over the entire spectrum. This mode is termed constant analyzer energy (CAE) or constant analyzer transmission (CAT). The second is the constant retard ratio or constant relative resolution, (CRR) mode, where electrons are decelerated by a constant factor from their total kinetic energies. The analyzer resolution in terms of the full width at half-maximum, ΔE, can be written as [177]:

$$\frac{\Delta E}{E} = \frac{0.63\ w}{R_o} \tag{3.4}$$

where, R_o is the mean radius of the hemispheres and w is the slit width. For a given geometry $\Delta E/E$ (the relative resolution) is constant and it will

only depend on the pass energy, E. During experiments, the analyzer was operated in the CAE mode with pass energy of 10 eV for high resolution XPS study (at this energy, full width half maximum (FWHM) of Ag 3d = 1.1 eV), whereas a pass energy of 50 eV was used for routine survey scans. For UPS study the pass energy used was 5 eV.

The analyzer energy scale was calibrated by using the: Cu $2P_{3/2}$ = 932.67 eV, Cu $3P_{3/2}$ = 74.90 eV, and Au $4f_{7/2}$ = 83.99 eV, photoelectron lines [178]. All the analyzer operating functions are controlled by the PDP 11/73 computer.

High Pressure Gas Cell

The cell is built into a special fast-entry air lock chamber attached to RHS preparation chamber, and comprises a stainless steel tube which passes through the chamber and is welded to it. The sample support assembly contains gas inlet and outlet lines, the sample heater, and a thermocouple, and is fitted to the bottom of the tube. The moveable pressure cell is mounted on a bellows sealed screwed drive, which is fitted to the top of the tube.

When the pressure cell is lowered, it seals to the sample support assembly with silver coated copper gasket. When it is raised, independently stub mounted samples can be inserted into and removed from the cell through an opening in the stainless steel tube by means of a "wobble stick". The cell is equipped with a high pressure gas handling

system includes four stainless steel valves for the inlet, outlet, roughing pump and high pressure gauge, lines.

With the high pressure gas cell, specimen can be exposed upto 30 atmosphere of gas and the exhaust routed to a gas chromatograph, if necessary. Specimen can also be heated to 600°C whilst exposed to high pressure gas. After treatment sample can be transferred quickly to the analysis chamber via RHS preparation chamber without exposing to air to avoid unwanted surface reactions.

System Control and Data Processing

The system is controlled by a fast dedicated PDP 11/73 micro-computer. This computer performs a complete system control and data acquisition and processing with an RSX11-M multiuser operating system. High speed HP plotter and Epson printer and plotter are also connected to the computer. Data processing software includes smoothing, deconvolution, peak fittings, both background and sattelite subtraction and many other facilities.

3.5 Sample Treatment

Before discussing the photoemission results obtained on the Y123 high-T_c superconductor, we will discuss the stability of these materials in UHV and how the sample surfaces are prepared prior to the photoemission measurements. It is now well established that the mean free path of an

electron is a sensitive function of its kinetic energy inside a solid. In most materials, the mean free path follows a curve known as the "Universal Curve" that exhibits a "U-shape", as is illustrated in Fig. 3.10, [179]. From this curve it is evident that PES in both XPS and UPS regimes is extremely surface sensitive. This makes the preparation and preservation of a clean sample surface a main experimental task. Moreover, surface contamination can occasionally, almost totally, obscure the electronic structure of the bulk material.

3.5.1 Surface Cleaning

Special attention has to be paid to the surface cleaning procedure in photoemission experiments, particularly for high-T_c superconductors, since they contain a fairly loosely bound oxygen atoms. These oxygen atoms can easily evaporate from the sample surface, especially under UHV conditions. Because of these loosely bound oxygen atoms, high temperature annealing or ion-beam bombardment (ion sputtering) cleaning procedure are in general inappropriate since they almost change the surface composition by either "outgassing" oxygen from the surface region or preferentially sputter the oxygen atoms so that the surface region becomes oxygen depleted.

The mechanical removal of surface layers through UHV, fracturing (cleaving), milling, scraping or brushing with a hard metal brush (tungsten) is attractive for these compounds. However, it is well known that grain boundaries are often the weakest part of the sample, also bulk

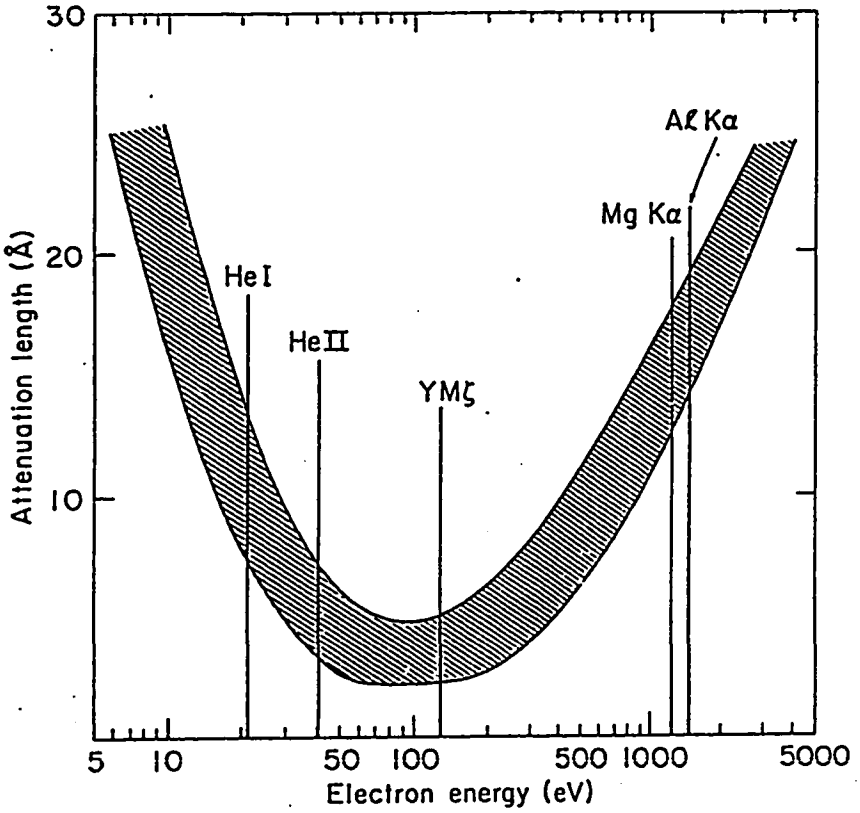

Fig. 3.10 Universal Curve.

contamination and impurities tend to accumulate at these boundaries. So, it is important that ceramic materials be sintered to a high degree of compactness to avoid the preferred sample breakage at a grain boundary upon in-situ scraping or in-situ cleavage. With these precautions, the chemical composition of an in-situ scraped ceramic material surface can be representative for that of the bulk.

Besides the difficulties in preparing bulk-representative surfaces, the character of some of high-T_c superconductors possess a difficult problem in UHV. Although the thermodynamics of oxygen equilibrium in Y123 suggests a large heat of desorption for oxygen [180] which implies that samples should be stable in UHV for a considerable time, experiments show that sample surfaces deteriorate or change after prolonged exposure to UHV [181-182]. The deterioration of the surface in UHV is believed to be caused by oxygen outdiffusion from the sample, thus depleting the oxygen content at the surface.

In the present work samples of Y123 superconductor in pellet form (10 mm diameter) were mounted to sample holders "stubs". To mount the sample, small groves were made in the sides of the pellet then, the pellet was fixed onto the stub by clamping it through the groves with small strips of tantalum which were spot welded to the stub. Thereafter samples can be introduced to the system through the fast entry air lock chamber.

On the as introduced surface, the only contaminations which

could be detected by core level spectroscopy was a few percent of carbon and its compounds CO or CO_2, probably due to adsorption of these gases at inner surfaces of the not completely dense samples or due to the residual not decomposed carbonate from the starting material used to prepare the samples.

This dirty surface can be cleaned in the preparation chamber by means of a diamond file where the top surface layers are removed completely. Furthermore, the freshly prepared surface was scraped by a stainless steel plate to confirm the cleanliness of the surface. While sample surface cleaning was done in UHV ($P < 5 \times 10^{-10}$ mbar) at room temperature, the pressure was monitored in the preparation chamber and there was no change in the chamber pressure which means that the sample does not outgas (lose oxygen) during scraping. After scraping, the specimen surface stayed clean for more than one day (which is more than the time required for collecting spectra). Moreover, no change was observed in O1s peak after this time which indicates the sample stability through the experimental run time. As the sample stays for longer time minor changes begin appearing in the spectra from the surface and increase with time till the surface becomes dirty, probably because of both the diffusion of the adsorbed CO or CO_2 gases to the surface or the accumulation of residual hydrocarbons resulting from pumping oils used in the system and oxygen desorption from the surface. A representative clean surface can be reproduced again by another scrap of the sample surface.

3.6 Data Acquisition

Core level and valence band spectra for various high T_c Y123 superconductor samples were taken with different treatments. Also, X-ray induced Auger Electron Spectroscopy (XAES) measurements were performed. All the spectra were recorded at room temperature using both Al K_α and Mg K_α lines for XPS studies and both He I and He II lines for UPS studies. The spectra were studied for the sample as introduced to the system and for clean surfaces, as well as before and after each treatment. Each experimental run for a particular case was conducted more than once. All the obtained spectra were reproducible.

The excitation X-ray gun was fed with the same electrical power (130 W) to insure the same photon flux in all XPS runs. In the case of UPS runs, the discharge lamp was optimized to get the maximum HeII portion in the UV radiation. For this purpose the lamp was run at the minimum gas pressure $\sim 5 \times 10^{-4}$ mbar. Moreover, the spectrometer was set at a well defined sharp peak, usually Ba 3d peak with binding energy $\approx$780 eV, and the sample position was optimized to get the maximum count rat at this peak.

Data for all spectra were accumulated at fixed constant pass energy of the analyzer of 10 eV for XPS studies and of 5 eV for UPS studies. XAES measurements were carried out in the undifferential pulse counting mode using a pass energy of 20 eV. The width of each scan is divided into run-steps of 0.1 eV for both XPS and XAES studies and of

0.05 eV for UPS studies. The collection time of each step (channel) is one second. Each run consisted of many scans divided into regions lasting from one t two hours for UPS experiments and from 12 to 16 hours for XPS experiments. All spectra were accumulated to a minimum of a bout 10^4 counts full scale. A constant background was subtracted using the VGS 5000 data system routines for that purpose. These are based on Shirley's methods [183] and the algorithm of Proctor and Sherwood [184]. The data was subsequently smoothed using appropriate routine of the same data system software which contains different smooth routines: a 3, 5 or 7 point smoothing [185] and extended smoothing routines which is either a quadratic/cubic or a quadratic/quintic function following the algorithm of Proctor et al [186]. The smoothing method used for all obtained data was the quadratic/cubic method in which the values for the end points are extrapolated in such a way that no data points are lost. This is found not to alter the spectral features at all. All spectra shown were normalized to the same maximum height.

With the purpose of being consistent, all energies are reported with reference to the C 1s line at 285.0 eV. The energy of various prominent peaks were determined after non linear background subtraction. The overall accuracy in the determination of the peak position is $\leq$ 0.2 eV.

CHAPTER 4

RESULTS AND DISCUSSION

4.1 Sample Characterization

4.1.1 Transition Temperature

A representative plot of the data obtained from resistivity measurements for different Y123 superconductor samples is given in Fig. 4.1 . This figure shows the variation of resistivity as a function of temperature. As seen from the figure the electrical resistance of the samples varies linearly in the normal state (above T_c) which indicate the metallic behavior of the sample in the normal state. Furthermore all the different samples studied showed sharp superconducting transitions having widths of about 1K to 1.5 K and zero resistance temperature ($T_{c(zero)}$) lying in the range from 90K to 94 K.

The above mentioned observations indicate high quality samples

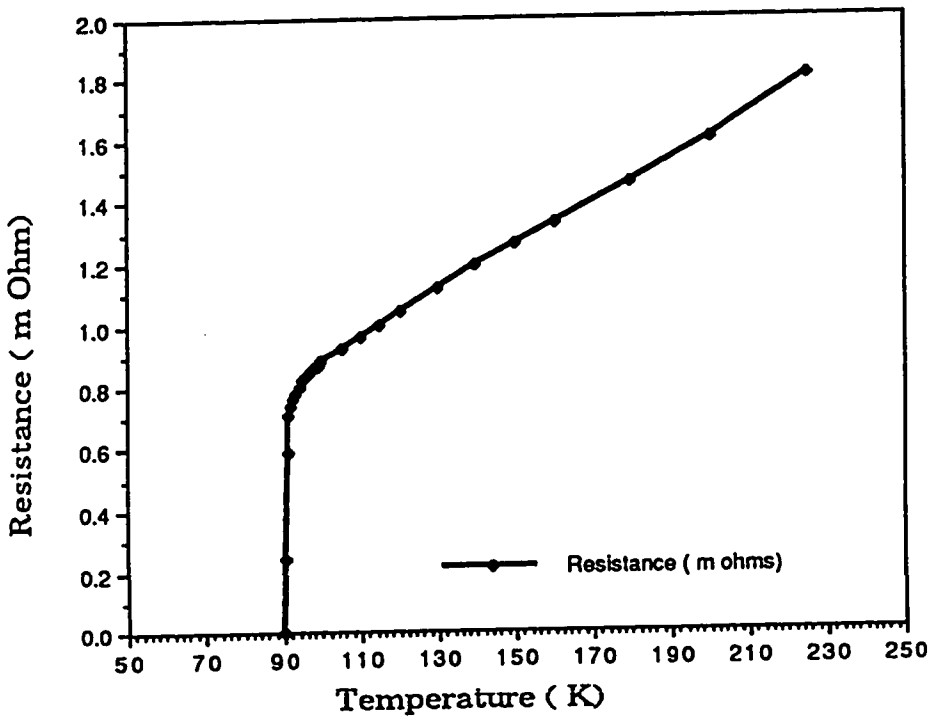

Fig. 4.1 : Representative plot of temperature dependence of the resistance for Y123 ceramic samples.

and support the conclusion obtained from XRD study that samples have a single phased orthorhombic structure.

4.1.2 X-ray Diffraction Analysis

The crystal structure characterization and analysis of the samples have been done by X-ray diffraction technique. The diffraction patterns obtained from the pellet samples were similar. In Fig. 4.2 we show a representative XRD pattern of the Y123 samples used in the present photoemission studies.

X-ray diffraction patterns were analysed using PDP(1.1) (Powder Diffraction Package) written by M. Calligaris and S. Geremita, University of Trieste, Italy. The pattern was first indexed using the indexing program in the package. The results are listed in Table 4.1 . The results do agree with the published data for the $YBa_2Cu_3O_7$. All the observed peaks have been indexed to the orthorhombic phase wit crystal symmetry Pmmm. The crystal symmetry, observed d-values, Miller indices for the observed peaks were then used as an input data for the program REFINE to retrieve the lattice parameters. This gives the following lattice parameters:

$$a = 3.784 \pm 0.0004 \text{ Å}$$

$$b = 3.829 \pm 0.0007 \text{ Å}$$

$$c = 11.552 \pm 0.0016 \text{ Å}$$

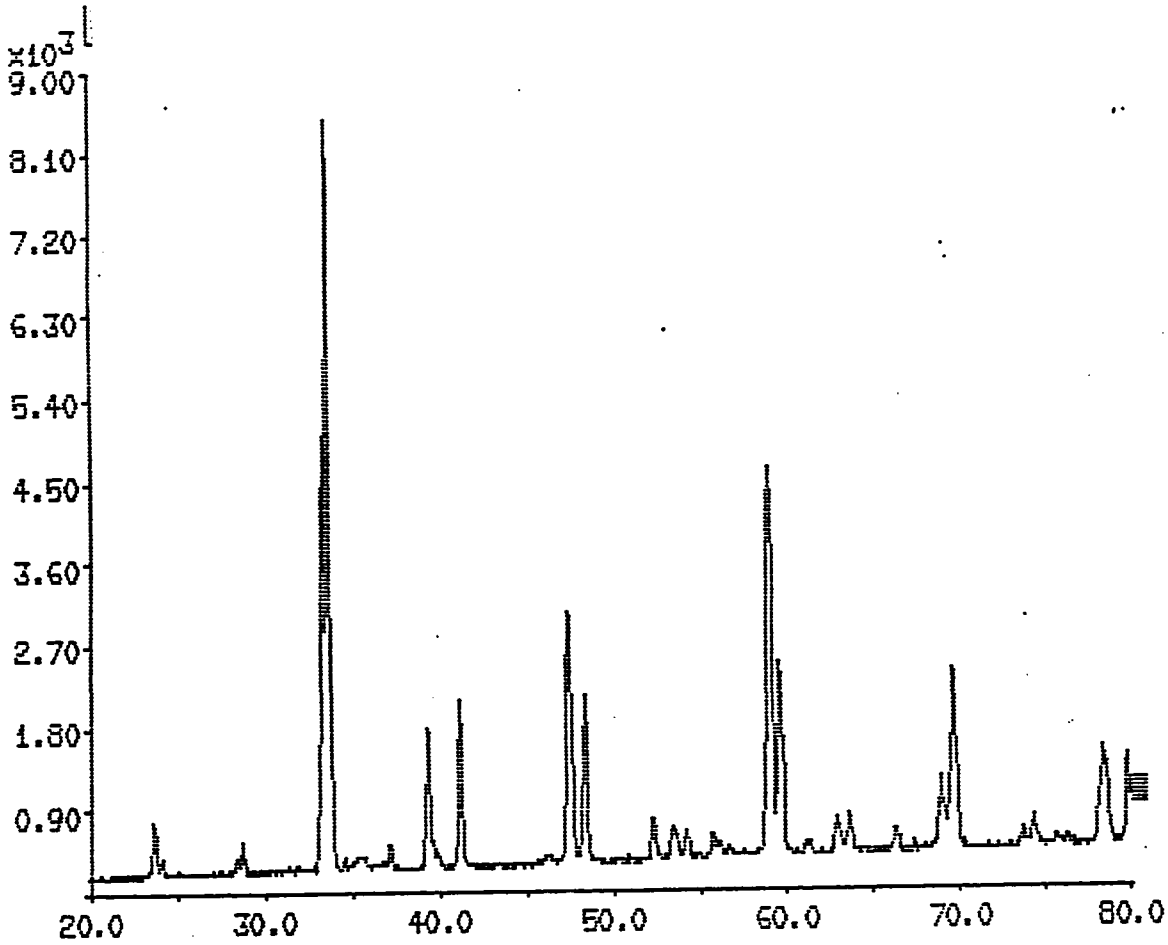

Fig. 4.2 XRD pattern of $YBa_2Cu_3O_{7-x}$ superconductor pellet.

Wave Length = 1.54178 Å				
Indices:				
h	k	l	2θ	d
0	0	3	23.655	3.7581
1	0	0	24.100	3.6897
0	1	2	28.390	3.1411
1	0	2	28.700	3.1079
0	1	3	33.362	2.6901
1	1	0	33.650	2.6612
1	1	1	33.712	2.6629
1	1	2	37.190	2.4156
0	0	5	39.288	2.2913
0	1	4	39.362	2.2928
1	1	3	41.172	2.1907
0	1	5	46.312	1.9588
0	0	6	47.352	1.9182
0	2	0	42.535	1.9159
0	2	1	48.385	1.8796
2	0	0	48.535	1.8788
1	1	5	52.278	1.7485
0	1	6	53.375	1.7151
2	0	3	54.185	1.6913
0	0	7	55.720	1.6483
1	1	6	59.940	1.5657
1	2	3	59.095	1.5658
2	1	3	59.572	1.5506
0	2	5	62.835	1.4777
2	0	5	63.050	1.4768
2	1	4	63.454	1.4620
1	1	7	66.270	1.4092
0	2	6	67.818	1.3631
1	0	8	69.308	1.3547
2	0	6	69.508	1.3546
2	2	0	69.628	1.3492

Table 4.1: Indices of different X-ray diffraction peaks.

As a further check for the crystal structure, and in order to ensure that the sample does not contain any phase other than the high T_c orthorhombic phase, the diffraction pattern of the $YBa_2Cu_3O_7$ was simulated using the refined lattice parameters, point group symmetry, atomic species, atomic coordinates, and atomic scattering factor for all the constituting atoms of the high T_c phase. These information were used as an input data for DEBY program which produces the diffraction spectrum. The results were in very good agreement with the measured spectra. This shows that the samples used in this study are in phased.

There was a small difference in the intensity of few peaks in the calculated pattern. This is due to the fact that the calculations are for samples in powder form, while our XRD measurements were made on a pellet sample. This leads to a preferred orientation in the sample along the c-direction since these high T_c oxides are high anisotropic.

4.1.3 EPMA and SEM Analysis

The analysis was done for the pellets as prepared. Fig. 4.3 shows a representative SEM micrograph of the tested samples taken in the secondary electron image mode with a split screen at magnification of 500X and 2000X while Fig. 4.4 shows another representative SEM micrograph at magnification of 1000X. The grainlike structure of the surfaces can clearly be seen, where irregular shaped grains of sizes ranging from 10 μm to 40 μm are observed. The obtained images confirm that orderly alining exist along the c axis as suggested by XRD analysis. In

Fig. 4.3 Scanning Electron micrograph of the surface of Y123 pellet at 500x and 2000x Mag.

Fig. 4.4 : Same as Fig. 4.3, but at 1000x Mag.

addition, large areas of residual porosity exist at the multi-grain junctions. Y123 grain adjacent to these regions of residual porosity exhibited surface irregularities which might suggest the retreat upon cooling of a liquid phase present at high temperatures.

EPMA showed the presence of the Y, Ba and Cu in the sample without any other detectable impurities. However, the amount of oxygen and contaminant carbon was not obtainable because of the limited sensitivity of the technique to light elements. Table 4.2 summarizes some representative results obtained from different samples. The observed ratio of Y:Ba:Cu (1:2:2.6) showed some deviation from the known atomic ratio 1:2:3, specially for Cu atom, which detected amount was less than expected. These observations can be attributed due to Cu atom loss from the surface layer during sample preparation since CuO vapour pressure (10^{-4} torr at 600 °C) is low compared to other components vapour pressure (Y_2O_3 : 10^{-4} torr at 1500 °C, $BaCO_3$: 10^{-4} torr at 1300 °C). Never the less, after scraping the surface the Cu amount detected by XPS increased, which confirms that the loss is only from the surface layer.

Sample #	YL	Ba L	Cu K
2	17.8	35.5	46.7
3	17.7	35.1	47.3
4	18.1	36.3	45.6
5	17.6	35.7	46.6
7	15.6	35.4	49.0
8	15.5	35.2	49.3

Table 4.2: List of some EPMA results.

4.2 Pohotoemission Study

The general surface analytical features observed from different Y123 and standard material samples (Cu, CuO, Y_2O_3, $BaCO_3$) will be presented in the following sections. The spectra were obtained from Y123 samples prepared by different methods and different starting materials. The spectra labeled A were obtained from samples prepared by co-precipitation solid-diffusion method and the spectra labeled B and C were from samples prepared by the solid state reaction method using barium carbonate and barium peroxide respectively. No major differences were noticed between the features of the three different groups. This implies that there is no significant dependence of Y123 superconductor photoemission on the starting material used for its preparation or the preparation method.

Fig. 4.5 shows a typical XPS wide scan of a $YBa_2Cu_3O_{7-x}$ sample scraped in situ. Besides the expected core levels, no significant contributions from any impurity were detected. The spectra exhibits the strongest core lines of the individual components: Cu 2p, Ba 3d, O 1s, Y 3d, Ba 4d, and Y 3p along with a very small C 1s signal. The X-ray excited Cu (LMM), O (KLL), and Ba (MNN), Auger transitions also appears clearly in the spectra.

Auger transitions were separated from core level ones by comparing the EDC's measured using Al K_α and Mg K_α radiations. The

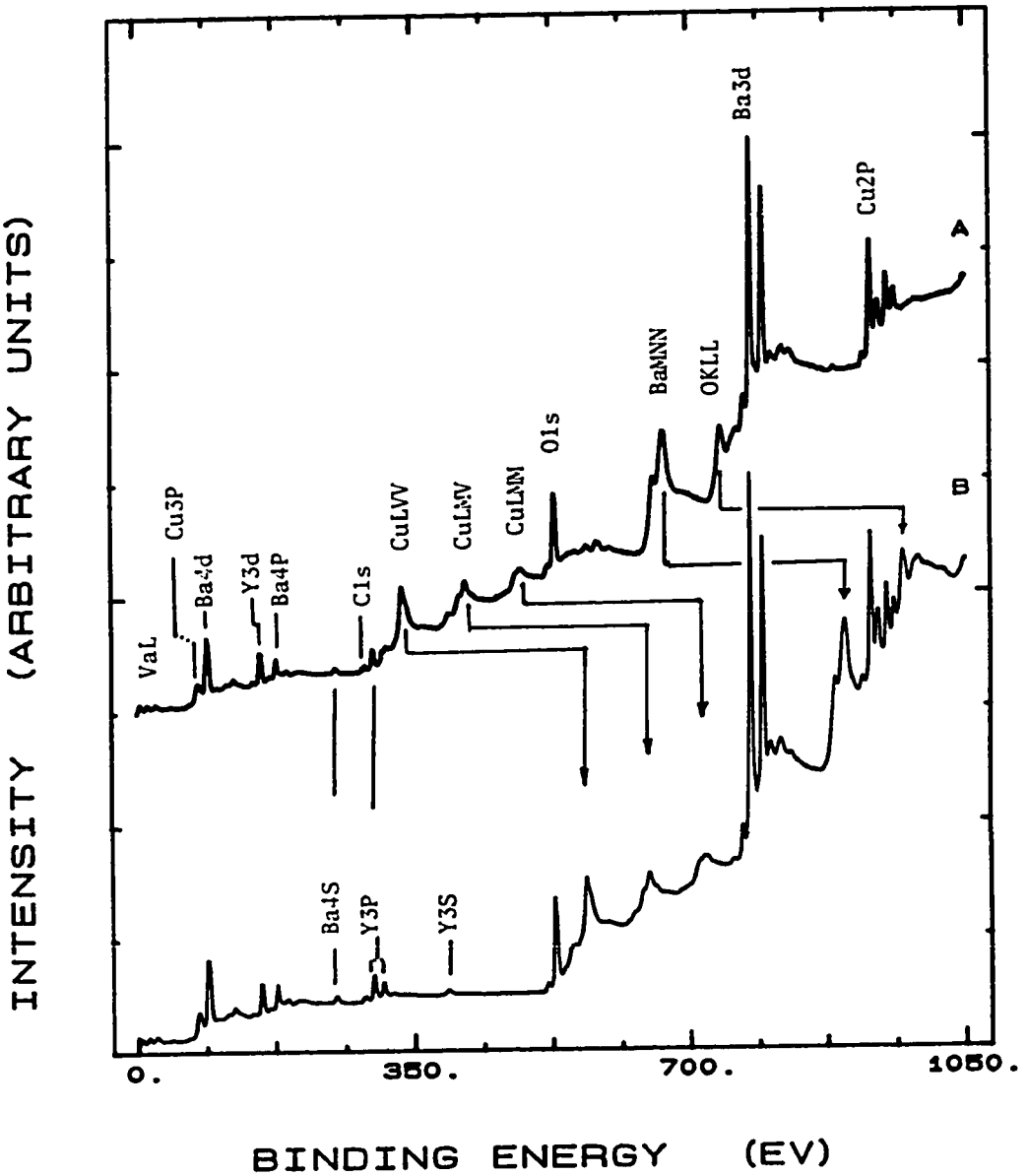

Fig. 4.5 Wide scan XPS spectra of Y123 excited by a) AlK_α (1486.6 eV) radiation and b) MgK_α (1253.6 eV) radiation, (notice the shift of the x-ray induced Auger peaks).

shift of the Auger peaks by the difference of the two excitation energies is indicated in the figure.

Analysis and discussion of the high resolution scans for individual components will be given in the following sections. A discussion of the effect of different sample treatments will also be discussed.

4.2.1 Valence-band (VB) Spectra

Valence-band photoemission spectra were obtained for Y123 by using both X-ray and ultraviolet radiations. In Fig. 4.6 we show representative EDC's for the valence band and shallow core levels of different Y123 samples excited by Al K_α radiation compared with the ones of CuO. The same spectra obtained by using He I and He II radiations are shown in Fig. 4.7 and Fig. 4.8 respectively.

The X-ray induced valence band shows a wide unresolved features centered around 3.5 eV. These features are dominated by the Cu 3d and O 2p derived levels with the copper d-band maximum below the oxygen 2p band maximum. Also as can be noticed from the spectra the intensity close to the Fermi level is very small. The other common features appearing in these spectra are the Ba 5p derived states with a broad peak centered around 13.0 eV with clear shoulders at lower and higher binding energies and Ba 5s level at about 28 eV. The O 2s and Y 4p states can be identified at binding energy of 20.0 eV and 23.7 eV respectively. The O satellite around 9.5 eV appears as a low energy shoulder for the Ba 5p

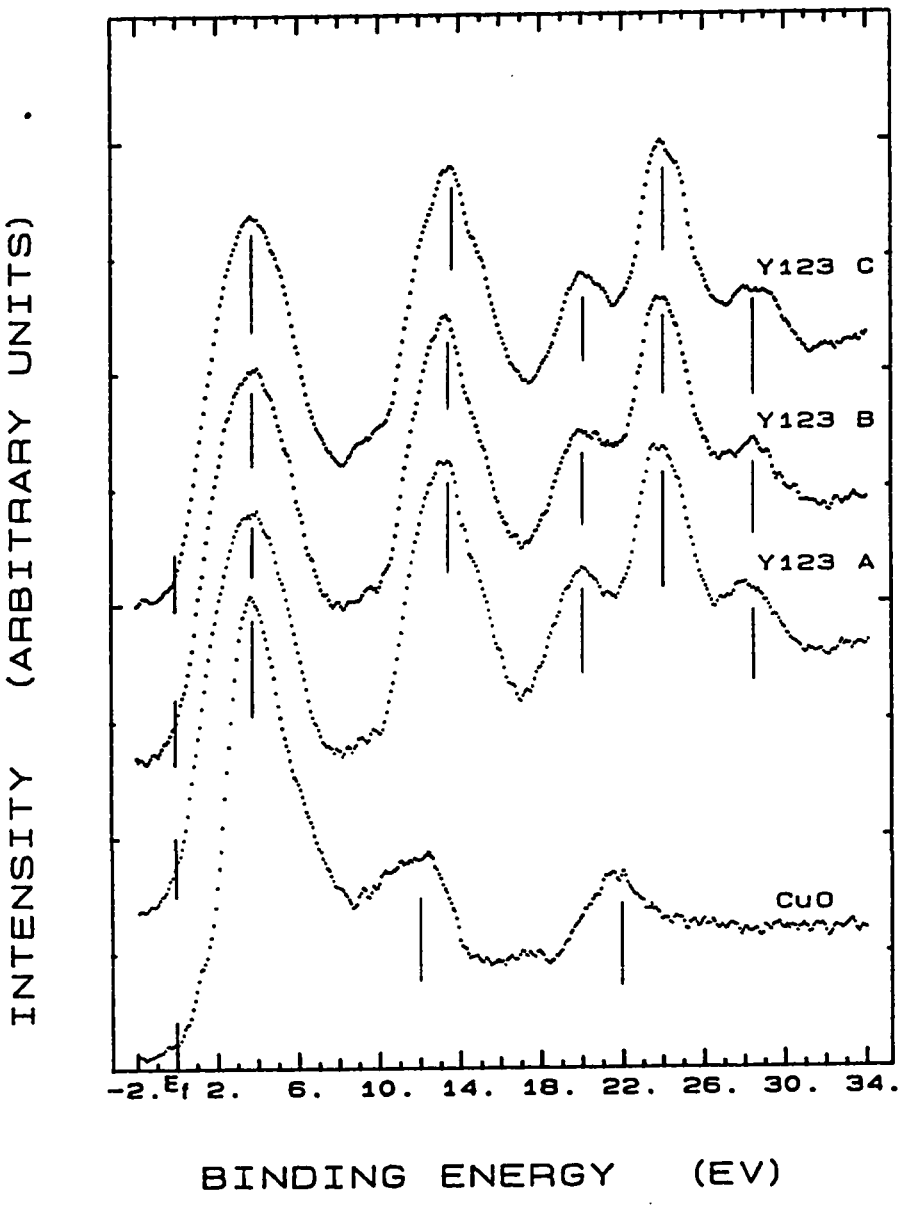

Fig. 4.6 Valence band spectra excited by AlK_α (1487 eV) for three different samples of Y123 prepared by A)solid diffusion method, B) Coprecipitation method from $BaCO_3$ and C) Coprecipitation method from barium peroxide; compared to the valence band spectrum of CuO.

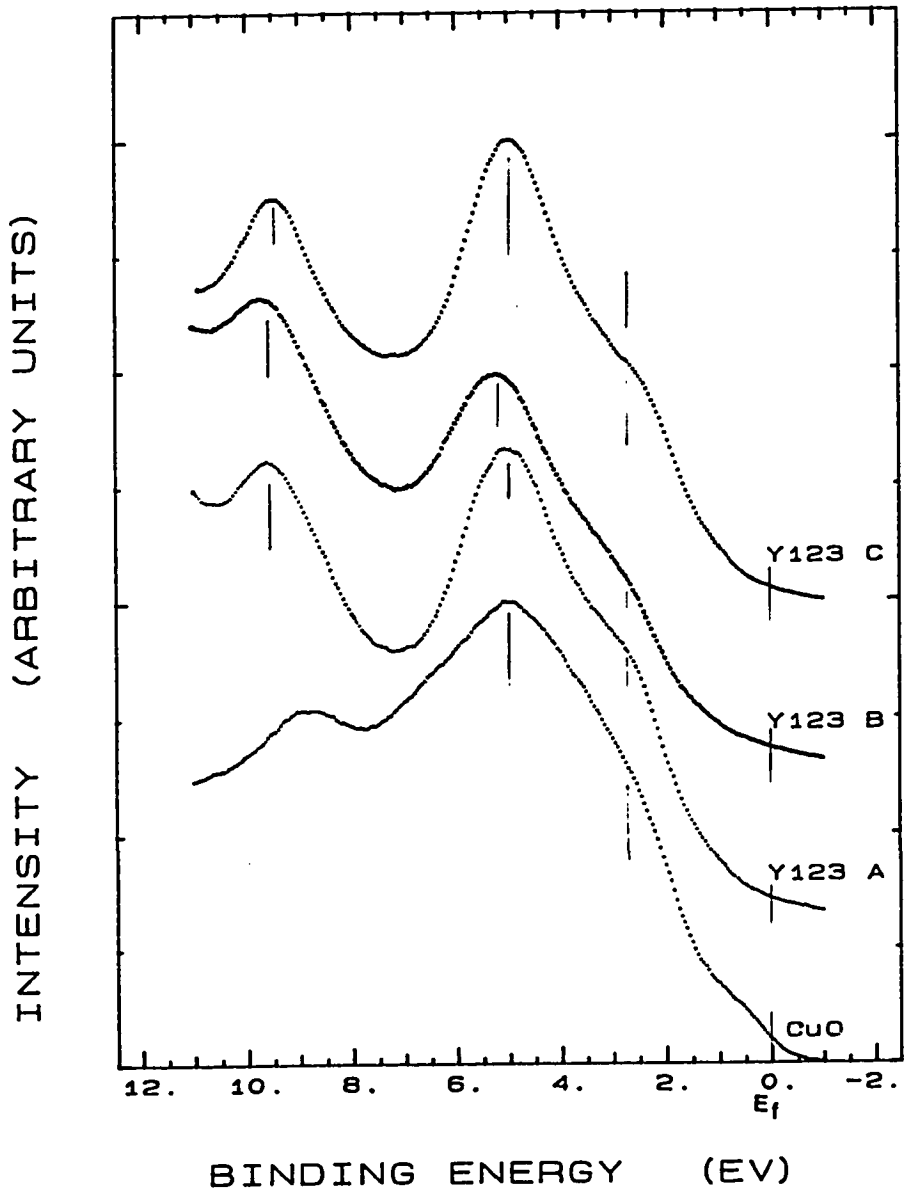

Fig. 4.7 Valence band spectra of different Y123 samples measured with He-I radiation (21.2 eV) compared to that of CuO; (A-C same as in Fig. 4.6).

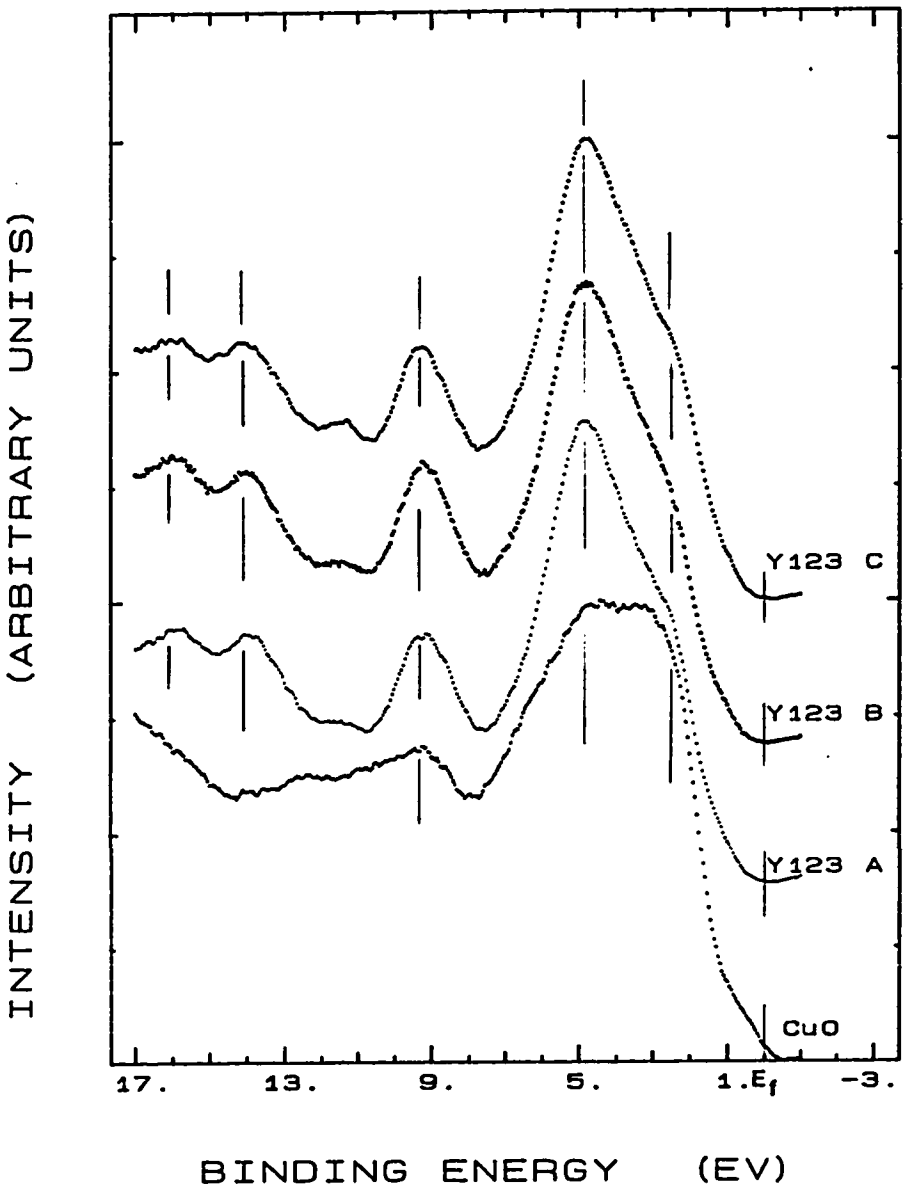

Fig. 4.8 Same as Fig 4.7 except measured with He-II radiation (40.8 eV).

peak while the Cu satellite around 12.5 eV is completely overlapped by this peak.

The He I spectra (Fig. 4.7) have a strong central peak at 4.8 eV with a clear shoulder at 2.7 eV and a small shoulder at about 6.3 eV binding energies. The O satellite is obvious at 9.35 eV.

He II spectra (Fig. 4.8) are similar to He I spectra and extend to a higher binding energy. The main valence band is centered at 4.8 eV with shoulders at 2.7 eV and 6.3 eV energies. The O and Cu satellites are observed at 9.3 eV and 11.4 eV respectively, while the Ba 5p spin orbit split appears at 14.0 eV and 15.8 eV binding energies.

The Y123 system valence band photoemission have been extensively reported by using different photon energies [187-208]. Naturally, much attention has been paid to the emission in the vicinity of the Fermi level where the states that may participate in superconductor pair formation are found. As in the present study, most of the studies performed on Y123 system have failed to reveal a significant emission at the Fermi level, regardless of the temperature at which the measurement was performed. In Fig. 4.9 we compare the obtained He I and He II spectra from a UHV-scraped sample of Y123 with the photoemission spectra calculated by Redinger and Co-workers [209] using LDA energy bands. As seen in the figure, in contradiction with the calculated LDA spectra, experimental spectra are gradually tailing off as approaching the Fermi level without any sign of Fermi level cut-off.

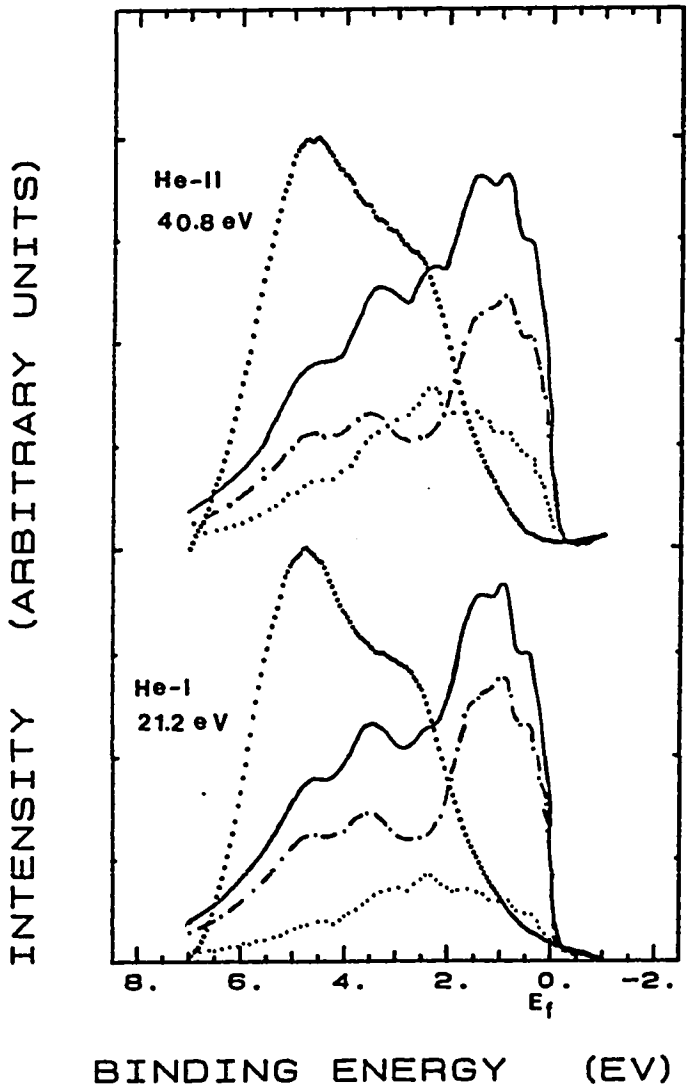

Fig. 4.9 Comparison of experimental valence band spectra taken with He-I and He-II rediations for $YBa_2Cu_3O_{7-x}$ with the calculated spectra of Redinger et al.[209]; calculated (x=0):_____ total; _.-._.-._ O-p ; ..... Cu-d ; experimental (x>0) : ••••••

The main valence band shows two main structures, a structure around 2.7 eV which can be associated mainly with O 2p character, and a structure around 4.8 eV with mainly Cu 3d character. This identification is supported by the band structure calculations and the observed changes in the relative intensity of these two peaks with different photon energies [123,210]. Band structure calculations [166,209,211-213] have predicted that, the major part of the partial density of states for the O 2p orbitals is located close to the Fermi level above the Cu 3d partial density of states.

As noticed in Fig. 4.9, the experimentally observed main valence band is shifted to a higher binding energy in comparison with the calculated ones. The difference between experimental and theoretical spectra has been suggested to be due to : (a) surface may not be representative of the bulk and (b) oxygen deficiency in the samples [201,204,206]. However, these discrepancies can be attributed as indication of the presence of localization and high correlation effects on the Cu 3d and O 2p hole levels. Inclusion of correlation in the theoretical calculations of Calandra et al [211] causes the same effects where the intensity in the region between E_F and 2 eV has been dramatically reduced, the center of gravity of the main valence band has been shifted to higher binding energy and the Cu $3d^8$ satellite around 12 eV has appeared.

Comparing the experimental VB spectra excited by He I and He II lines showed that the spectra do not strongly depend on the photon energy. At He I photon energy, the O 2p photoionization cross-section

(10.67) is larger than the Cu 3d photoionization cross-section (7.553) and the ratio is 1.413; while the situation is reversed at He II photon energy where the O 2p photoionization cross-section (6.816) is smaller than the Cu 3d photoionization cross-section (9.934) and the ratio becomes 0.686 [214]. However the ratio of the two valence band peaks stays approximately the same. This not very pronounced energy dependence of the valence band indicates that the Cu 3d and O 2p states in the valence band are strongly mixed (hybridized) which means that the system is highly covalent and one cannot simply separate the Cu and O contributions.

The valence band Cu satellites are not easily seen in the photoemission data from Y123 because of the interference from Ba $5p_{3/2}$ level. However it can be observed as a small peak centered around 11.4 eV and as a low binding energy tailing for the Ba $5p_{3/2}$ state. In resonance photoemission studies [187,188,190,191,206,215] a well defined copper satellite showing resonance enhancement at hν = 74 eV has been found in the range of 12.3-12.9 eV in data obtained from both single-crystal and polycrystalline samples. The 12.4 eV valence band Cu satellite is not accounted for by band structure calculations and indicates a strong correlation effect. This satellite may be associated with a Cu $3d^9$ final state structure created out of the Cu $3d^8$ initial state and the separation between this satellite and the top of the valence band gives an order of magnitude estimate of the d-d correlation energy, $U_{dd} \approx 6$ eV.

In addition to the 12.4 satellite, a very clear satellite peak appears at 9.4 eV. It was observed that this peak is very strong for contaminated surfaces. Although, this peak is reduced by scraping but it is still observable in the spectra from clean surfaces. The presence of this peak has been reported by several groups but the origin of this peak was one of the most controversial topics [188,190,191,208]. The presence of this peak in both single-crystal [188,190,191] and polycrystalline results implies that this peak has some intrinsic origin. Moreover, some groups [187,191] have reported resonant behavior for this peak at photon energies near the O 2s excitation threshold. This behavior suggests an oxygenic origin of this satellite. Other groups maintained that the 9.4 eV feature is due to surface contamination [216,217].

It has been proposed that this feature (or part of it) may be a two-hole satellite of the O 2p-like subband (O $2p^4$ configuration) which is connected with the Cu3$d^{10}\underline{L}^2$ configuration. The presence of this peak probably also indicates correlation effects [33].

By contrast, Arko et al [206] reported the absence of the 9.4 eV satellite from the data taken from Y123 single-crystals cleaned at 20 K, but this peak grows rapidly as the crystal is allowed to warm to room temperature. This behavior can lead to the suggestion that the 9.4 eV satellite is associated with adsorbed oxygen or interstitial oxygen derived from the bulk crystal.

It seems that this peak has both carbon-induced and intrinsic

components. Evidence for the carbon induced component comes from the dependence of this peak in the surface state. This peak noticeably decreases after cleaning the surface, and for clean surfaces it showed some sort of correlation with C 1s peak. The energy of this peak is typical for C 2p emission of carbon contamination. Evidence for the intrinsic component is that the intensity of this peak remains high even when C 1s emission is very low and also the presence of this peak in samples not prepared from carbonates. It seems likely that the intrinsic contribution involves oxygen states such as those proposed by Winden [218].

In order to interpret the valence band photoemission spectra, it has been suggested [187,208,215,218] that a configuration-interaction (CI) approach may be more appropriate way to describe these materials than the one-electron band models. In this CI cluster scheme, the emission of a photoelectron from the N=9 ground state produces the two-hole excitation spectrum for N=8, Fig. 4.10 . The VB two-hole state is described as a superposition of different states with :- two holes on Cu ($3d^8$ or $3d^2$), two holes on the ligand ($3d^{10}\underline{L}^2$ or $\underline{L}^2$), and one hole on each ($3d^9\underline{L}$ or $3d\underline{L}$). The energies of these configurations will depend on the hole-hole Coulomb interaction U. Thus the main valence band was attributed to final states of predominantly mixed $3d^9\underline{L}$ and $3d^{10}\underline{L}^2$ character, and the satellite at 12.4 eV to an almost pure $3d^8$ final state. The large separation (8.6 eV) between the satellite and the main VB suggests a large value U_d, which implies a high energy for the $3d^8$ configuration and suggests that charge

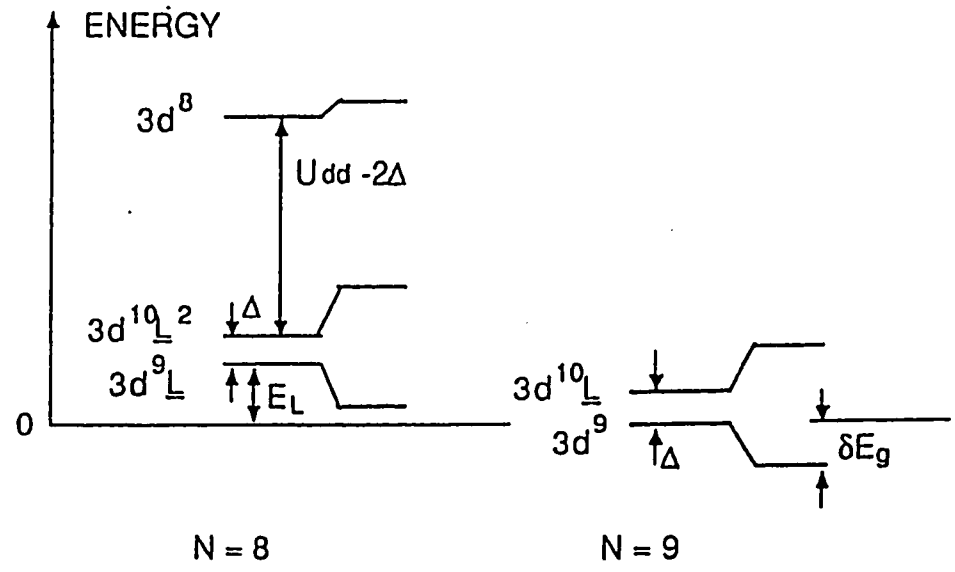

Fig. 4.10 Energy-level diagram for configurations of the cluster model description of the ground state (N=9), and valence band photoemission final states (N=8). The changes in splittings are due to hybridization, [Ref. 187].

fluctuations to Cu^{3+} state are unfavorable.

4.2.2 Core Level Spectra

Oxygen 1s

In Fig. 4.11 a representative O 1s spectra from freshly scraped surfaces of various Y123 samples are shown. Also, a dirty surface spectrum is shown. The spectra contains two peaks one near 528.4 eV and another at about 530.4 eV. The lineshape shown remains unchanged upon further mechanical scraping, however, relative intensity of the two peaks vary depending upon the sample handling. For as introduced (dirty surface) samples the high binding energy component is usually higher than the low binding energy one while the situation is reversed after in situ scraping (clean surfaces). The intensity of the high binding energy peak grows again by exposure to air or water or after a long exposure to UHV.

O 1s peaks have been studied by a large number of groups [24,25]. But unfortunately, their results vary strongly from each other. It is now well established that the low binding energy peak at 528.5 eV is characteristic of the high T_c Y123 superconductor, and for a good Y123 samples this peak must be dominant [198,200,219-224]. However the high binding energy peak has been the subject of intense discussion. After a review of the published results about the O 1s peak Ramaker [225]

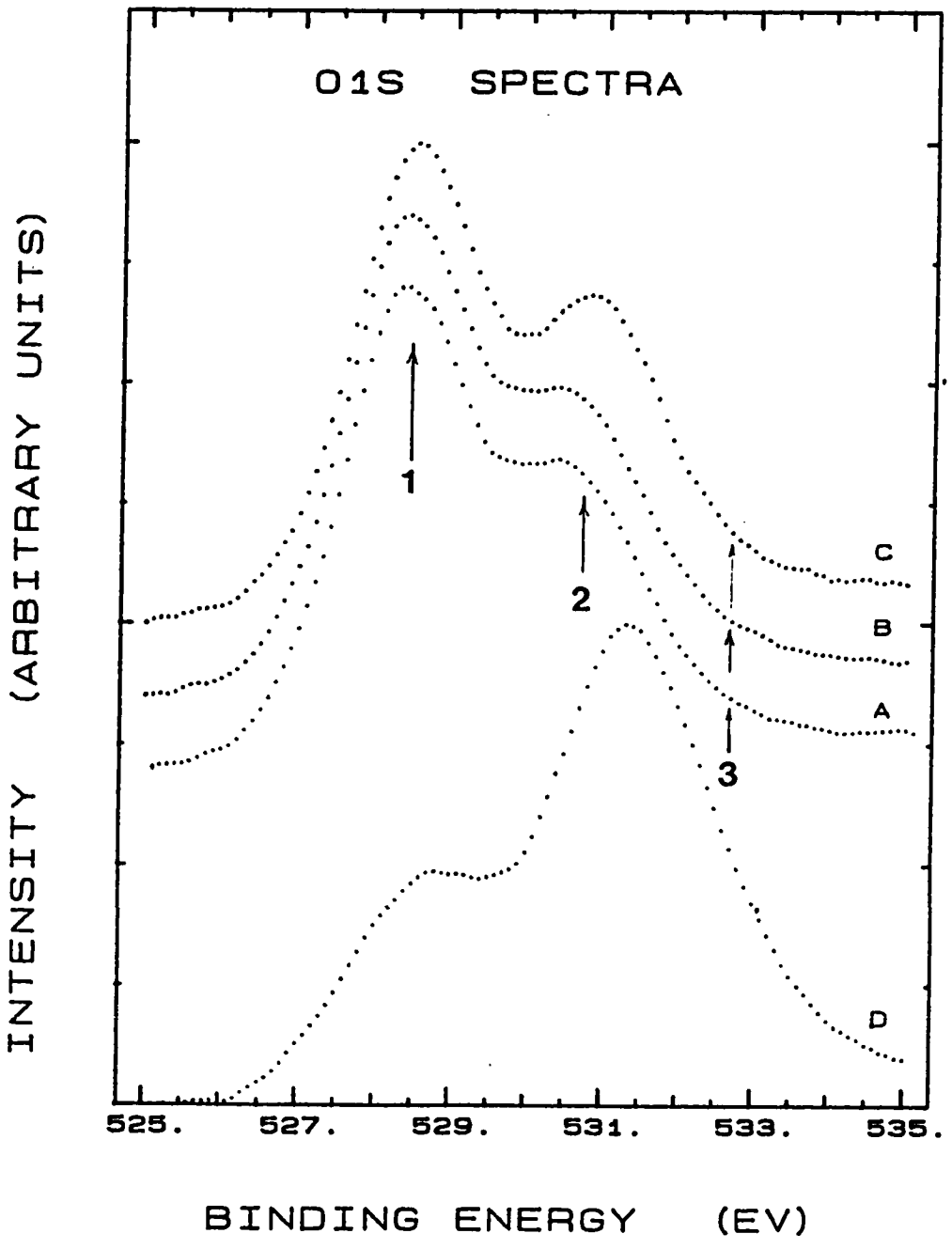

Fig. 4.11 O 1s XPS spectra for several Y123 samples; curves A-C same as in Fig. 4.6, scraped in situ, and curve D for the sample as introduced (contaminated).

concluded that the high binding energy feature arises from adsorbed species, and that all the oxygen sites have similar binding energies. Other authors believe that this peak reflects the holes in oxygen band [222,223]. Some groups have also reported that this peak is a satellite of the main 528.5 eV peak [226] and there is another component at 531 eV due to surface contamination. Other groups consider that the peak between the main line at 528.5 eV and the adsorbate line is a line of molecular ions, superoxide (O_2^{2-}) appears on the surface [227] or peroxide $(O_2)^{2-}$ in the bulk of the sample [228].

While studying O 1s spectra we noticed that the high energy component at 530.4 eV shows a dependence on the photon energy of the exciting radiation. As going from Mg K_α radiation to Al K_α radiation the intensity of this peak shows a noticeable decrease. Since spectra obtained by Mg K_α radiation is more sensitive to the surface layer than those obtained by Al K_α radiation, due to the change of electron escape depth, then this observation implies that the high binding energy peak may be partially related to oxygen near the surface. In O 1s spectra obtained from surfaces cleaned by scraping, three features can be noticed 1) The major feature at 528.4 eV which is attributed to O^{2-} ions in the bulk superconductor, 2) A component centered at 530.4 eV. The origin of this component will be discussed below. 3) Additional signal at 531 eV which has a binding energy comparable to that of O 1s line from $BaCO_3$, so it is proposed that it arises from carbonate contamination mainly at the sample

surface.

As it is noticed the energy of the second peak at 530.4 eV is lower than the energy of O 1s line from expected surface contaminants such as CO_1, CO_2, OH and CO_3 which can be observed from the spectra of dirty surface. Hence, it is suggested that this peak is due to oxygen holes formally described by O^{1-}. The peak at 531 eV can account for the detected residual carbonate signal and for the observed photon energy dependence of the high energy peak.

Interpretation of the O 1s is very complicated since there are different inequivalent oxygen sites as discussed in the crystal structure of Y123. However, according to the model proposed by Winden [218] the 528.4 eV peak can be attributed to $1\underline{s}2p^6$ $[3d^9 + 3d^{10}\underline{L}]$ configuration while the 530.4 eV state is represented by $1\underline{s}2p^5$ $[3d^{10} + 3d^{10}\underline{L} + ...]$ configuration.

Copper 2p

A typical Cu 2p XPS results for different Y123 samples are shown in Fig. 4.12 together with the corresponding spectra for Cu foil and CuO powder accumulated under the same experimental conditions. The spectra consist of spin-orbit split Cu $2p_{3/2}$ and Cu $2p_{1/2}$ components at 933 eV and 953 eV binding energies respectively. Satellites associated with these two components appear at 8.7 eV higher binding energies. The Cu

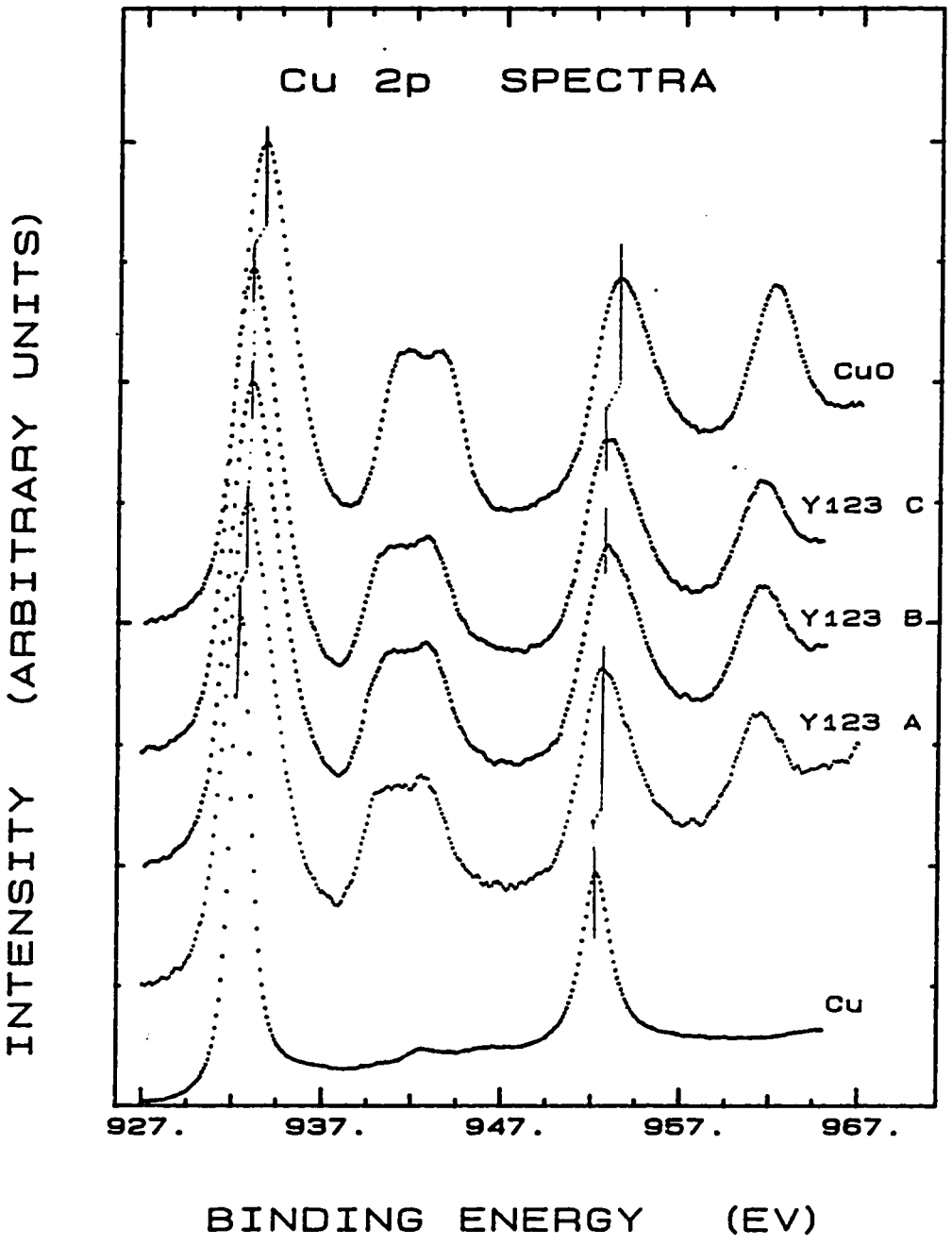

Fig. 4.12 Cu 2p XPS spectra for different Y123 samples scraped in situ with the corresponding spectra for Cu metal and CuO, A-C same as Fig. 4.6 .

2p line shape of the Y123 compares with those of pure ionic divalent compounds [230,231]. The presence of intense satellite peaks indicates that the oxidation state of Cu is largely Cu^{2+}. Also as noticed in Fig. 4.12, the Y123 Cu $2p_{3/2}$ peak is shifted to a lower binding energy relative to Cu $2p_{3/2}$ peak of CuO at 933.6 eV . However, it still at binding energy higher than that of the corresponding peak of metallic Cu at 932.4 eV or Cu_2O at 932.2 eV [229]. Since it has been observed [228,236] that the chemical shift of the Cu $2p_{3/2}$ line increases as the Cu valence state or CuO increases, then the intermediate chemical shifts of the Cu $2p_{3/2}$ line from Y123 samples indicate that the oxidation state of Cu in these samples is less than that of CuO which provides additional evidence that Cu^{3+} does not occur. A closer inspection of the spectra exhibits two main spectral differences between CuO and Y123 XPS results. Firstly, the FWHM value of Cu $2p_{3/2}$ main line for Y123 (3.1 eV) is slightly smaller than the value for CuO (3.2 eV). Secondly, the intensity ratio I_s/I_m of the satellite peak intensity (I_s) to the main peak intensity (I_m) for Y123 (35%) is lower than that for CuO (54%). These findings support the above conclusion that the Cu valency is lower than 2+.

The observed Cu 2p spectra can be generally interpreted in terms of the ligand-to-metal charge transfer model [230] which includes configuration interaction. According to this model, the main peaks are attributed to the ligand screening of the 2p hole via the final-state configuration $2\underline{p}3d^{10}\underline{L}$ whereas the satellite structure is assumed to reflect

the multiplet structure resulting from the interaction of 2p hole with the $3d^9$ valence electrons in the $2\underline{p}3d^9$ final-state configuration. Here, $2\underline{p}$ indicates a hole in the 2p core state and $\underline{L}$ denotes a hole in the ligand bond [187,215,232,233]. The intensity of the main peak results from the presence of some $3d^{10}\underline{L}$ component in the ground state and also from an O to Cu charge transfer induced by the creation of a core hole. The width of the main peak is believed to be due to satellite contributions and intrinsic Op($\underline{L}$) band width [234] while the width of the satellite peak is due to multiplet effect [233,234]. Furthermore, the satellite to main peak intensity ratio (I_s/I_m) is closely related to the respective weights of the $2p^63d^9$ and $2p^53d^{10}\underline{L}$ configurations in the ground state [218,230,235]. The separation between the main peak and the satellite is given approximately by the intraatomic Coulomb repulsion U_{cd} between a Cu 2p core hole and 3d hole. For most 3d transition-metal compounds $U_{dd}/U_{cd} \approx 0.7$ has been reported [215,232,238]. Hence the observed $U_{cd} = 8.7$ eV leads to $U_{dd} \approx 6$ eV. Same value was obtained earlier from the valence band spectra and also pointed by Fujimari et al [215,232].

The previous analysis only applies to the insulating N=9 state (Fig. 4.10). In the metallic regime additional feature due to the final state $2\underline{p}3d^{10}\underline{L}^2$ may appear at the high binding energy side of the main peak [234,239,240] because of the presence of some additional O p holes.

Using the satellite-to-main line intensity ratio and the peak energy separations one can calculate the ground state d-electron

occupation number n_d, the Cu-O charge transfer density, the effective Coulomb interaction U_{dd}, and other parameter. In this way Shen et al [187] find an average 3d occupation $n_d \approx 9.4$ for $YBa_2Cu_3O_7$.

Barium 3d and 4d

Experimental Ba 3d spectra of the Y123 samples are given in Fig. 4.13 . The $3d_{5/2}$ level is centered at 779.6 eV and the $3d_{3/2}$ level is centered at 15.3 eV higher binding energy. All Ba peaks in Fig. 4.13 show asymmetric low binding energy shoulder which indicate the presence of at least two differently charged Ba ions. The same conclusion can be obtained from Ba 4d spectra shown in Fig. 4.14 . Each Ba 4d spectrum appears to be composed of overlapping unresolved pairs of spin-orbit split peaks from different Ba ion states. The spectrum is centered at about 88.8 eV with a clear shoulder at 2 eV higher binding energy.

It is well established experimentally [241-259] that at least two barium components contribute to the XPS core level spectra of Y123. However, the precise energetic position and the physical origin of these two components, as well as the shape of the Ba 3d and Ba 4d core lines have not yet been considered in detail. By studying the dependence of the peak intensity on the photoelectron take-off angle, many authors [241,242,246,258] have concluded that the higher binding energy contribution is associated with a surface component whereas the lower binding energy contribution results from the bulk and is characteristic of

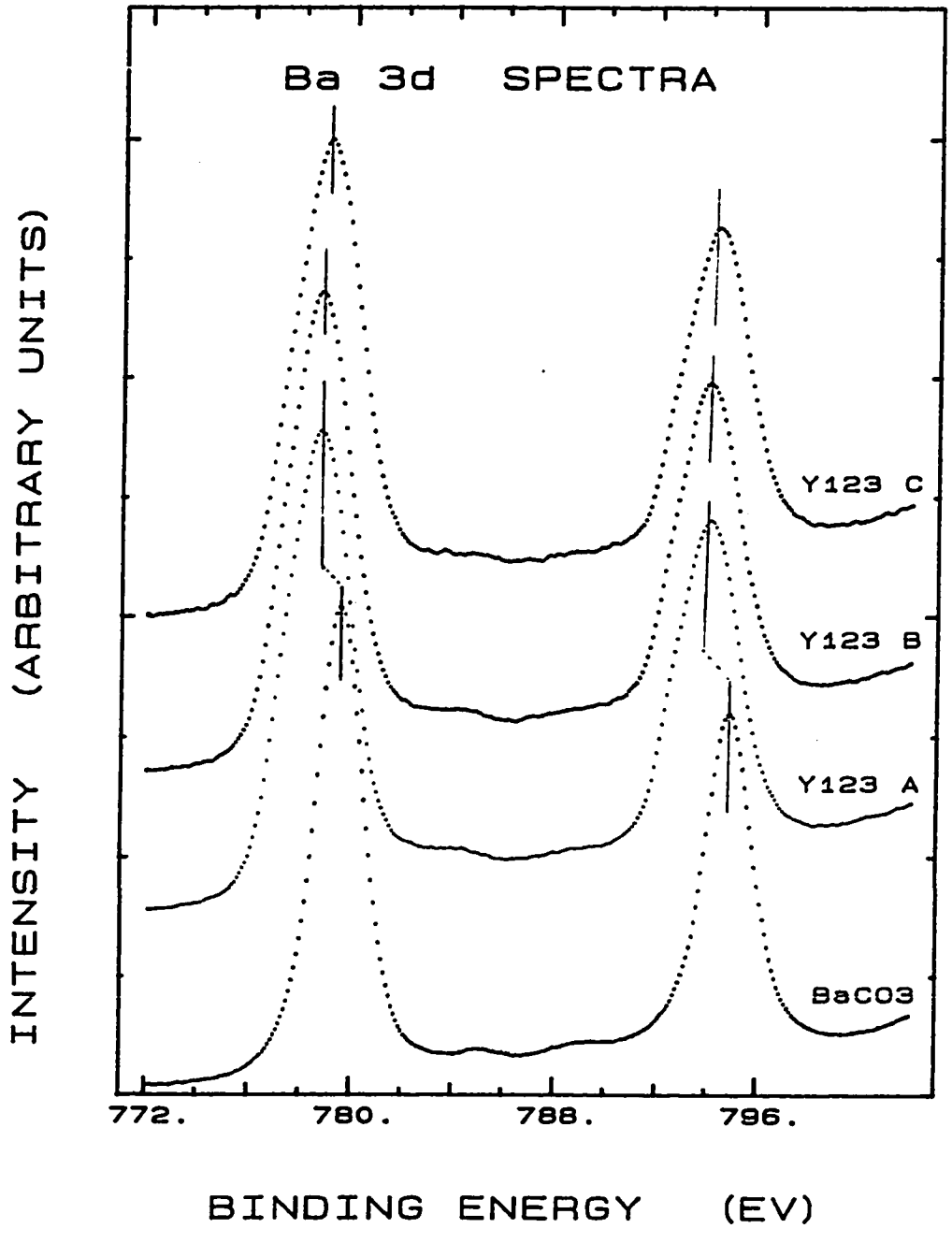

Fig. 4.13 XPS spectra for the Ba 3d region. A-C different Y123 samples same as Fig. 4.6 scraped in situ, and for $BaCO_3$ powder sample.

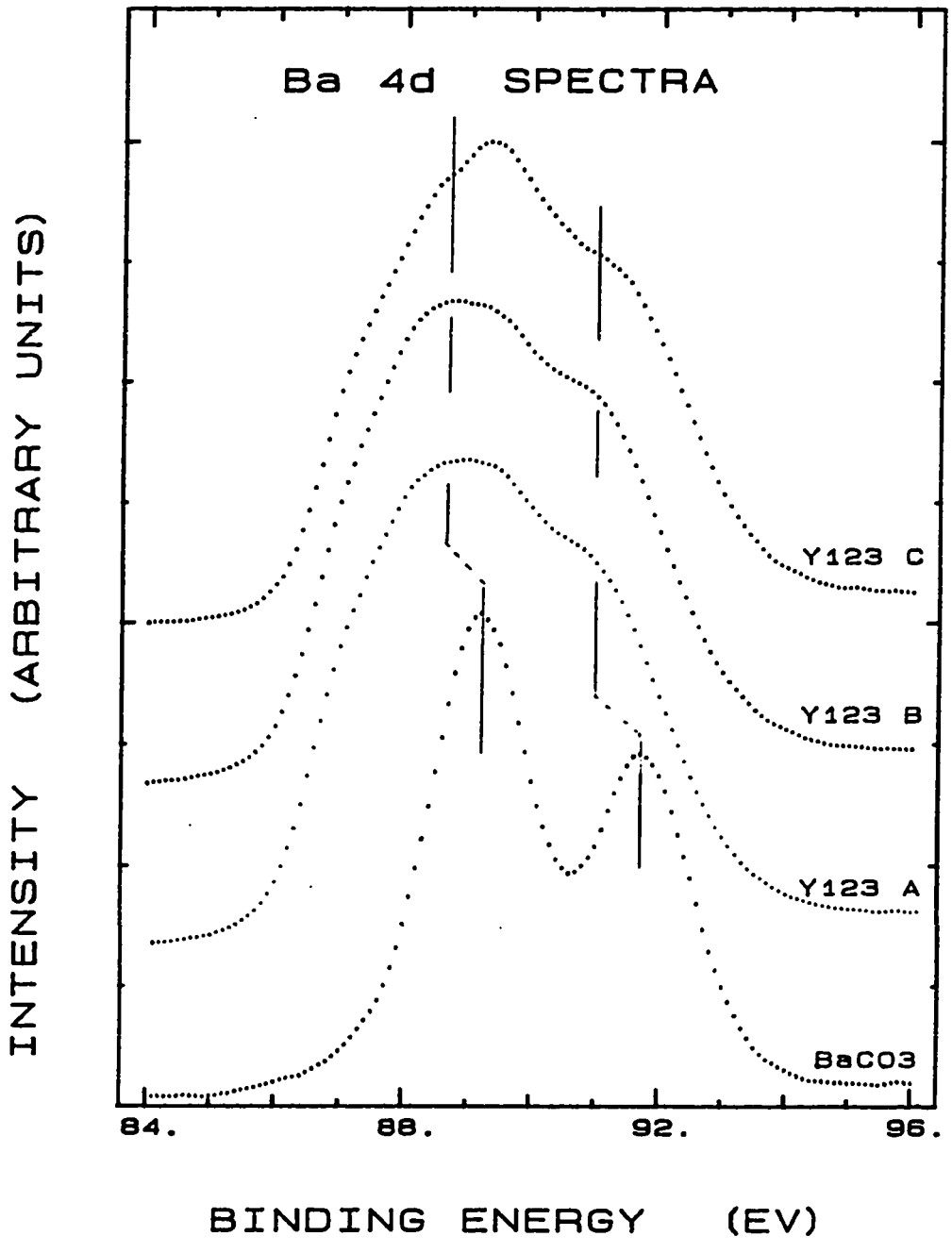

Fig. 4.14 Same as Fig. 4.13 except for Ba 4d region.

the superconducting phase. Others [250] made the opposite assignment of these two components which was based upon their measurements at different low photon energies. Despite the agreement at the origin of low energy component which has been assigned to bulk superconductor Ba ion with perfect oxygen coordination, the interpretation of the extra high energy component have been quite diverse. The high energy component was assigned to Ba ion at oxygen-deficient sites [192,241-243]. The origin of this line was also discussed in terms of coordination properties, final-state relaxation and inclusion [263]. Others pointed out that the different chemical states are due to the valence charge fluctuation of barium atoms [221], or due to surface core level shift [245,246,250]. On the other hand the different chemical states of barium and oxygen were discussed in terms of impurities such as carbonate and hydroxyl groups coming from atmospheric gases or segregated at the grain boundaries [219,247,254].

The observed Ba $3d_{5/2}$ spectra (Fig. 4.13) in the present work are in agreement with the published ones [192,241,249]. For an optimal determination of the components contributing to this spectrum from scraped surface, a careful spectrum decomposition was performed by means of peak synthesis software supplied with the computer. The line was fitted to three components of mixed Gaussian-Lorantzian line shape. The results are listed in Table 4.3 and shown in Fig. 4.15. The above results are similar to some reported values for barium in different chemical states [241,248,255]. The low binding energy peak at 777.3 can be assigned to Ba ions in the bulk which is in an almost perfect oxygen coordination.

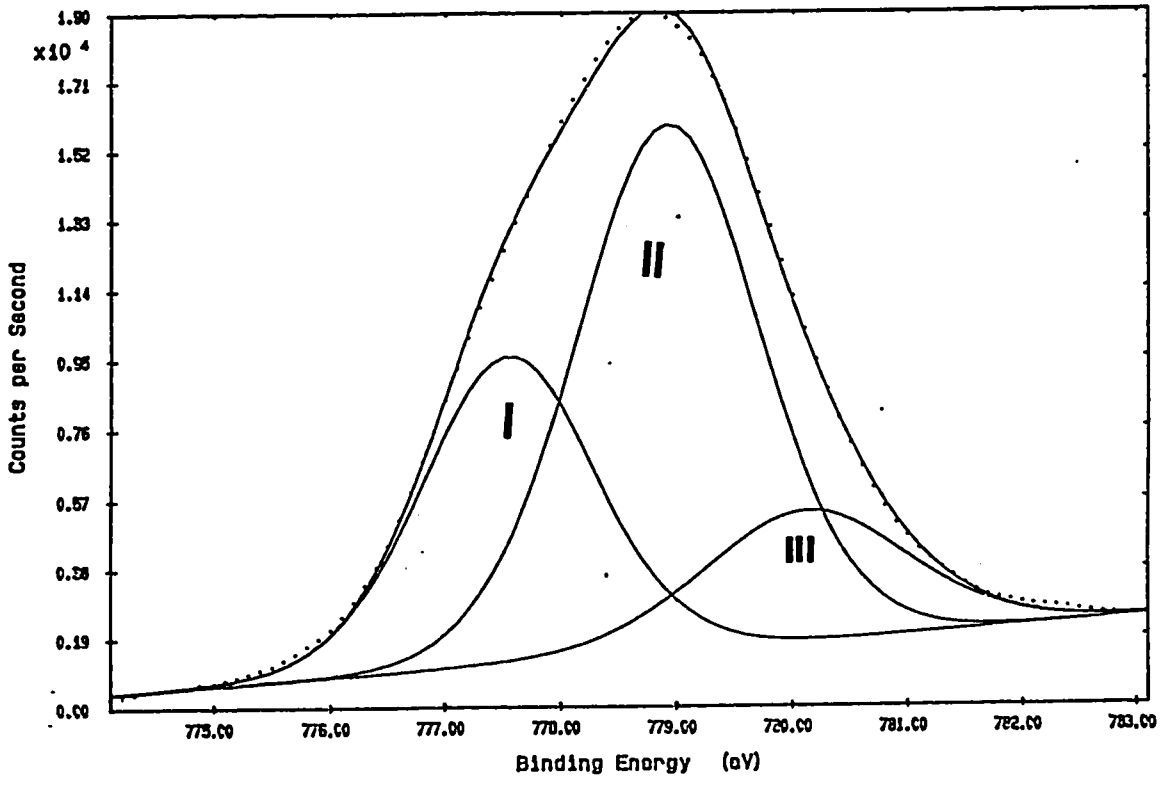

Fig. 4.15 Decomposition of Ba $3d_{5/2}$ peak into its components; I, II, and III are the components, continuous line is the total, while the doted line is the experimental.

Peak #	Energy	FWHM	%
1	777.3	1.74	23.7
2	778.8	2.06	63.1
3	780	2.16	13.1

Table 4.3 : Different components resulting from Ba $3d_{5/2}$ peak decomposition.

The shift of this peak towards a lower binding energy than that reported for BaO [260-262], reflects an enhanced O content because Ba atoms in Ba-O planes, sandwiched between Cu-O layers, are sensitive to O content. Their unique chemical environment is reflected by lower binding energies in the superconductor than in BaO and even shifts to lower energy as the oxygen content increases. The second 778.8 eV peak is assigned to Ba states at the surface layer of the sample in accordance with the published results [241-243]. Since there is a negligible carbonate emission from scraped surfaces compared to this peak, it is easy to state that this component is not associated with surface carbonate. Also the binding energy of this peak is comparable to the binding energy of the same peak in BaO [260-262]. This component seems to refer to Ba ions in an almost distorted oxygen neighborhood. The energy difference between this peak and the lower energy one results from different screening response of the surrounding to the photo hole created at the Ba^{2+} site. The screening energy at Ba^{2+} site coordinated to oxygen vacancies with smaller polarizability is smaller than it is for Ba^{2+} site with a complete O^{2-} coordination. The residual amount of carbonate observed can be safely associated to the third component observed at 780.0 eV. The assignment of the bulk and surface peaks was confirmed by comparing the Ba 3d line taken using Al K_α and Mg K_α radiations. The kinetic energies of this Ba line for Mg and Al radiations are $\sim$ 475 and 708 eV, respectively, and therefore there is appreciable difference in electron escape depth. Running experiments with the two radiations under the same experimental

conditions, the escape depth will be the only parameter that changes. In the obtained spectra the shoulder at low binding energy was more pronounced in Al K_α excited spectrum than the Mg K_α excited one, while the situation was reversed for the higher binding energy components.

Yetterium 3d and 3p

The Y 3d spectra for Y123 and Y_2O_3 shown in Fig. 4.16 consist of a doublet. The $3d_{5/2}$ spin-orbit component occurs at 155.8 eV for Y123 and at 156.4 eV for Y_2O_3 while the $3d_{3/2}$ component occurs at 157.7 eV and 158.2 eV for Y123 and Y_2O_3 respectively. The results exhibit a high binding energy tail and a filling in of the minimum between the doublet peaks. Moreover, the intensity ratio $I(3d_{5/2})/I(3d_{3/2})$ is about 1.3 which is smaller than the theoretical value of 1.5.

In Fig. 4.17 the Y 3p spin-orbit-split doublet for the above samples is displayed. These spectra show the same high energy tailing as Y 3d spectra. Also the Y $3P_{3/2}$ component at 299.1 eV and Y $3P_{1/2}$ component at 311.0 eV are shifted about 0.4 eV to a lower binding energy than the corresponding components for Y_2O_3.

The Y spectra in Y123 superconductor have not been widely reported. However, the high energy tailing and the shift to a lower binding energy observed here has been reported [243-245,247,255].

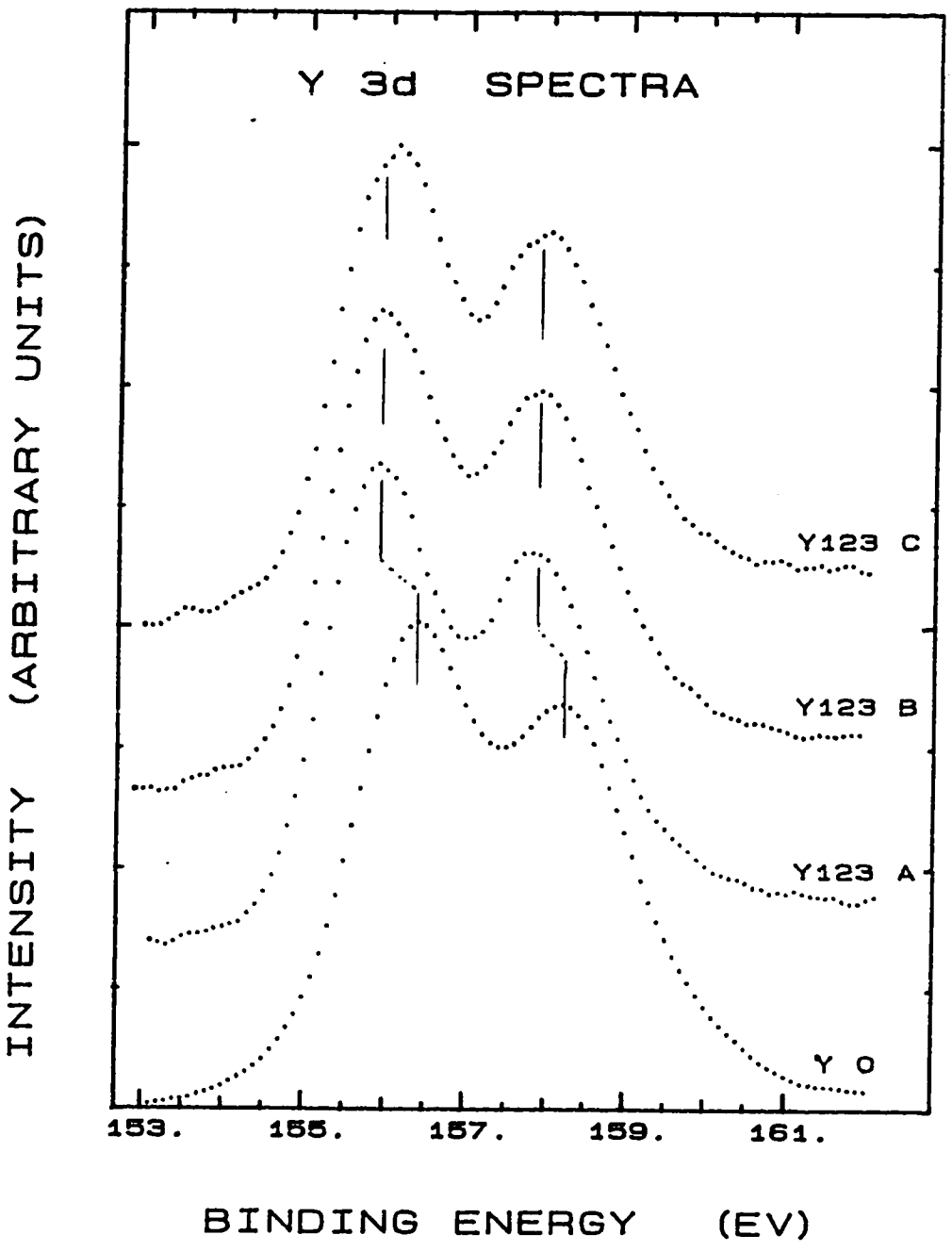

Fig. 4.16 Y 3d XPS spectra of different Y123 samples (A-C same as Fig. 4.6) compared to the spectrum of Y_2O_3 powder.

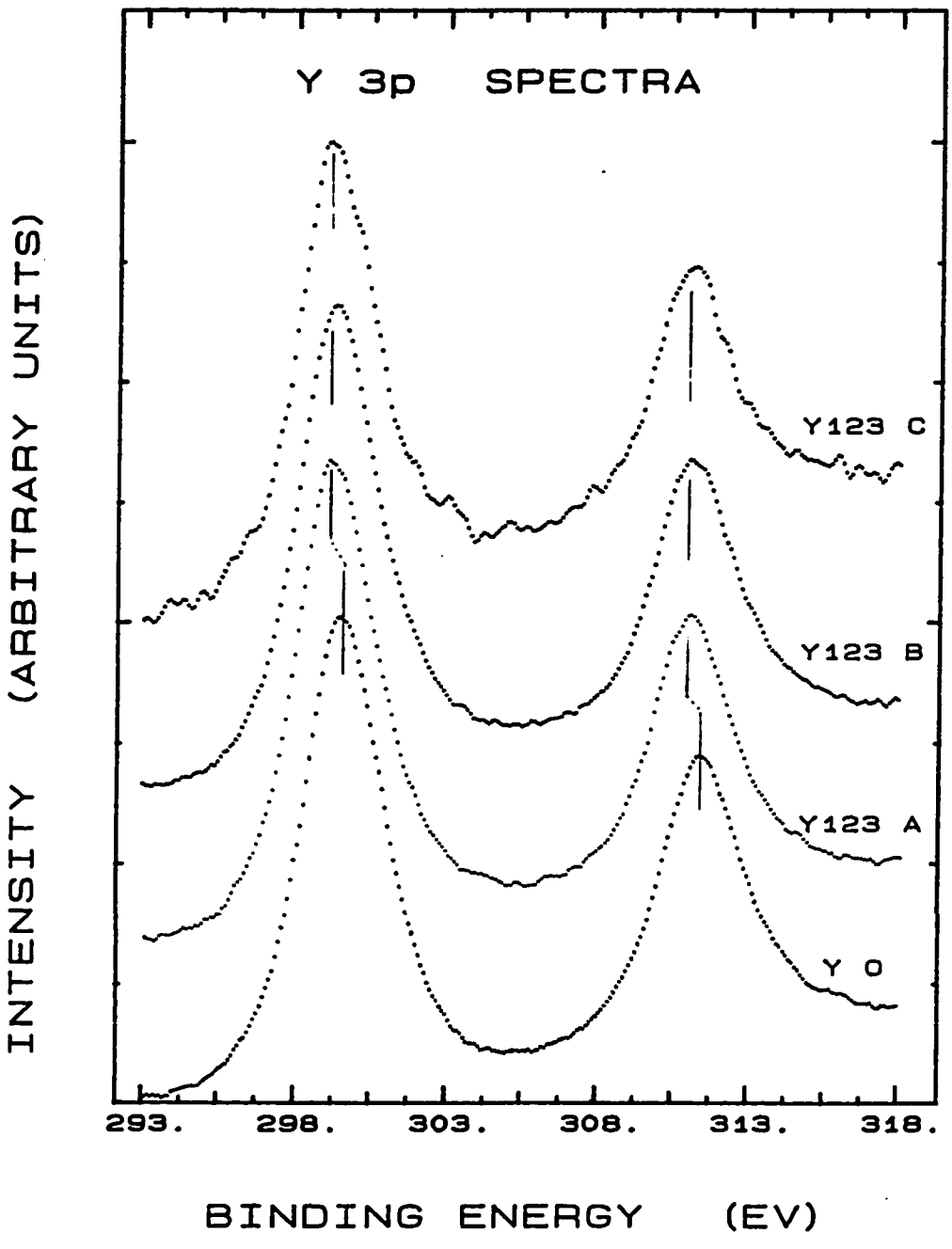

Fig. 4.17 Same as Fig. 4.16 except for Y 3p region.

For the observed Y 3d doublet of Y123 samples (Fig. 4.16), the peak positions at 155.8 eV and 157.7 eV are consistent with the energies reported for metallic Y [272]. Hence, the Y site in the Y123 corresponds to metallic Y coordination without oxygen interaction. This result is in good agreement with the crystal structure of Y123 discussed in Chapter two where the Y plane in the crystal is completely free from oxygen atoms. Furthermore, the high energy tailing and the deviation from theoretical value for the ratio $I\,3d_{5/2}/I\,3d_{3/2}$ observed suggested a second oxidation state of Y. This state is probably caused by the residual unreacted Y_2O_3 oxide from the starting material used to prepare the Y123 samples.

Carbon 1s

The region corresponding to the C 1s was scanned to assess sample cleanliness and chemisorption from the vacuum system.

In spite of efforts to ensure cleanliness of samples through preparation and transportation carbon 1s transition was found during analysis. Fig. 4.18 compares C 1s spectra for different Y123 samples. In addition to C 1s peak at 285 eV which can be attributed either to an adventitious hydrocarbon contaminations or to the presence of carbon in the grain boundaries, another peak at 289.0 eV is observed. The high oxidized carbon peak is likely to reflect a residual carbonate phase. This carbonate originated peak appears in all the samples studied including samples prepared with peroxide. It seems that this carbonate phase was

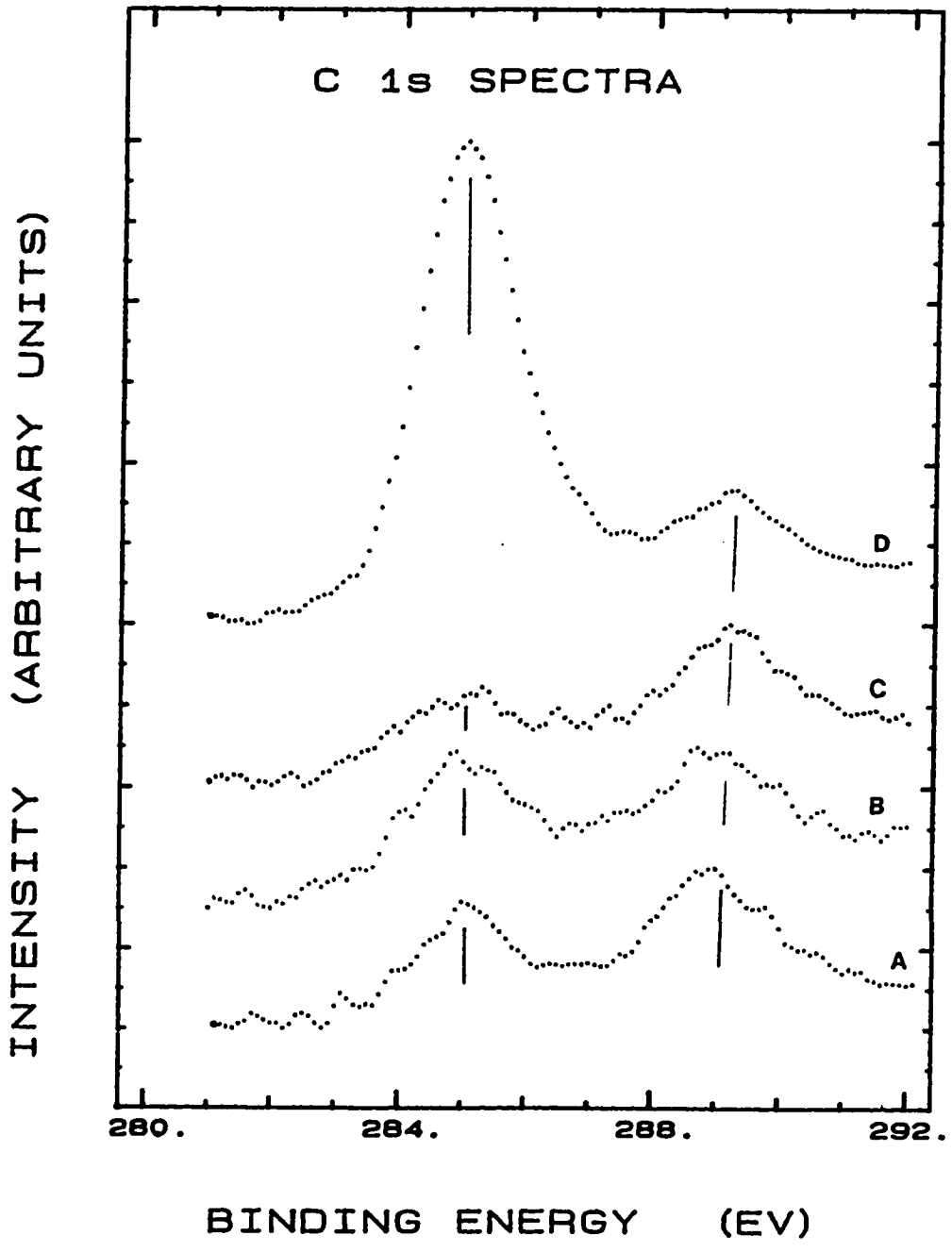

Fig. 4.18 C 1s XPS spectra of different Y123 samples A-C) same as Fig. 4.6 after in situ scraping (clean) D) before in situ scraping (contaminated) sample.

formed during sintering the samples and then stays at grain boundaries. The binding energy of this peak is comparable to that of $BaCO_3$ and the Ba 3d and Ba 4d peak shapes show some dependence on this peak. Hence it can be due to $BaCO_3$ formed at the surface and grain boundaries.

As noticed from the figure the intensity of the two peak is reduced dramatically by scraping but they are still clear. This supports the suggestion that carbon is found at grain boundaries.

4.2.3 X-ray Induced Auger Electron Spectra

The physics of Auger transitions involving valence electrons is admittedly complex, specially in systems like Y123 superconductor where the valence band structure is not completely determined. However, we report here Cu(LVV) and O (KVV) Auger spectra and attempt to relate them with the observed XPS features to estimate the effective Coulomb interaction between valence electrons. The interaction can be probed from the position of the observed Auger lines.

Copper (LVV)

In Fig. 4.19 we show the Cu $L_{2,3}VV$ spectra in the kinetic energy range 880 eV to 950 eV from three different Y123 samples and from both Cu metal and CuO powder. These Auger spectra are obtained by creating the initial state hole with X-rays instead of electrons because X-ray causes far less radiation damage than electrons. Cu (L_3VV) Auger spectra from

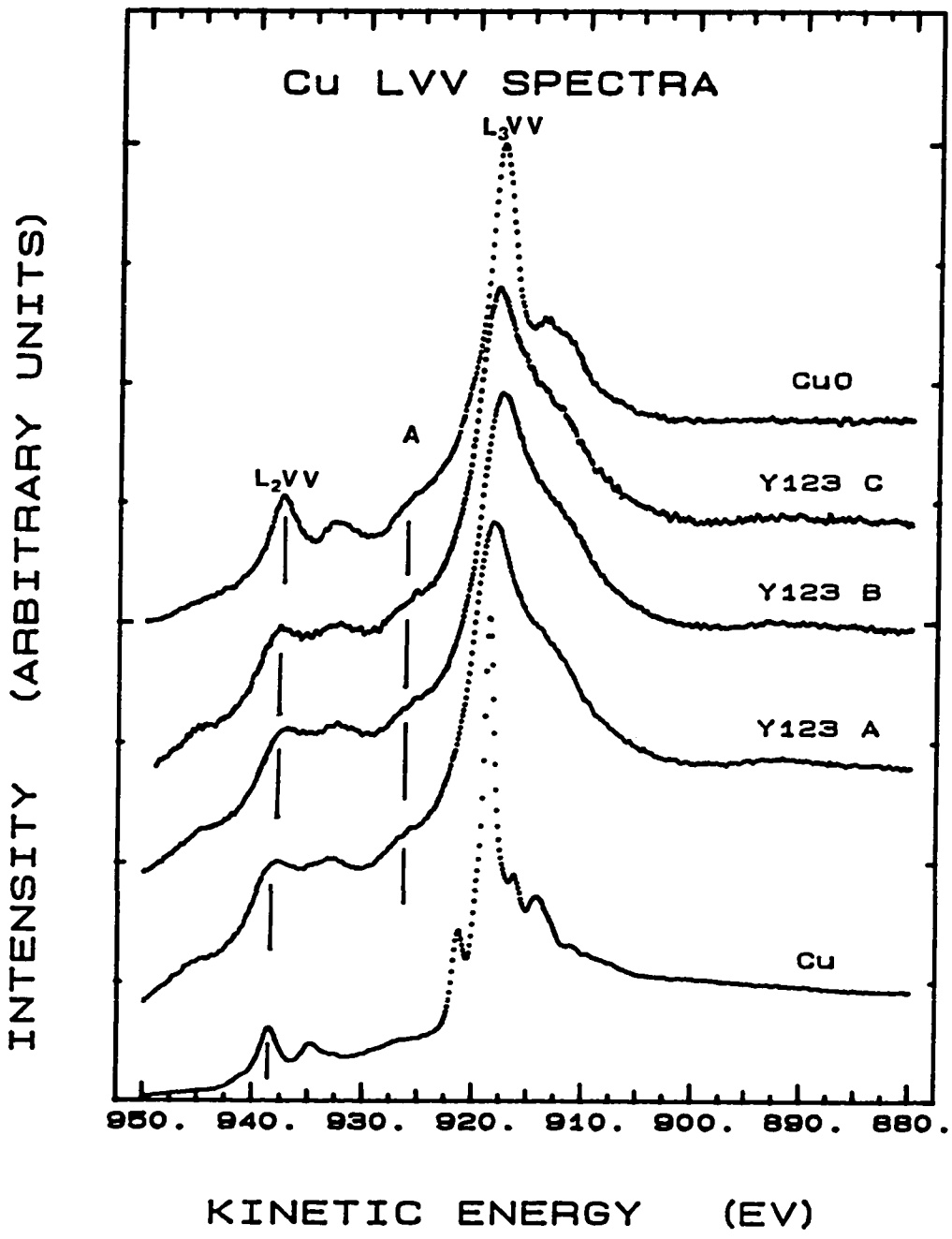

Fig. 4.19 Copper ($L_{2,3}$ VV) Auger spectra of three different Y123 samples (A-C same as in Fig. 4.6), Cu metal and CuO.

Y123 samples is dominated by a broad peak centered at kinetic energy of about 918.2 eV. In this process, a core hole is created in Cu $2p_{3/2}$ state (L_3) which is filled by a valence electron (V) and the energy of this transition is used to emit another valence electron (V). This transition leads to the creation of two holes on the same site. The kinetic energy (E_{kin}) of the electron must be related to the Coulomb interaction between two valence electrons. The position of the Cu (L_3VV) Auger peak is given by

$$E_{kin} = E_B(L_3) - 2E_B(3d) - U^{\wedge}_{eff}(d\text{-}d)$$

i.e. the effective Coulomb repulsion $U^{\wedge}_{eff}$ is

$$U^{\wedge}_{eff}(d\text{-}d) = E_B(L_3) - 2E_B(3d) - E_{kin}$$

where $E_B(L_3)$ and $E_B(3d)$ are the binding energies for the Cu $2p_{3/2}$ core electrons and Cu 3d valence electrons respectively. Theoretical treatments of Cini [264] and Sawatzky [265] indicate that $U^{\wedge}_{eff}$ approaches the effective Coulomb interaction U_{dd} asymptotically in the limit of large U. An estimate can be derived from the peak in the L_3VV Auger spectra since $E_B(L_3)$ and $E_B(3d)$ can be derived from XPS spectra. For the studied Y123 samples estimated U_{dd} is about 5 eV.

The observed Cu (L_3VV) lineshapes reveal a principle peak around 918 eV and a satellite at around 914 eV. According to Laan et al [230] and Larson et al [266] as well as our previous discussion of Cu 2p

line (sec. 4.2.2) the main L_3VV line at kinetic energy 918.2 in Y123 originates from the $2\underline{p}3d^{10}\underline{L}$ state and ends in a $3d^8\underline{L}$ final state. The satellite at the low kinetic energy side originates in the $2\underline{p}3d^9$ initial state and ends with the $3d^7$ final state. The features seen in Fig. 4.19 between the L_3 and L_2 Auger transitions marked A are most likely due to final states $3d^9\underline{L}^2$ which can be reached because of covalent mixing with the states $3d^8\underline{L}$. This is similar to the peak seen in copper dihalides as discussed by Laan et al [230]. The L_2VV Auger transitions for Y123 show a main peak at about 938 eV kinetic energy and a satellite around 933.5 eV kinetic energy.

From Fig. 4.19 we can notice two main differences between Cu (L_3VV) spectra of Y 123 and those of Cu and CuO: (a) the features are less sharp and (b) there is an extra intensity in the satellite at 914 eV.

Laan et al [230] have discussed the same features for Cu dihalides. They attribute the smoothing of the spectra to crystal-field splitting. Another source of broadening is formed by the finite life time due to coupling of the d^8 states to the $d^9\underline{L}$ continuum. Furthermore, Lann et al attributed the extra intensity in the satellite to the d^7 final states originating from the unscreened $2\underline{p}3d^9$ state. These extra lines coincide almost completely with the positions of Auger transitions produced by L_2L_3V Koster-Kronig process which also end at $3d^7-$ like states. Through this process the L_3VV line "borrows" intensity from the L_2VV line [195].

Oxygen (KVV)

In Fig. 4.20 we display O (KVV) spectra of different Y123 samples scrapped in situ. The O (KVV) transition shows a broad feature with a central component around 514.4 eV and a shoulder at 511 eV kinetic energies. The spectra result from the creation of an O 1s core hole and is dominant by the final state in which two valence band holes have predominantly O 2p character. In accordance with Valzarotti, et al [267], the peak at 514.4 eV can be assigned to O^{1-} ion while the shoulder at lower kinetic energy corresponds to the final state configuration $2S^2 2p^4$ of the O^{2-} ion. Nevertheless, other explanations for the peak at 514.4 are possible [268].

By analogy with the Cu (LVV) spectra we may write

$$U^{\wedge}_{eff} = E_B(1s) - E_{kin}(KVV) - 2E_B(2p)$$

Hence, from the binding energies of O 1s peaks and from the position of O 2p valence band component we estimate a value of $U^{\wedge}_{eff} \approx 8.4$ eV. This value is much higher than is generally assumed [24]. A discussion of this point is given in Ref. 24.

4.2.4 Surface Effects

As discussed before, (Ch. 3), it is evident that the cleanliness of the samples surface plays a crucial role in the photoemission results. Thus,

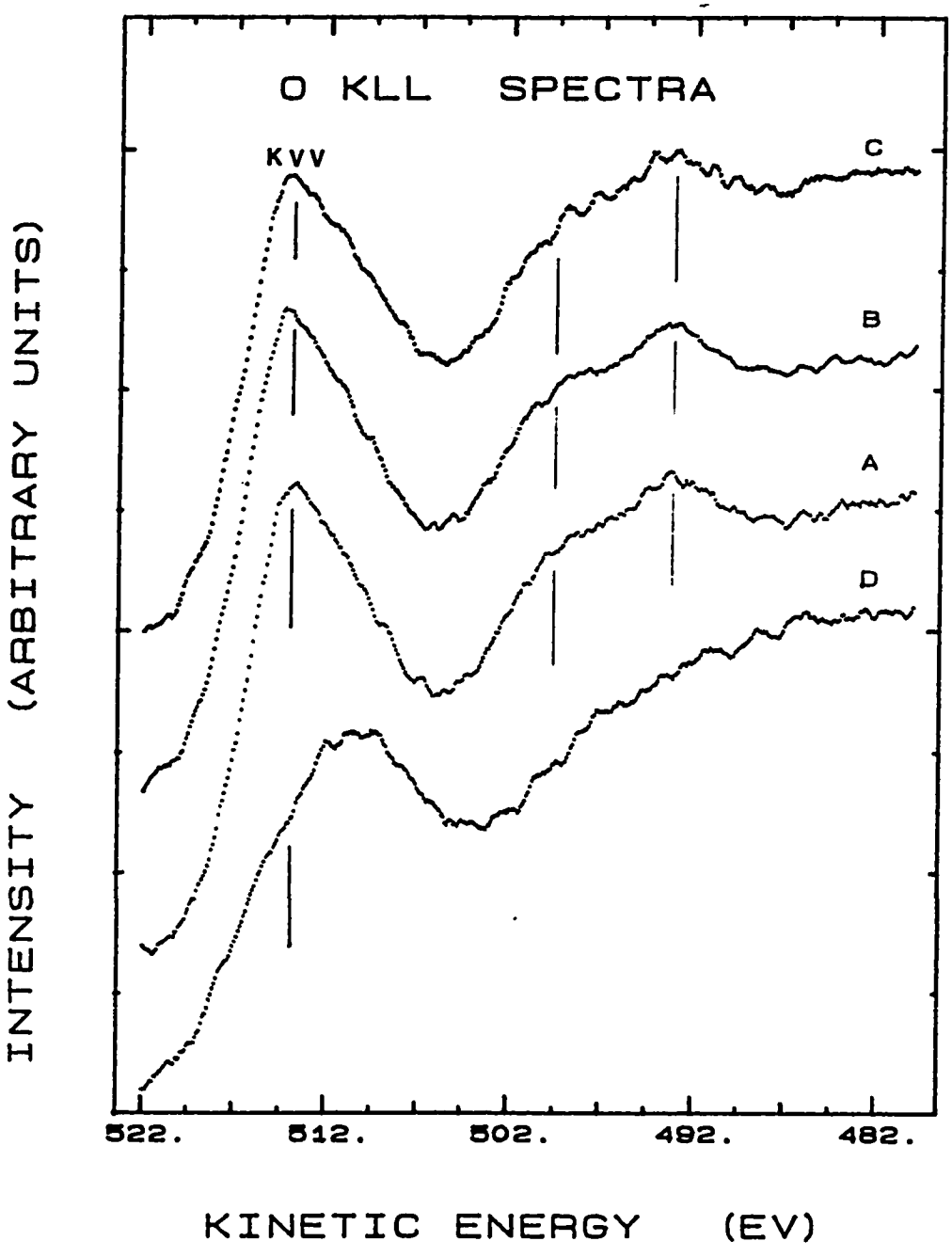

Fig. 4.20 Oxygen K LL Auger spectra of different Y123 samples scraped in situ, (A-C as in Fig. 4.6), with the spectra taken from dirty sample.

special attention must be paid to surface cleaning for the studied samples. Moreover, careful examination of the surface cleanliness is imperative prior to photoemission experiments.

For Y123 superconductor, the most trustworthy monitor of the surface condition is probably the O 1s and the Ba (3d. 4d, 2p) XPS peaks. In Fig. 4.21 to Fig. 4.26, we compare spectra obtained from unscraped surfaces (contaminated) with those obtained from scraped (clean) surfaces.

For contaminated surface, O 1s spectrum (Fig. 4.21) is dominated by the high binding energy peak at 531.4 eV which is attributed to contamination carbonate or hydroxide phases formed at the surface or at the grain boundaries. Adsorbed CO and CO_2 can also contribute to the intensity of this peak. A feature related to this peak appears in the Ba atom spectra. As seen in Fig. 4.22, the carbonate component around 779.7 eV is higher than the superconductor component in the contaminated surface spectrum.

In the C 1s region large amounts of carbon from both adventitious and carbonate species appears in the photoemission spectrum of the unscraped surface compared to that of the clean surface, Fig. 4.23. Also, Y 3d line, Fig. 4.24, shows a smeared unresolved structure indicating the presence of more than one oxidized Y state at the spectrum. The additional status are most likely resulting from Y_2O_3 and $Y(OH)_3$ present at the sample surface. No major difference is observed in Cu 2p spectra (Fig. 4.25) which indicates the stability of Cu states in this high T_c

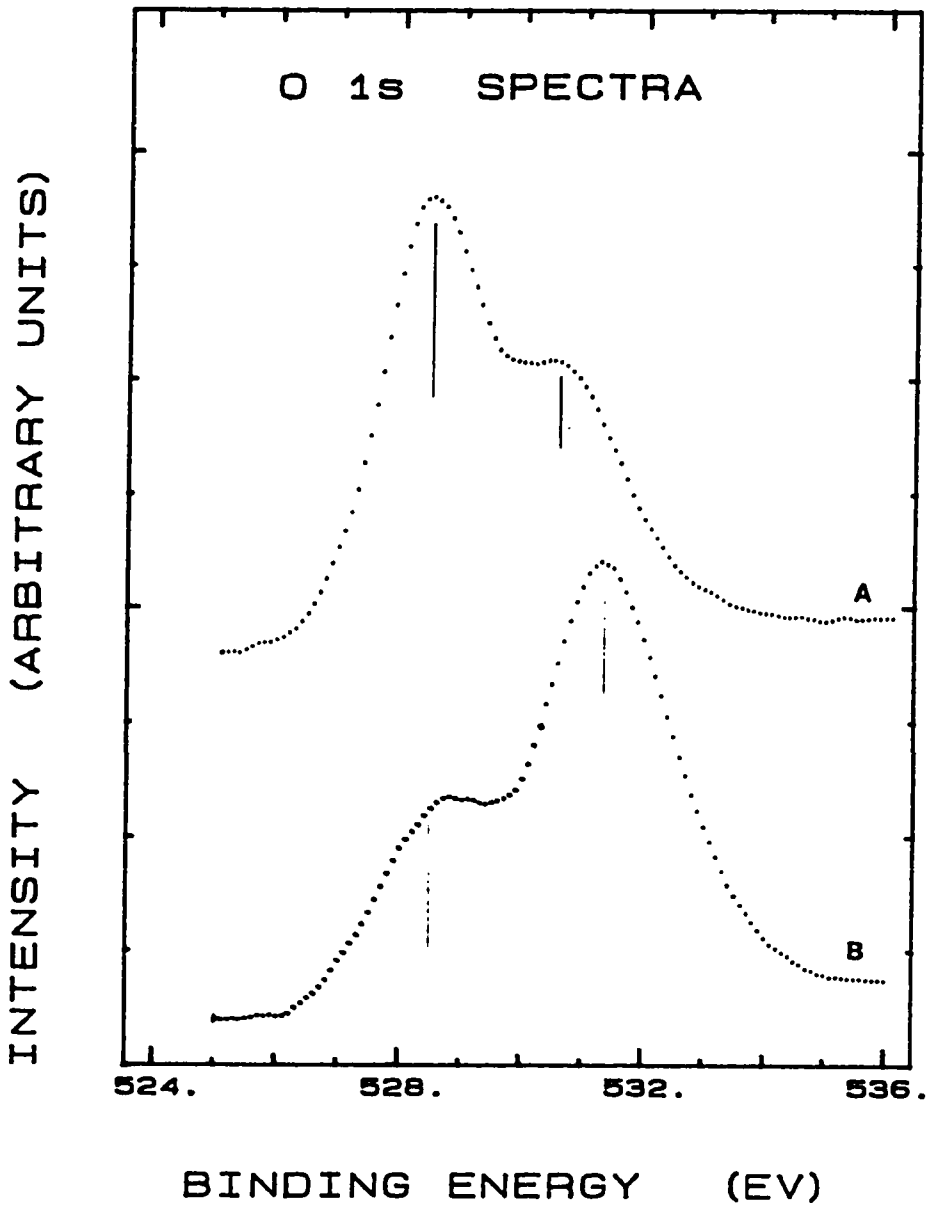

Fig. 4.21 O 1s XPS spectra of Y123 samples A) After scraping in situ (clean), and B) As introduced surface (contaminated).

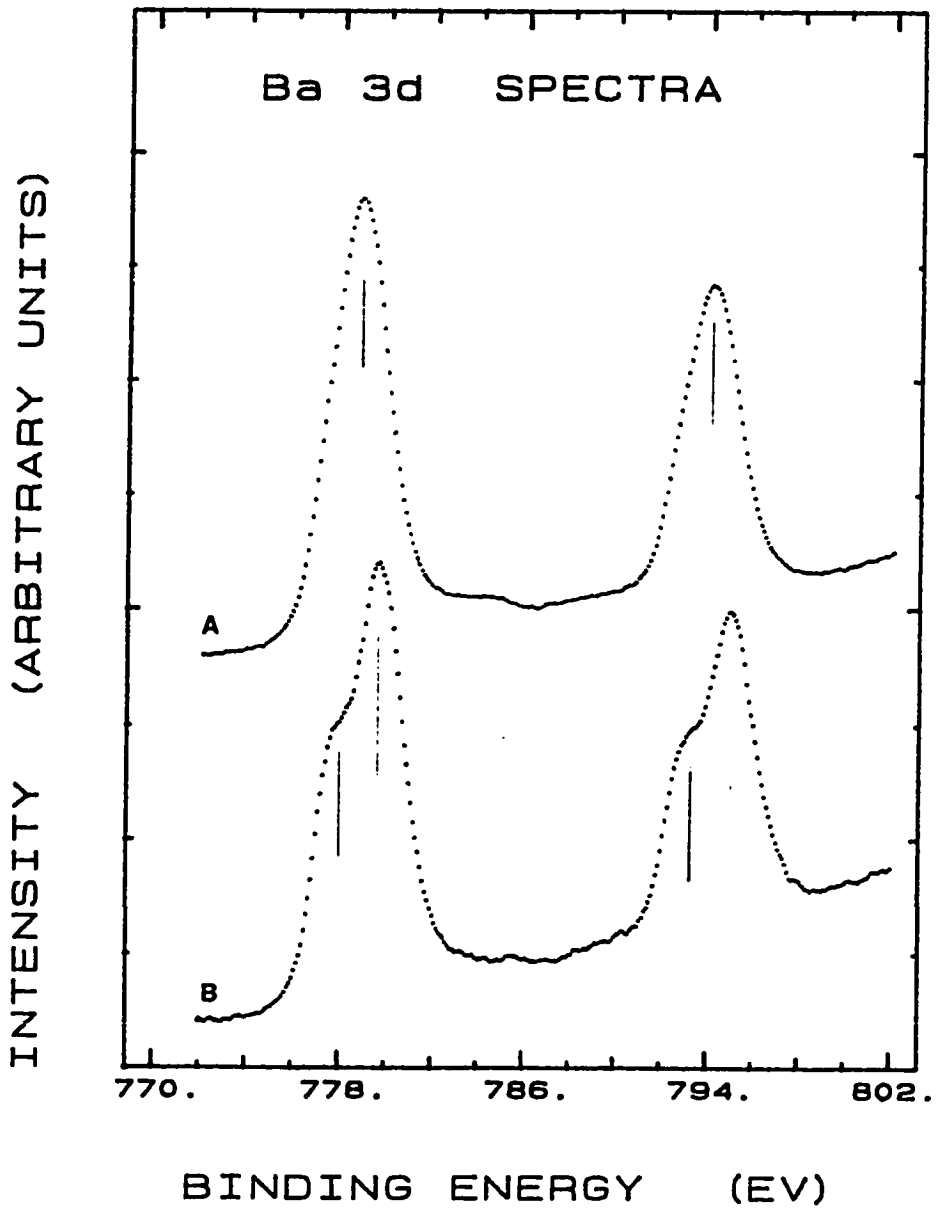

Fig. 4.22 Same as Fig. 4.21 except for Ba 3d region.

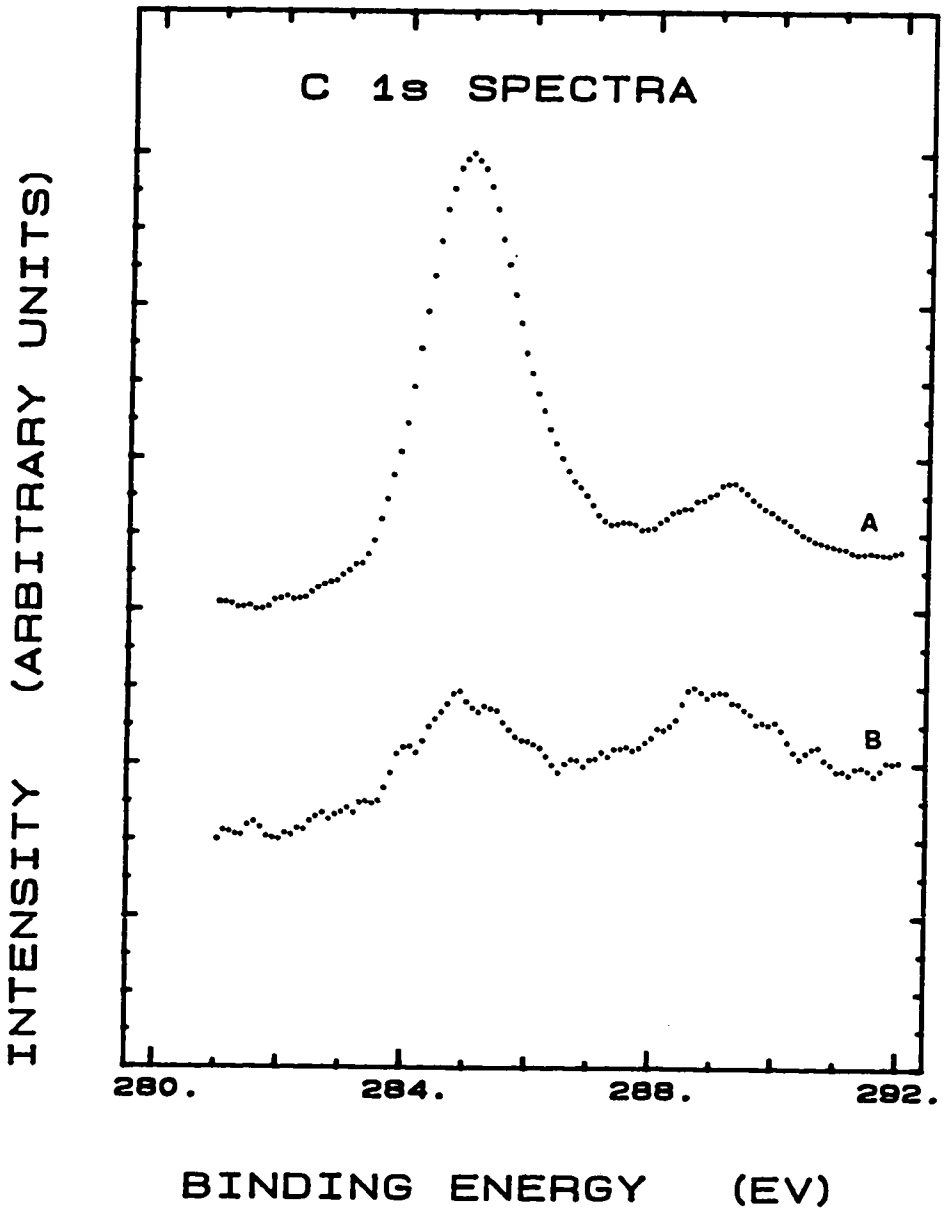

Fig. 4.23 Same as Fig. 4.21 except for C 1s region.

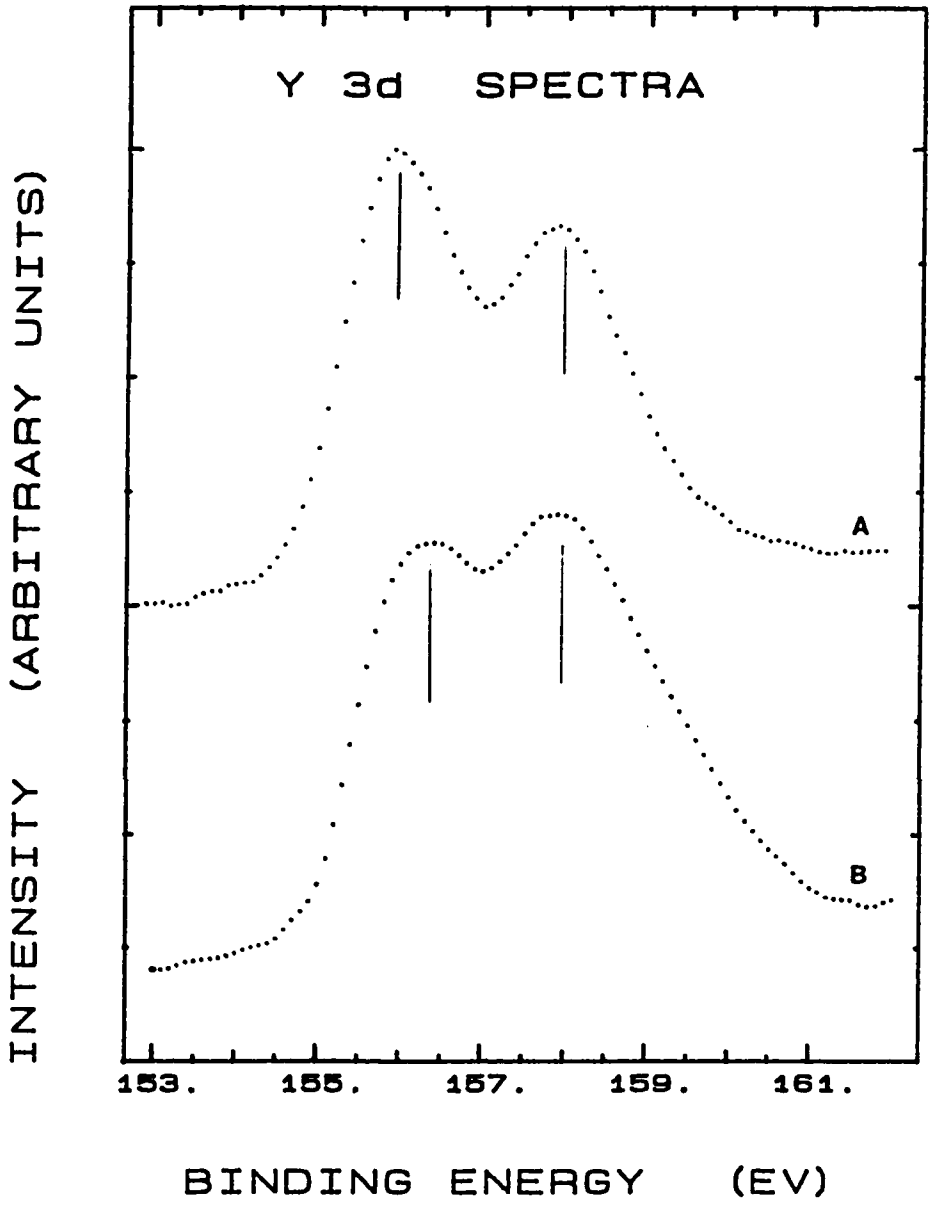

Fig. 4.24 Same as Fig. 4.21 except for Y 3d region.

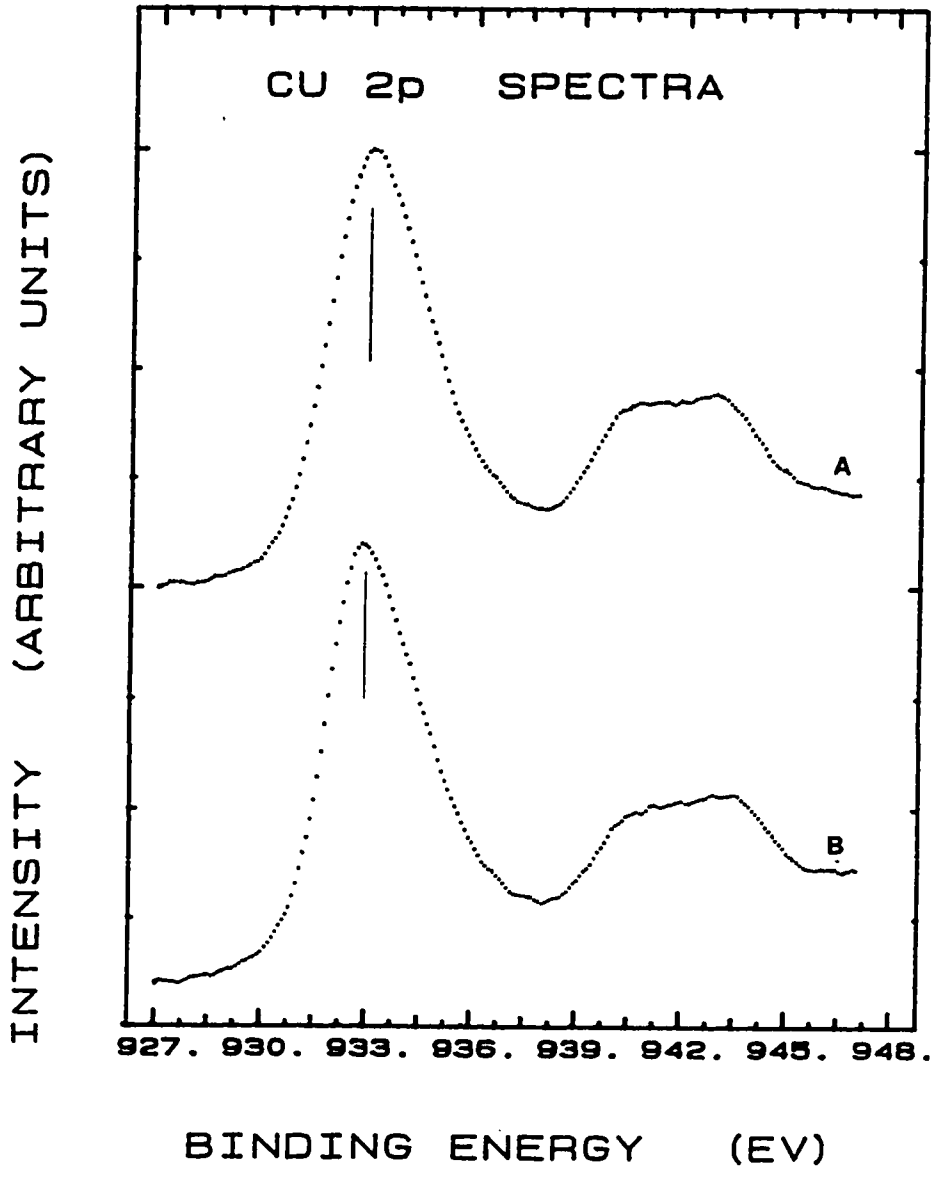

Fig. 4.25 Same as Fig. 4.21 except for Cu 2p region.

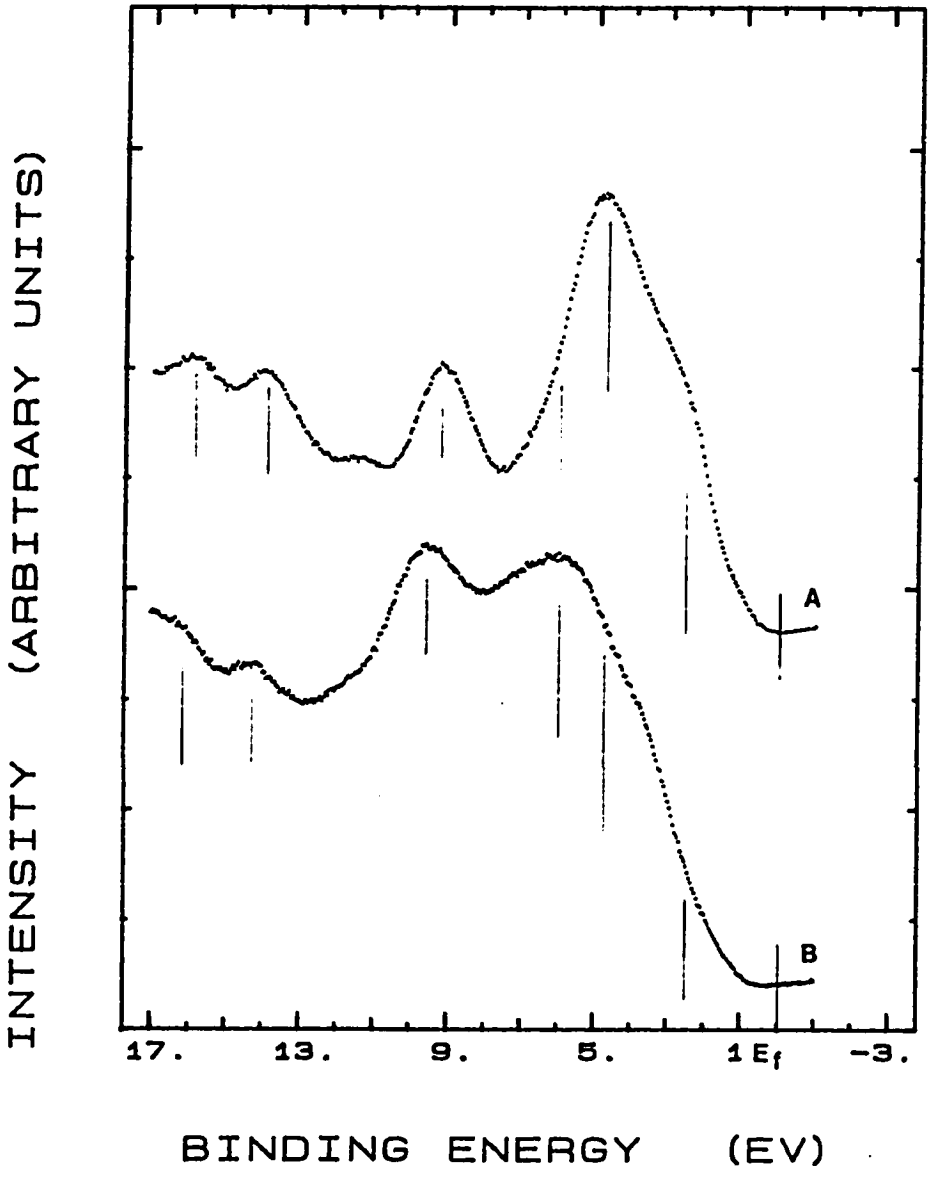

Fig. 4.26 He -II valence band spectra of Y123 sample, A and B same as Fig 4.21.

superconductor. However dramatic changes are found in the valence band spectra obtained by He II radiation (Fig. 4.26). In the contaminated surface spectrum the 9.4 eV peak which has some C 2p originated component is dominant, the intensity of the shoulder at 2.8 eV due to O 2p states decreased, and the shoulder at 6.3 eV which is mainly due to contamination phase grows too much. All these changes result generally from the presence of carbon compounds and other contaminations at the surface and can be almost totally removed by scraping the surface.

From the above results it is clear that the surfaces of the prepared Y123 samples always show a strong contamination level just as prepared, hence they need a careful cleaning in order to obtain a representative surface for the bulk material. We find that mechanical scrapping of the surface produces a good representative surface with a very small amount of contamination which is proposed to be present at the grain boundaries in the bulk of the samples. Moreover scraping does not alter the composition of the surface.

Another important point is the stability of the surface after cleaning. As discussed in Sec. 3.5, we found that scrapped surfaces stay clean and no changes are observed during the experiment period. In order to check for any change in the surface state during experiment time a short run for only C 1s and O 1s was performed before and after each experimental study. No differences were observed between the spectra obtained in these two short runs. After a long time in UHV some deviation from the clean spectra starts appearing.

In Figures 4.27 to 4.30 we compare valence band, O 1s, C 1s and Ba 3d spectra obtained from Y123 sample surface immediately after scrapping and one month in UHV later. Aging in situ of Y123 samples results in the growth of the O 1s shoulder (Fig. 4.27) and C 1s line of 285 eV (Fig. 4.28) because of chemisorption of residual H_2O, CO and CO_2 in the vacuum system. Similarly, the high binding energy component of Ba $3d_{5/2}$ line (Fig. 4.29) shows an increase indicating the formation of Ba contamination phases which are generally Ba CO_3 and $Ba(OH)_2$.

With respect to the He-II valence band (Fig. 4.30), the shoulder at 2.6 eV intensity is reduced because of oxygen depletion from the surface layer. Also, the adsorption of residual contaminants in the system causes the growth of the shoulder at 6.3 eV, which is mainly due to contamination phase, and the 9.4 eV peak. A representative clean surface can be regenerated by scrapping in situ, which indicates that oxygen is generally desorbed from the surface layer only which also accumulates contamination from the surrounding media after prolonged exposure to UHV.

4.3 Photoemission Case Studies

The existence of high T_c superconductivity in a wide range of compounds is now well established [25]. However, there are many obstacles in the road of the practice use of these materials, mainly because of their limited chemical stability. The Y123 compounds readily react with the

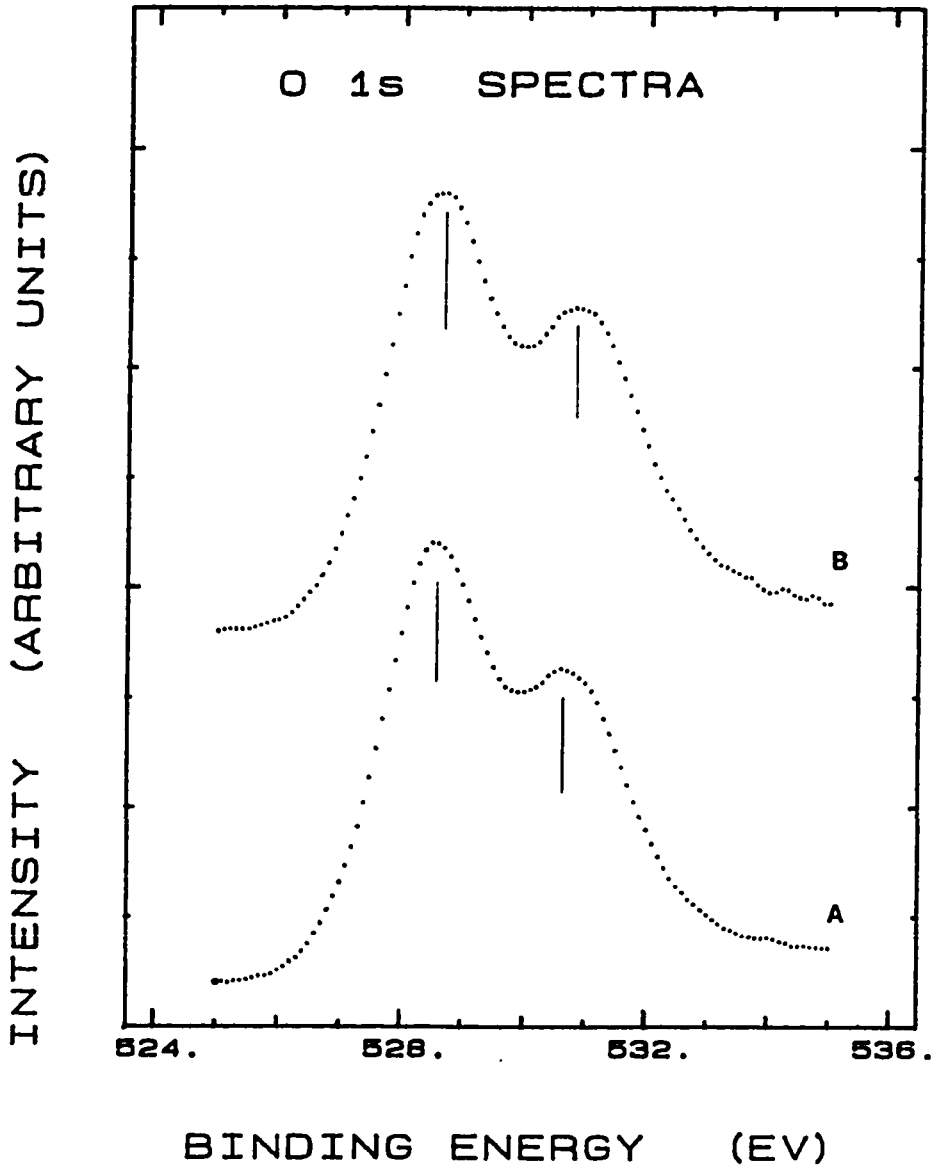

Fig. 4.27 O 1s XPS spectra of Y123 samples A) After scraping in situ (clean), and B) After one month exposure to UHV.

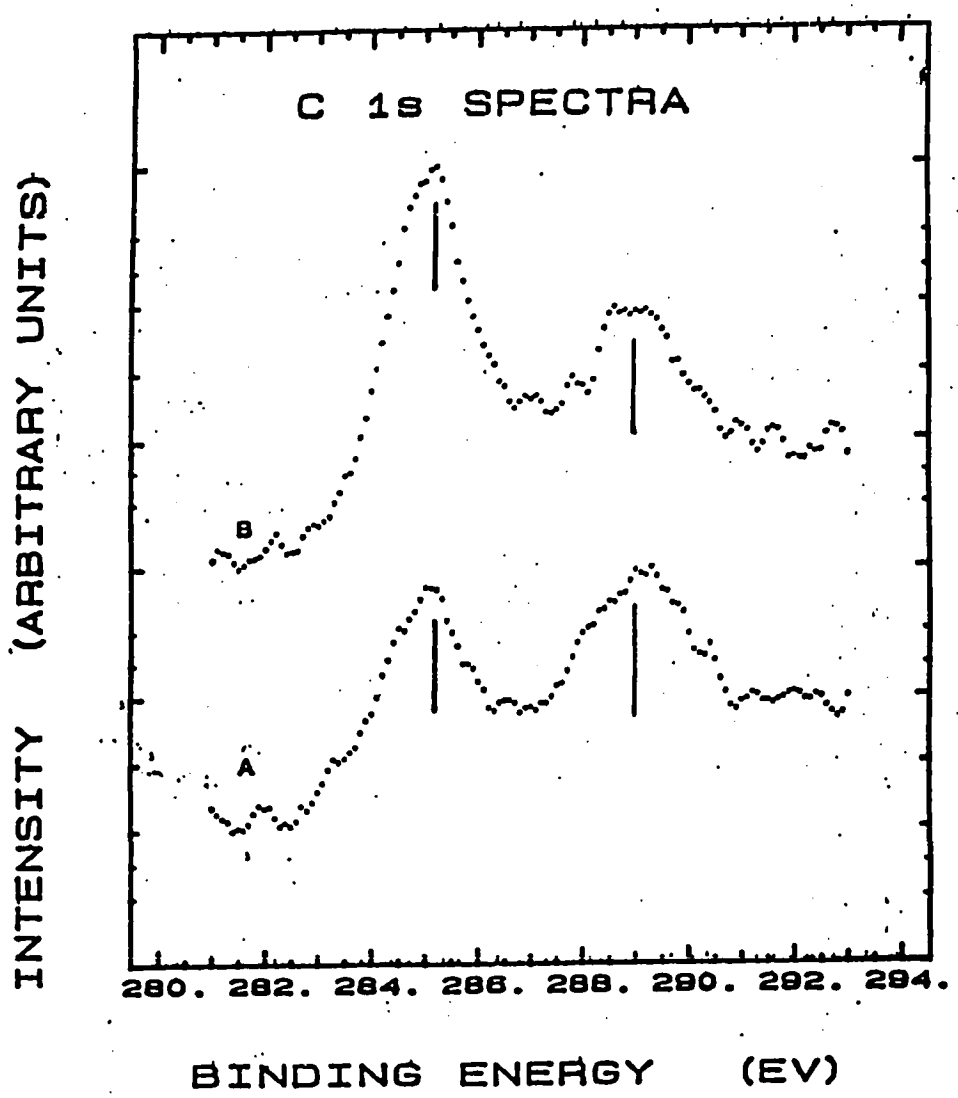

Fig. 4.28 Same as Fig. 4.27 but for C 1s line

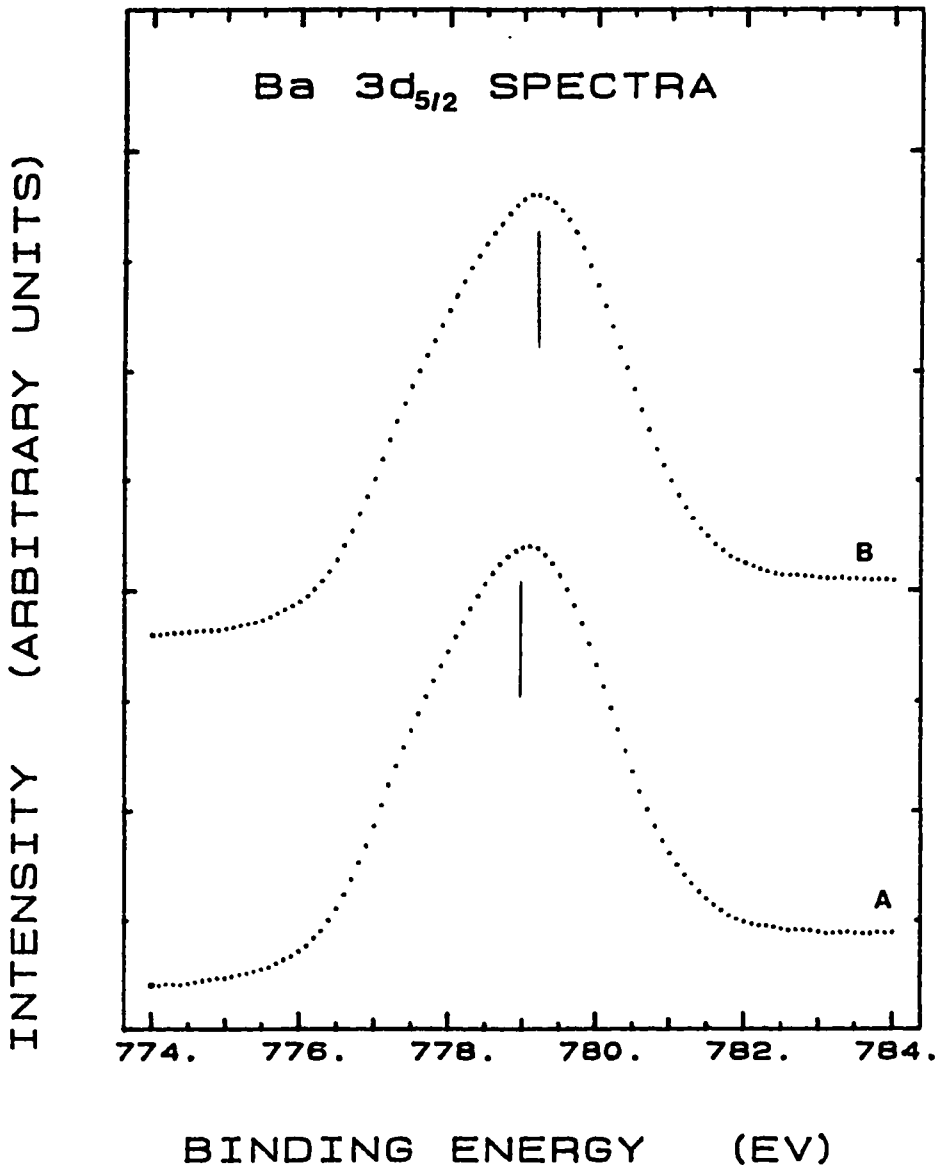

Fig. 4.29 Same as Fig. 4.27 but for Ba $3d_{5/2}$ line.

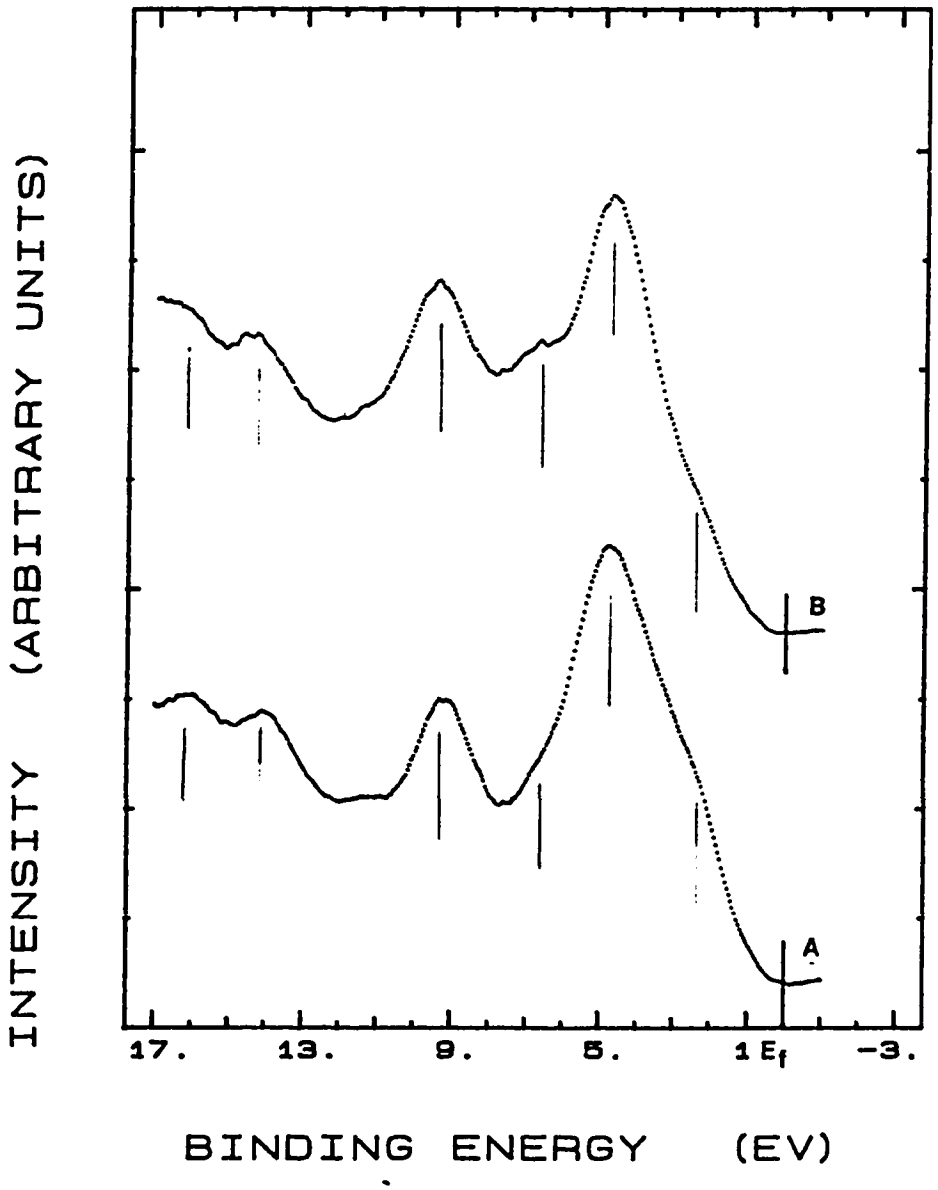

Fig. 4.30 He -II valence band spectra of Y123 sample, A and B same as Fig 4.27.

ambient atmosphere at typical ambient temperature. Both water and carbon dioxide participate in the degradation through the formation of hydroxides and carbonates. Also, the chemical stability is limited because of oxygen loss from the materials under vacuum.

In the following sections we will discuss the effect of heat treatment in UHV and the effect of H_2O and O_2 exposure and Y123 samples by the aid of photoemission spectra obtained from these samples.

4.3.1 Effect of Heat Treatment in UHV

Heat treatment procedure was carried out in the high pressure cell directly mounted to the fast-entry-airlock chamber. The cell was heated to the required temperature and was kept at this temperature for about 1 hour prior to the introduction of the sample to make sure that it will not outgas during annealing the sample. The Y123 samples were scrapped in situ with a diamond file and studied before the treatment, then introduced to the cell for annealing. During annealing the pressure in the chamber increased from $\approx 10^{-8}$ torr to $\approx 10^{-6} - 10^{-5}$ torr, indicating the release of oxygen from the samples.

All core level lines and the valence band were monitored during the course of heat treatment. Oxygen, barium, valence band and to a lesser extent copper showed important variations, whereas Y did not. Figures 4.31 through 4.33 display the core level spectra after different

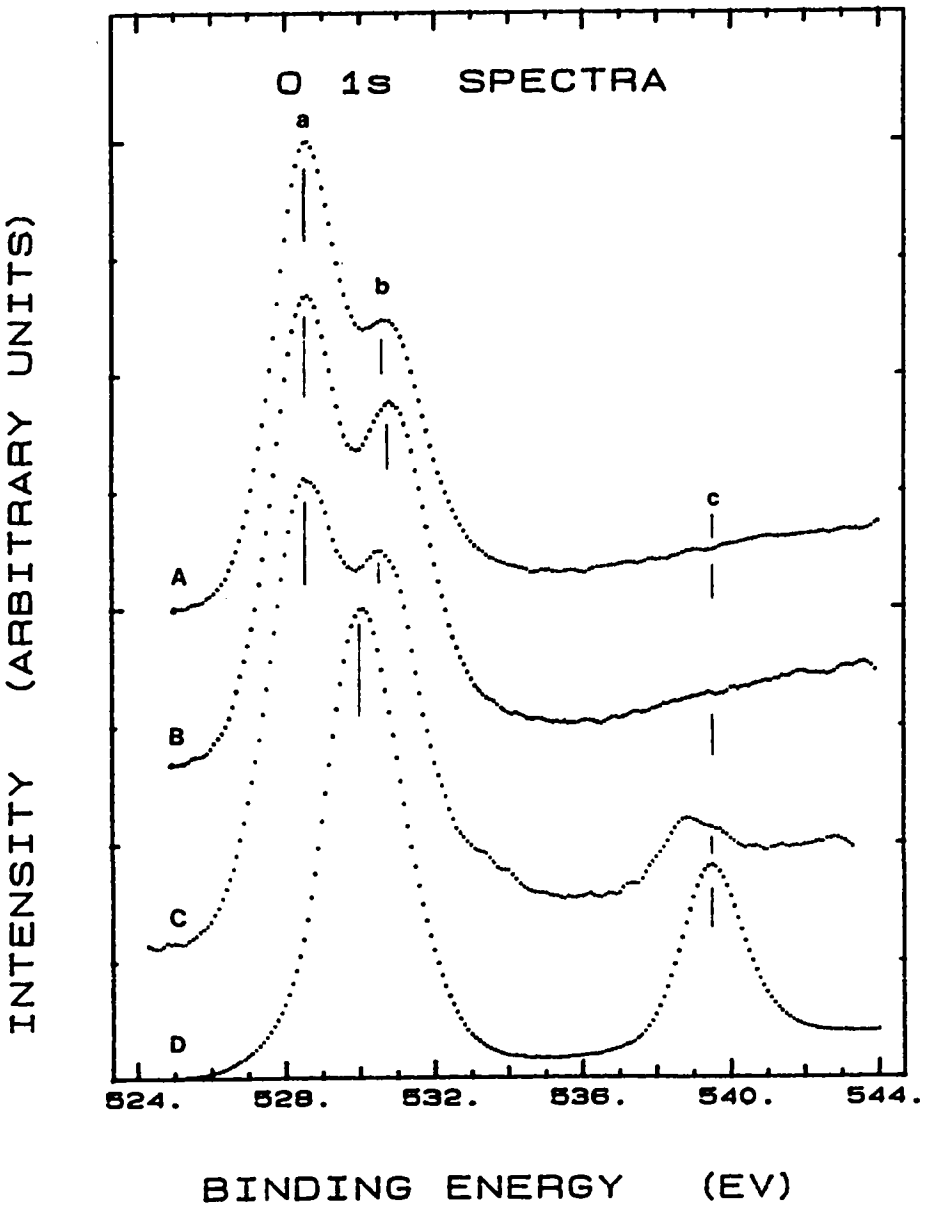

Fig. 4.31 O 1s XPS line for Y123 sample A) Scraped in situ and after different heat treatments in UHV for 15 min.; B) Treated at 200 °C, C) Treated at 400 °C, and D) Treated at 600 °C.

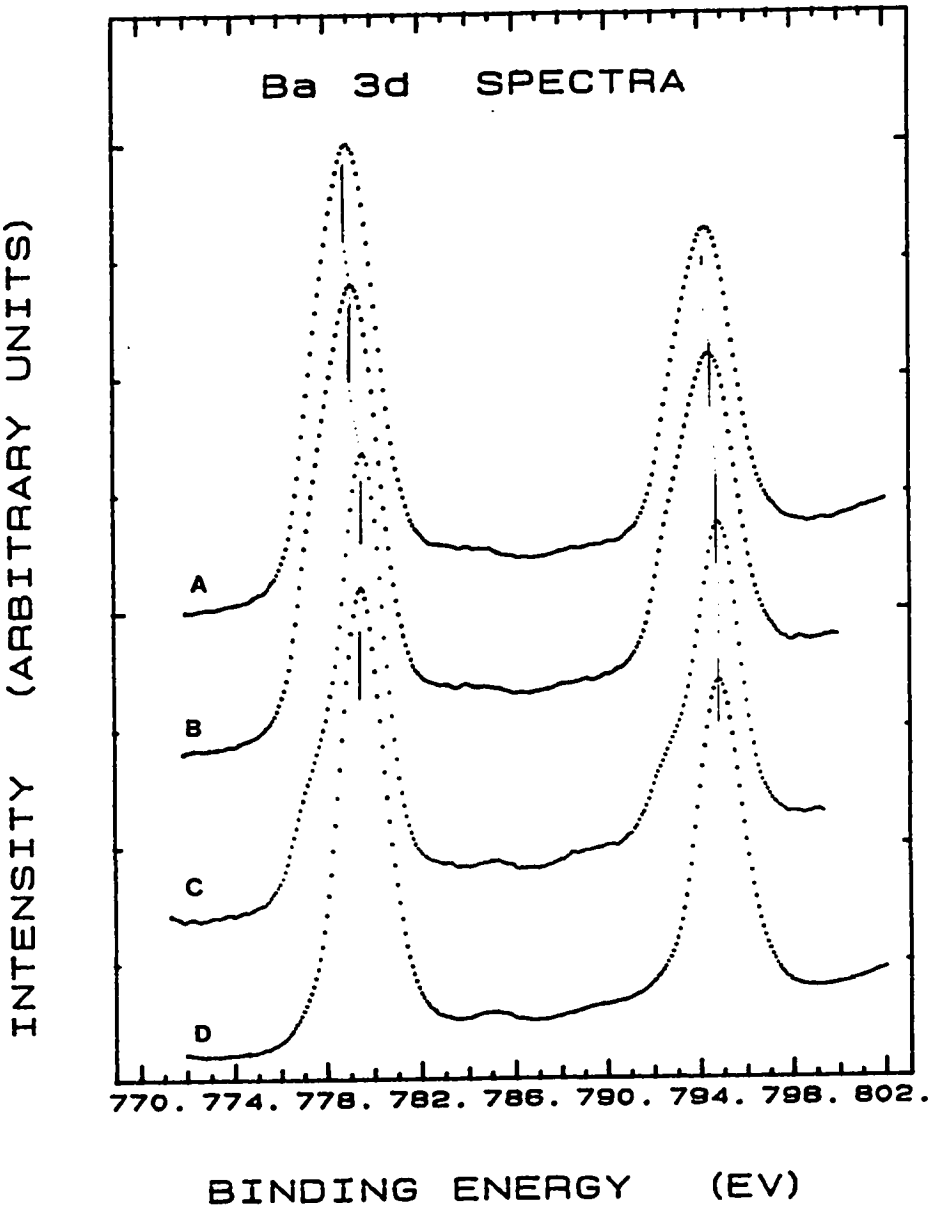

Fig. 4.32 Same as Fig. 4.31 except for Ba 3d XPS line.

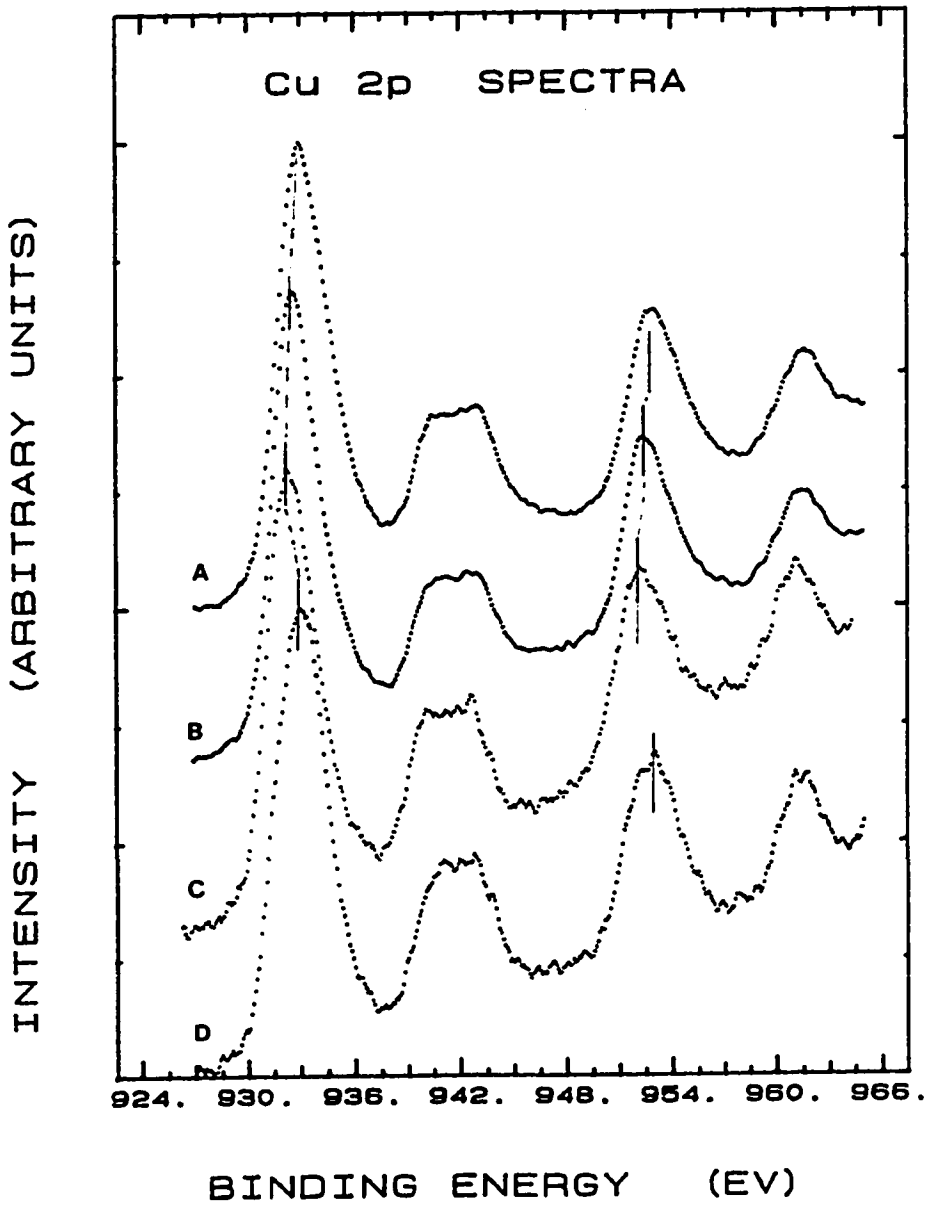

Fig. 4.33 Same as Fig. 4.31 except for Cu 2p XPS line.

stages of treatment while Fig. 4.34 displays the valence band spectra. Curves labeled (A) represent the sample surface after scrapping in situ. The origins of these peak have been discussed in the previous sections. The sample was then heated to 200 °C for 15 minutes. The spectra after this heating are displayed by curves (B). The sample was next heated to 400 °C for 15 minutes after scrapping the surface. Curves (C) show the effect of this heating. Finally, the sample was heated to 600 °C for 15 minutes after another scrape of the surface. The results of this stage are presented by curves (D).

Sample charging was observed when the sample was heated at 400°C and 600°C. This charging resulted from a loss of conductivity at the surface of the sample and caused line shift. The line position was corrected by lining the Y 3p line which shows the least dependence of temperature. This method of energy scale correction has been used in ref. 265.

During the different stages of heat treatment O 1s spectra Fig. 4.31 indicates the loss of oxygen from the sample surface. The low binding energy peak (a) at 528.5 eV and the high binding energy peak (b) at 530.6 intensity ratio I_a/I_b decreases with increasing the annealing temperature. Also, the intensity of both peak decreases till they finally become one peak at 530 eV. Moreover a new peak appears at high temperatures of treatment around 539.2 eV. At the same time Ba $3d_{5/2}$ peak (Fig. 4.32), shows a clear narrowing where the low binding energy shoulder lost its

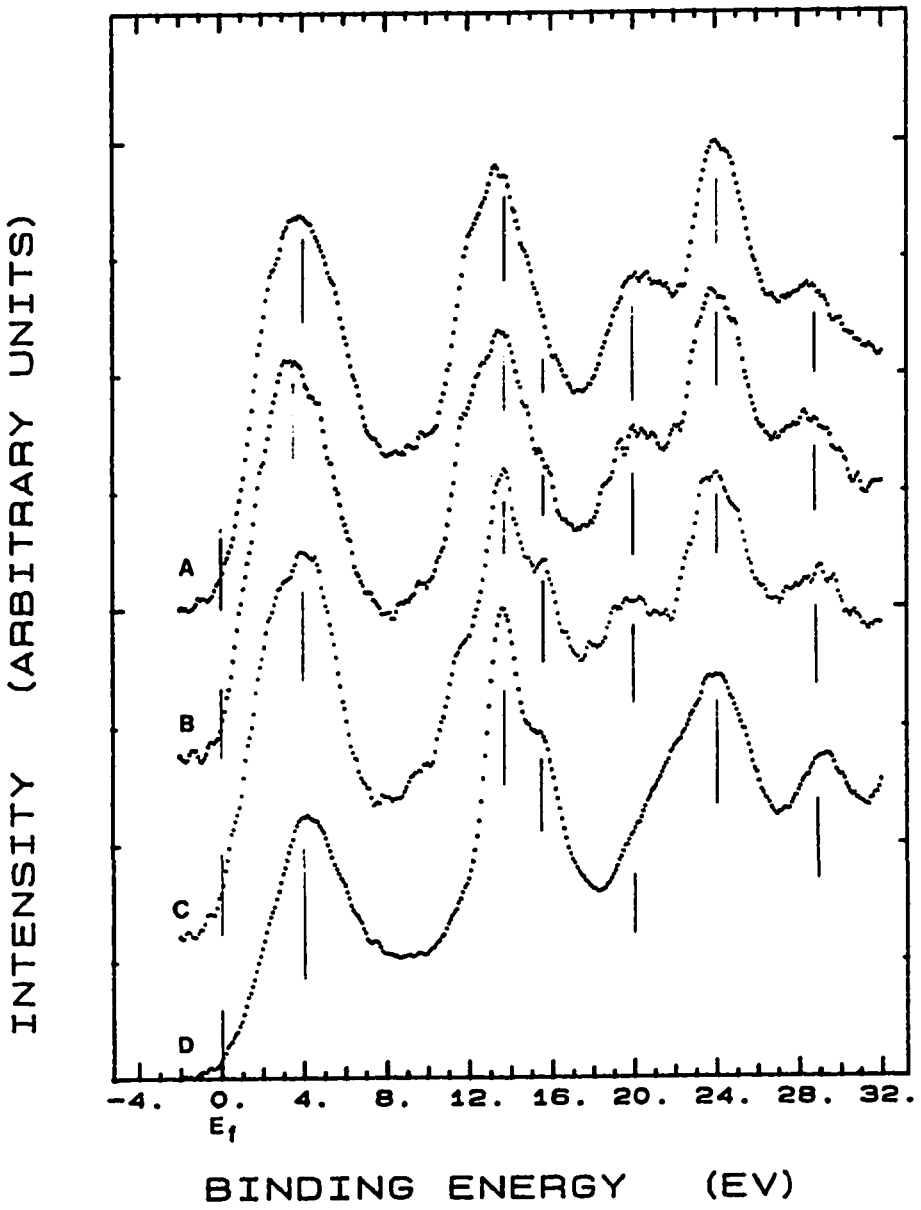

Fig. 4.34 Same as Fig. 4.31 except for XPS valence band and shallow core levels.

intensity relative to the central peak at 779.0 eV. Similarly, there was a decrease in the FWHM of Cu $2p_{3/2}$ peak (Fig. 4.33). The center of this peak is shifted to a lower binding energies and I_s/I_m decreases, when treated at 200°C and 400°C. However the detected amount of Cu was drastically reduced at 600°C and the spectra shape becomes similar to the original clean surface.

The decrease noticed in I_a/I_b for O 1s spectra is due to the diffusion of oxygen containing contaminants from the bulk to the surface layer during heating. At higher temperature these contaminants are almost completely removed from the surface as what we observed from C 1s line. We have concluded before that peak (b) is attributed to oxygen hole (O^{1-}) and with the loss of oxygen from the sample the number of O 2p holes decreases leading to the loss of peak b intensity, in consistence with what we get here. The new peak around 539.2 eV found in O 1s is proposed to be due to oxygen molecules released from the bulk and accumulated at the surface or trapped in the porosities of the sample. The observed changes in Cu 2p are consistent with the reduction of Cu valency and the decrease of O 2p holes due to oxygen loss. Also the observed behavior in Ba atom spectra supports the conclusion reached before when explaining the Ba spectra, that the high energy contribution in the Ba spectra is due to Ba^{2+} coordinated with O^{2-} vacancies. The obtained conclusion from core level spectra is supported by the changes observed in the valence band and shallow core levels spectra, Fig. 4.34 . The intensity near the Fermi level and the intensity of the valence band is largely

reduced by heat treatment due to oxygen loss and the reduction of Cu amount at the surface. Also, Ba 5p peak is narrowed and shows a better resolution, and finally O 2s intensity is reduced and a new peak (not shown) appears in spectra C, D with approximately the same shift as the one observed in O 1s spectra which is similarly attributed to O 2s from molecular oxygen.

4.3.2 Water Exposure Effect

Water exposure took place in the high pressure cell. Freshly distilled H_2O was placed in a flask and the flask was connected to the gas inlet tube of the high pressure cell through a fine control value. Before exposure, H_2O was vigorously boiled to remove any dissolved gasses such as O_2 and CO_2. While boiling H_2O , the resulting steam with dissolved gasses was pumped out using oil free pump and H_2O was kept in the flask at low pressure.

For exposure, freshly scrapped sample was moved from the analysis chamber to the fast-entry-air-lock chamber through the preparation chamber. Thereafter the sample was inserted in the high pressure cell and the cell was tightly closed while it is at a very low pressure (8×10^{-7} mbar). The valve between the cell and water flask was then opened. At such low pressures, water evaporation rate is very high and the high pressure cell was filled with water vapor. Following exposure, the high pressure cell was pumped again and the sample was

moved from the high pressure cell to the fast-entry-air-lock chamber. At the fast-entry chamber the sample was left for a period to outgas; hence it was moved to the preparation chamber and finally to analysis chamber. The sample continued outgassing in the analysis chamber but with very low rates.

There was a number of significant changes in the spectra obtained from the surface exposed to H_2O.

Fig. 4.35 shows the O 1s core level spectra for a scraped Y123 sample before (a) and after (b) exposure to water at room temperature. Water adsorption causes a slight shift (0.2 eV) to a higher energy and the growth of the high binding energy peak. The increase in the high binding energy peak can be attributed to the formation of hydroxyl species at the surface or at the grain boundaries as suggested from studies of water-exposed oxide surfaces [269]. The same trend was clear from the spectra of Ba 3d and He II spectra , shown in Fig. 4.36 and 4.37 respectively. As noticed the $Ba3d_{5/2}$ core level is shifted to a higher energy (779.6) as a result of $Ba(OH)_2$ formation. In the valence band region obtained by He II radiation a reduction of the emission around 2.6 eV, an increase in the 9.4 eV peak intensity and a growth of a peak around 7 eV is observed. The growth of the 7 eV peak and the increase in the 9.4 eV peak can also result from hydroxide formation at the surface. The reduction of the 2.6 eV peak can be attributed to the attenuation caused by the hydroxide layer found at the surface [271]. Finally Cu 2p spectrum (Fig. 4.38) shows

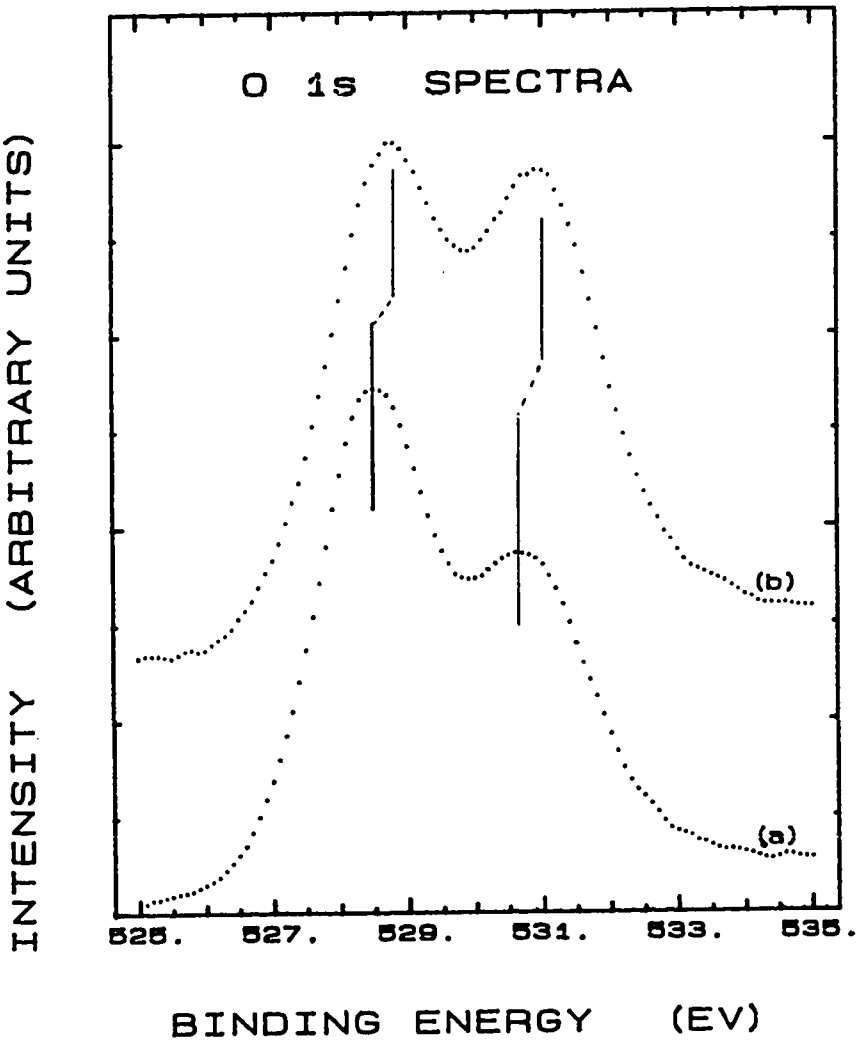

Fig. 4.35 O 1s spectra of a scraped Y123 sample; (a) before exposure to water, and (b) after the exposure.

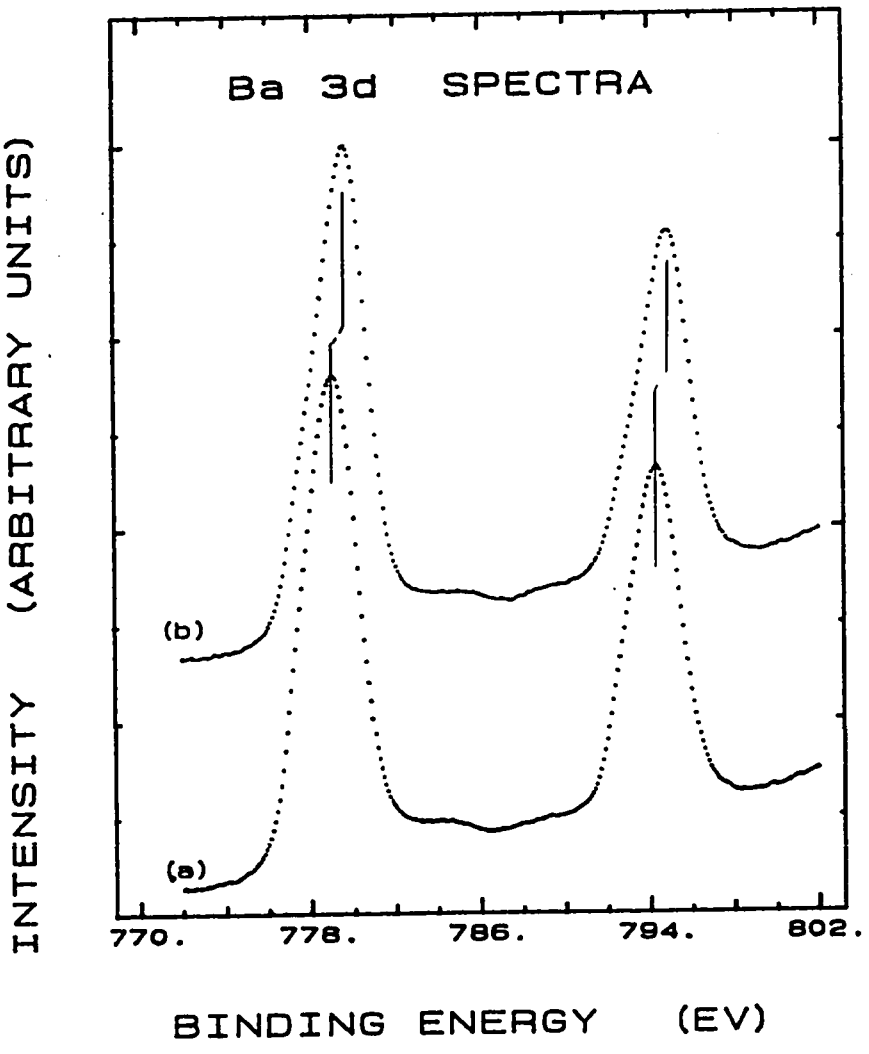

Fig. 4.36 Same as Fig 4.35 except for Ba 3d spectra.

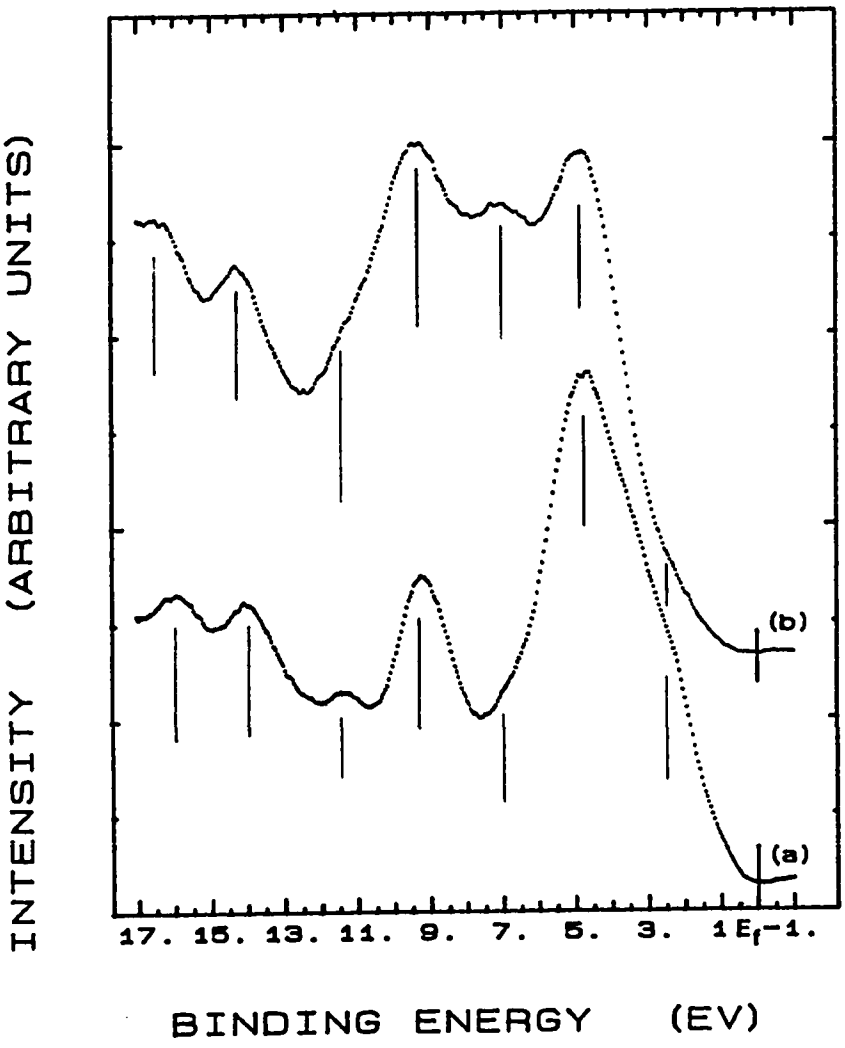

Fig. 4.37 Same as Fig 4.35 except for valence band spectra excited by He-II radiation.

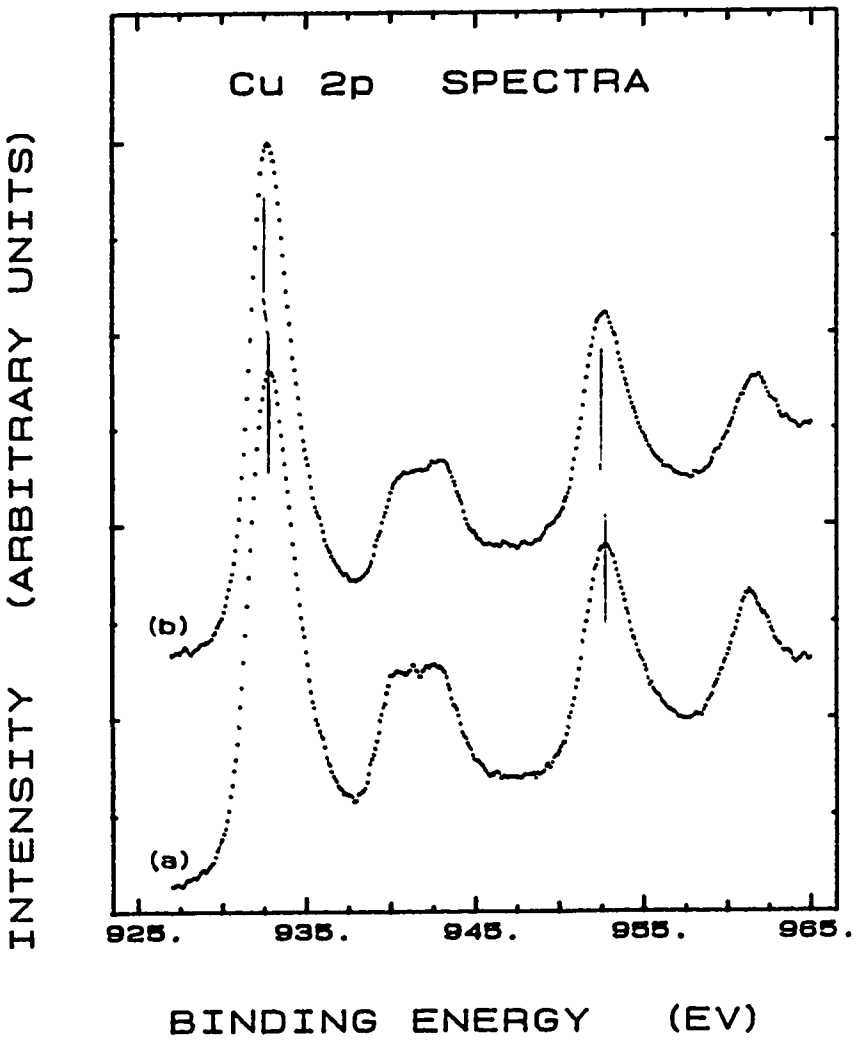

Fig. 4.38 Same as Fig 4.35 except for Cu 2p spectra.

narrowing in the main peak a small shift (0.2 eV) to lower binding energy and reduction in the satellite (I_s/I_m = 30%) compared to the clean surface (I_s/I_m = 38%) indicating the reduction of Cu valency at the surface.

Similar results for O 1s, Ba 3d and He II valence band have been reported [270,271] for samples exposed to water at cryogenic temperatures then warmed up to room temperature.

4.3.3 Oxygen Exposure Effect

Exposure to high purity oxygen was done by transporting the samples from the analysis chamber to the preparation chamber. Oxygen was introduced into the preparation chamber through a leak valve. Freshly scrapped surfaces was exposed to different doses of 1, 10, 100, 1000, 5000 and 10000 L (1L = 1 langmuir = 10^{-6} torr sec) of pure oxygen.

Fig. 4.39 displays different valence band spectra obtained using He II radiation at selected different dosing rates. No significant changes were observed in the different spectra. These observations are consistent with the results reported by other groups [248,271].

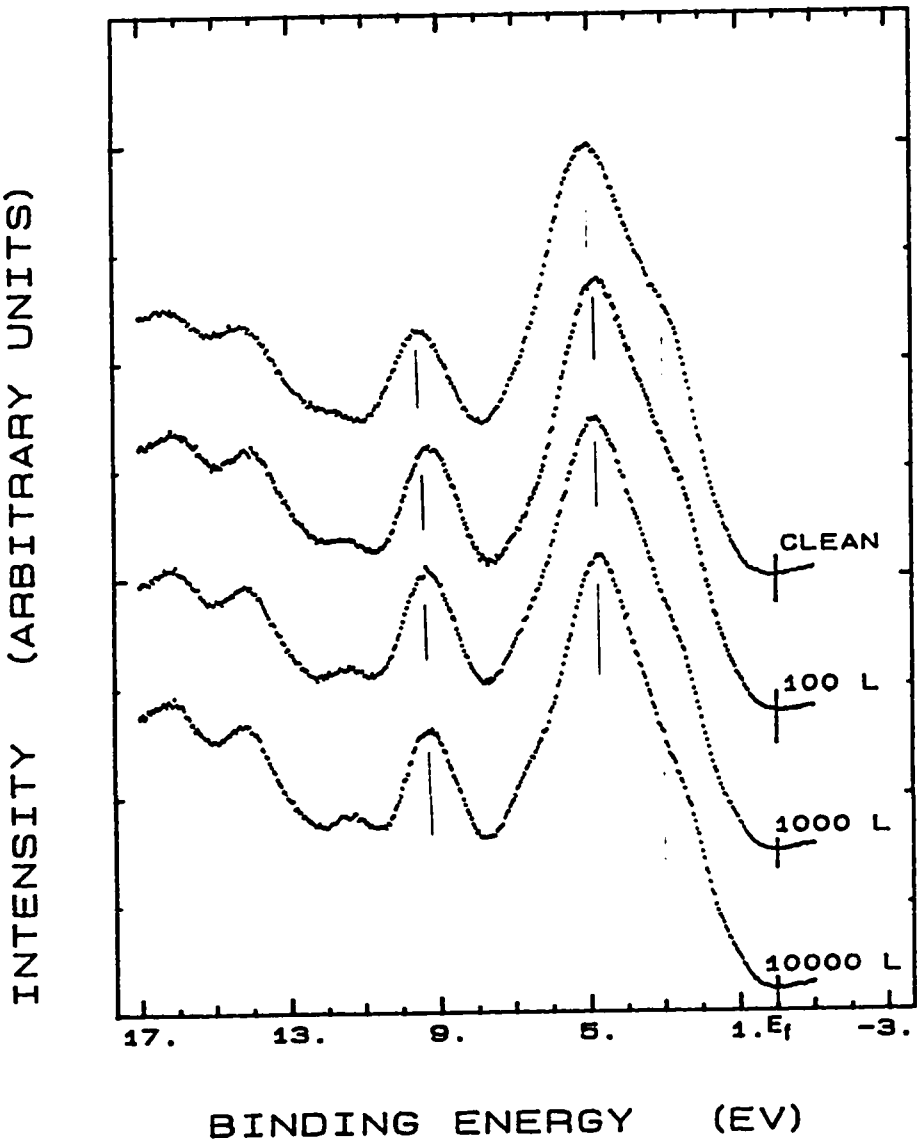

Fig. 4.39 Valence band spectra excited by He-II radiation of a scraped Y123 sample at different dosing rates of oxygen; as indicated.

CHAPTER 5

CONCLUSIONS

Superconductor samples have been prepared using the solid state reaction method and the co-precipitation solid diffusion method from different starting materials. The prepared samples showed a good superconducting properities with a sharp transition ($\Delta T \sim 1K$) and transition temperature $T_c \sim 92$ K. SEM micrographs showed a grainlike homogeneous structure with a preferred orientation along the crystal c axis. XRD patterns confirmed the orthorhomic crystal structure and single phased samples.

Photoemmision spectra showed that sample surface cleaning is necessary, since the as prepared surfaces were contaminated. Representative clean surfaces were obtained by in-situ scraping. However, after a prolonged exposure to UHV, clean surfaces start degrading because of oxygen loss and adsorption of residual contaminants. The clean surface can be regenerated by another in-situ scrapping. This indicate that oxygen is generally desorbed from the surface layer only

which also accumulates contamination from the surrounding media.

From the observed valence band spectra it is possible to conclude that correlation is important in the electronic structure of the Y123 system. This conclusion comes from the very low (much lower than that predicted by band structure calculations) DOS found near the Fermi level and the noticeable shift of the main valence band to higher binding energy.

The main valence band shows two main structures which are strongly hybridized, one around 2.7 eV mainly associated with O 2p character and another around 4.8 eV with mainly Cu 3d character. The very strong mixing of these two states is indicated by insignificant photon energy dependence of the photoemission from the valence band.

The importance of correlation effects was also indicated by the presence of valence band satellite peak around 12.4 eV which was reported to show a resonant behavior at 74 eV photon energy and was attributed to Cu $3d^8$ configuration with a Coulomb correlation energy $U_{dd} \approx 6$ eV. The presence of Cu^{3+} states is ruled out by the large value of this correlation energy.

The 9.4 eV valence band satellite seems to be mainly an intrinsic feature of Y123 superconductor and has an oxygen related origin. It may be attributed to O $2p^4$ configuration related to $3d^{10}\underline{L}^2$ main valance band configuration. However, contributions from contaminant carbon are possible.

Finally, an interpretation of the measured valence band spectra taking their multiple hole structure into account can be done by a cluster CI calculation.

The O 1s line in Y123 high T_c superconductor consists of two main features. The low energy feature results from bulk O^{2-} ions while the high energy component has an intrinsic part originates from hole on oxygen (O^{1-}) and another part comes from contaminations which are mainly carbonates formed at the surface or segregated into the bulk.

The shape and peak position of Cu 2p spectra indicates that the Cu valency is mainly $\leq 2+$. The presence of Cu^{3+} is not detected and is excluded. The separation between the main and satellite peaks leads to U_{dd} value which is in agreement with that estimated from the valence band.

The asymmetric structure observed in the Ba $3d_{5/2}$ line can be interpreted in terms of two different Ba states in the superconductor and a third state comes from the residual contamination at the superconductor. The two different states in the superconductor are due to Ba^{2+} coordinated completely to O^{2-} ions (low energy component) and Ba^{2+} ions with some O^{2-} vacancies (high energy component). The second state is always observed in the surface layer of the superconductor because of oxygen depletion from this layer. This conclusion is supported by the results observed from sample heating in UHV.

The Y 3d core level spectra indicates that Y is present in a single stable bonding configuration in the crystal structure. However, a small amount of unreacted Y_2O_3 seems to be present in the polycrystalline samples as impurities.

In spite of efforts to ensure cleanliness of samples through preparation and transportation carbon 1s transition was found during analysis. It was observed that the intensity of the two peaks is reduced dramatically by scraping but they are still clear. This supports the suggestion that carbon is segregated in the bulk at the grain boundaries.

The Cu(L_3VV) Auger lineshapes for Y123 by their two structures confirm the presence of a major amount of Cu^{2+} single Cu atom after the Auger decay which means that large correlation effects are evident.

Heat treatment results showed that oxygen can be lost readily from the sample surface. However, degradation of superconductivity occurs only at high temperatures where the sample undergoes a phase transition from orthorhombic to tetragonal.

Water exposure results indicated that water reacts dissociatively with high T_c superconductors resulting in the formation of surface hydroxides even at a room temperatures. Hence, high T_c superconductors must be handled carefully and stored in dry inert media to avoid degradation of these materials by atmospheric humidity.

From oxygen exposure experiments, no significant change was

observed at any dosing rate from 1 L to 10,000 L.

For further work, a more ditailed study of the Cu spectra to investigate the role of copper in superconductivity and determine the the proportions of different Cu valencies present in the superconductor is required.

Morcover, since superconductor thin films are the most probable candidates for practical applications, the previous studies can be repeated on thin films prepared by different methods to investigate the effect of different treatments on these thin films.

References

1) H. K. Onnes, Commun. Phys. Lab. Univ. Leiden Nos. 119, 120, 122 (1911).

2) J. File and R. G. Mills, Phys, Rev. Lett. 10, 93 (1963).

3) W. Meissner and R. Ochsenfeld, Naturwissenschaften 21 (1933).

4) H. London and F. London, Physica 2, 341 (1935).

5) A. B. Pippard, Proc. R. Soc. London Ser. A216, 547 (1953).

6) V. L. Ginzburg and L. D. Landau, Zh. Eksp. Teor. Fiz. 20, 1064 (1950).

7) A. A. Abrikosov, Zh. Eksp. Teor. Fiz. 32, 1442, (1957).

8) E. Maxwell, Phys. Rev. 78, 477 (1950).

9) J. Bardeen, L. N. Cooper, and J. R. Schrieffer, Phys. Rev. 106, 162 (1957); 108, 1175 (1957).

10) B. J. Josephson, Phys. Lett. 1, 251 (1962).

11) J. R. Gavaler, Appl. Phys. Lett. 23, 480 (1973).

12) J. G. Bednorz and K. A. Muller, Z. Phys. B64, 189 (1986).

13) R. J. Cava, R. B. van Dover, B. Batlogg, and E. A. Rietman, Phys. Rev. Lett. 58, 408 (1987).

14) C. W. Chu, P. H. Hor, R. L. Meng, L. Gao, and Z. J. Huang, Science 235, 567 (1987).

15) M. L. Wu, J. R. Ashburn, C. J. Torng, P. H. Hor, R. L. Meng, L. Gao, Z. J. Huang, Y. Q. Wang and C. W. Chu, Phys. Rev. Lett. 58, 408 (1987).

16) R. M. Hazen, L. W. Finger, R. J. Angel, C. T. Prewitt, R. L. Ross, C. G. Hadidiacos, P. J. Heaney, D. R. Veblen, Z. Z. Sheng, A. El. Ali, and A. M. Hermann, Phys, Rev. Lett. 60, 1657 (1988).

17) W.E. Pickett, Rev. Mod. phys. 61, 433 (1989).

18) J.D. Jorgensen, B. W. Veal, W. K. Kwok, G. W. Crabtree, A. Umezawa,L. J. Nowicki and A. P. Paulikas, phys. Rev. B36, 5731 (1987).

19) J. M. Tarascon, W. R. McKinnon, P. Barboux, D. M. Hwang, B. G. Bagley, L. H. Greene, G. W. Hull, Y. LePage, N. Stoffel, and M. Giroud, Phys. Rev. B38, 8885 (1988).

20) Z. Z. Sheng, Nature (London) 332, 138 (1988).

21) J. Bok, Solid State Commun. 67, 251 (1988).

22) Y. Tokura, H. Takagi, and S. Uchida, Nature 337, 345 (1989).

23) Y. Tokura, A. Fujimori, H. Matsubara, H. Natabe, H. Takagi, S. Ychida, M. Sakai, H. Ikeda, S. Okuda, and S. Tanaka, Phys, Rev. B39, 9704 (1989).

24) J. C. Fuggle, J. Fink, and N. Nucker, Int. J. Mod. Phys. B1, 1185-1226 (1988).

25) F. Al Shamma, and J.C. Fuggle, Physica C 169, 325(1990).

26) A. S. Davydov, Phys. Reports 190, 191-306 (1990).

27) J. R. Christman, Fundamentals of Solid State Physics, John Wiley and Sons, 1988.

28) C. Kittel, Introduction to Solid State Physics, John Wiley and Sons, 6th Ed., 1986.

29) C. P. Poole, Jr., T. Datta and H. A. Farach, Copper Oxide Superconductors, John Wiley and Sons, 1988.

30) P. Garsche and C. Noguera, MRS Anaheim Symp., 243 (1987).

31) J. B, Boyce, F. Bridges, T. Claeson, T. H. Geballe, C. W. Chu, and J. M. Tarascon, Phys. Rev. B35, 7203 (1987).

32) J. C. Phillips, Phys. Rev. B36, 861 (1987).

33) Z. Wang, N., Zou, J. Pang, and C. Gong, Solid State Commun. 64, 531 (1987).

34) T. Yamashita, A. Kawakami, T. Nishihara, Y. Hirotsu, and M. Takata, Japan. J. Appl. Phys. 26, L635 (1987).

35) T. J. Witt, Phy. Rev. Lett. 61, 1423 (1988).

36) R. H. Koch, C. P. Umbach, G. J. Clark, P. Chaudhari, and R. B. Laibowitz, Appl. Phys. Lett. 51, 200 (1987).

37) C. E. Gough, M. S. Colclough, E. M. Forgan, R. G. Jordan, M. Keene, C. M. Muirhead, A. I. M. Rae, N. Thomas, J. S. Abell, and S. Sutton, Nature 326, 855 (1987).

38) P. Gammel, D. J. Bishop, G. J. Dolan, J. R. Kwo, C. A. Murray, L. F. Schneemeyer, and J. V. Waszczak, Phys. Rev. Lett. 59, 2592 (1987).

39) G. Aeppli, R. J. Cava, E. J. Ansaldo, J. H. Brewer, S. R. Kreitzman, G. M. Luke, D. R. Noakes and R. F. Kiefl, Phys. Rev. B35, 7129 (1987).

40) D. R. Harshman, G. Aeppli, E. J. Ansaldo, B. Batlogg, J. H. Brewer J. F.Carolan, R. J. Cava, M. Celio, A. C. D., Chaklader, W. N. Hardy, S. R. Kreitzman, G. M. Luke, D. R. Noakes, and M. Senba, Phys. Rev. B36, 2386 (1987).

41) J. Niemeyer, M. R. Dietrich and C. Z. Politis, Z. Phys. B67, 155 (1987).

42) J. G. Bednorz and K. A. Mueller, Rev. Mod. Phys. 60, 585 (1988).

43) C. N. R. Rao, Ann. Phys. (Paris) 13, 327 (1988).

44) T. R. Dinger, T. K. Worthingron, W. J. Gallagher, and R. L. Sandstrom, Phys. Rev. Lett. 58, 2687 (1987).

45) T. K. Worthington, W. J. Gallagher and T. R. Dinger, Phys. Rev. Lett. 59, 1160 (1987).

46) U. Walter, M. S. Sherwin, A. Stacy, R. L. Richards, and A. Zettl, Phys. Rev. B35, 532 (1987).

47) A. Kapitulnic, M. R. Beasley, C. Castellani and C. Di Castro, Phys. Rev. B37 (1988).

48) U. Welp, W. K. Kwok, G. W. Crabtree, K. G. Vandervoort and J. Z. Liu, Phys, Rev. Lett. 62, 1908 (1982).

49) R. J. Cava, B. Batlogg, R. B. van Dover, D. W. Murphy, S. Sunshine, T. Siegrist, J. P. Remeika, E. A. Rietman, S. Zahurak, and G. P. Espinosa, Phys. Rev. Lett. 58, 1676 (1987).

50) A. J. Panson, A. I. Braginski, J. R. Gavaler, J. K. Hulm, M. A. Janocko, H. C. Pohl, A. M. Stewart, J. Talvacchio, and G. R. Wagner, Phys. Rev. B35, 8774 (1987).

51) B. Oh, K. Char, A. D. Kent, M. Naito, M. R. Beasley, T. H. Geballe, R. H. Hammond, A. Kapitulnik, and J. M. Graybeal, Phys. Rev. B37, 7861 (1988).

52) D. J. Bishop, P. L. Gammel, A. P. Ramirez, R. J. Cava, B. Batlogg, and E. A. Rietmann, Phys. Rev. B35, 8788 (1987).

53) D. J. Bishop, A. P. Ramirez, P. L. Gammel, B. Batlogg, E. A. Rietmann, R. J. Cava, and A. J. Hills, Phys. Rev. B36, 2408 (1987).

54) W. W. Warren, Jr., R. E. Walstedt, G. F. Brennert, G. P. Espinoza, and J. P. Remeika, Phys. Rev. Lett. 60, 1860 (1987).

55) Z. R. Schlesinger, R. T. Collins, D. L. Kaiser, and F. Holtzberg, Phys. Rev. Lett. 59, 1058 (1987).

56) J. M. Imer, F. Pathey, B. Dardel, W. D. Schneider, Y. Bear, Y. Petroff, and A. Zettl, Phys. Rev. Lett. 62, 336 (1989).

57) B. Batlogg, G. Kourkoulis, W. Weber, R. J. Cava, A. Jayaraman, A. E. White, L. W. Rupp, and E. A. Rietman, Phys. Rev. Lett. 59, 912 (1987).

58) D. E. Morris, R. M. Kuroda, A. G. Markeiz, Phys. Rev. B37, 5936 (1988).

59) C. Thomson, H. Mattausch, M. Bauer, W. Banhofer, R. Liu, L. Genzel, and M., Cardona, Solid State Commu. 67, 1069 (1988).

60) H. Katayama-Yoshida, T. Hirooka, A. Oyamada, Y. Okabe, T. Takahashi, T. Sasaki, A. Ochiai, T. Suzuki, A. J. Mascarenhas, J. I. Pankove, T. F. Ciszek, S. K. Deb, R. B. Goldfarb, and Yongkang, L.I., Physica C156, 481 (1988).

61) A. Fujimari, E. Takayama-Muromachi, Y. Uchida, and B. Okai, Phys. Rev. B35, 8814 (1987).

62) N. Nucker, J. Fink, B. Renker, D. Ewert, C. Politis, J. W. P. Weijs, and J. C. Fuggle, Z. Phys. B67, 9 (1987).

63) P. Steiner, S. Huefner, V. Kinsinger, I. Sander, B. Siegwart, H. Schmitt, R. Schulz, A. Junk, G. Schwitzgebel, A. Gold, C. Politis, H. P. Mueller, R. Hoppe, S. Kemmler-Sack, and C. Kunz, Z. Phys. B69, 449 (1988).

64) R. Tournier, A. Sulpice, P. Lejay, O. Laborde, and J. Beille, J. Magn, Mater, 76-77, 552 (1988).

65) M. E. Reeves, T. A. Friedmann, and D. M. Ginsberg, Phys. Rev. B35, 7207 (1987).

66) B. D., Dunlap, M. V. Nevitt, M. Slaski, T. E. Klippert, Z. Sungaila, A. G. McKale, D. W. Capone, R. B. Poeppel, and B. K. Flandermeyer, Phys. Rev. B35, 7210 (1987).

67) L. E. Wenger, J. T. Chen, G. W. Hunter, and E.M. Logothetis, Phys. Rev. B35, 7213 (1987).

68) S. von Molnar, A. Torressen, D. Kaiser, F. Holtzberg, and T. Penney, Phys. Rev. B37, 3762 (1988).

69) S. L. Cooper, M. V. Klein, B. G. Pazol, J. P. Rice, and D. M. Ginsberg, Phys. Rev. B37, 5920 (1988).

70) D. A. Bonn, J. E. Greedan, C. V. Stager, T. Timusk, M. G. Doss, S. L. Herr, K. Kamaras, C. D. Porter, D. B. Tanner, J. M. Tarascon, W. R. McKinnon, and L. H. Greene, Phys. Rev. B35, 8843 (1987).

71) D. A. Bonn, J. E. Greedan, C. V. Stager, T. Timusk, M. G. Doss, S. L. Herr, K. Kamaras, C. D. Porter, D. B. Tanner, J. M. Tarascon, W. R. McKinnon, and L. H. Greene, Phys. Rev. B37, 1547 (1988).

72) W. Ose, P. E. Obermayer, H. H. Otto, T. Zetterer, H. Lengfellner, N. Tasler, J. Keller, and K. F. Renk, Physica C153-155, 639 (1988).

73) P. W. Anderson, Science 235, 1196 (1987).

74) G. Baskaran, Z. Zou, P. W. Anderson, Solid State Commu. 63, 973 (1987).

75) P. W. Anderson, G. Baskaran, Z. Zou, and T. Hsu, Phys. Rev. Lett. 58, 2790 (1987).

76) P. W. Anderson, G. Baskaran, Z.Zou, J. Wheatley, T. Hsu, B. S. Shastry, B. Doucot, and S. Liang, Physica C153-155, 527 (1988).

77) W. Webber, Phys. Rev. Lett. 58, 1371 (1987).

78) P. Fulde, Physica C153-155, 1769 (1988).

79) J. R. Schrieffer, X.-G. Wen and S.-C. Zhang, Physica C153-155, 21 (1988).

80) C. M. Varma, S. Schmit-Rink, and E. Abrahams, Solid State Commu. 62, 681 (1987).

81) S. Robaszkiewicz, R. Micans, and J. Ranninger, Phys. Rev. B36, 180 (1987).

82) V. J. Emery, Phys. Rev. Lett. 58, 2794 (1987).

83) J. E. Hirsh, Phys. Rev. B35, 8726 (1987).

84) D. H. Lee, and J. Ihm, Solid State Commu. 62, 811 (1987).

85) Z. Zau and T. C. Hsu, Mod. Phys. Lett. B2, 939 (1988).

86) H. Chi, and A. D. S. Nagi, Solid State Commu. 65, 1563 (1988).

87) W. Weber, Z. Phys. B70, 323 (1988).

88) D. A. Cardwell, and N. M. Shorrocks, Phys. Rev. B40, 6564 (1989).

89) M. Frick, and T. Schneider, Z. Phys. B78, 159 (1990).

90) Y. Takahashi, Z. Phys. B78, 199 (1990).

91) M. Crisan, and D. Vacaru, Z. Phys. B78, 213 (1990).

92) L. C. Bourne, M. F. Crommie, A. Zettl, H. C. Zurloye, S. W. Keller, K. L. Leary, A. M. Stacy, K. J. Chang, M. L. Cohen, and D. E. Morris, Phys. Rev. Lett. 58, 2337 (1987).

93) W. Hang-Sheng and W. Zheng-yu, Solid State Commu. 63, 269 (1988).

94) A. Mawdsley, H. J. Trodahl, J. Tallon, J. Sarfati, and A. B. Kaiser, Nature 328, 233 (1987).

95) R. A. Zacher, Phys. Rev. B36, 7115 (1987).

96) L. F. Mattheiss and D. R. Hamann, Solid State Commu. 63, 395 (1987).

97) Y. Okabe, Y. Sugumura, T. Sasaki, and H. Katayama-Yoshida, Solid State Commu. 64, 483 (1987).

98) Yu BN. Gaididei and V. M. Loktev, Phys. Status Solidi B147, 307 (1988).

99) F. Marsiglio and J. P. Carbotte, Solid State Commu. 63, 419 (1987).

100) I. Bozovic, D. Kirillov, A. Kapitulnik, K.Char, M. R. Hahn, M. R. Beasley, T. H. Gebatlle, Y. H. Kim, and A. J. Heeger, Phys. Rev. Lett, 59, 2219 (1987).

101) F. Marsiglio and J. P. Carbotte, Phys. Rev. B36, 3937 (1987).

102) Y. Guo, J. M. Langlois, and W. A. Goddard, Science 239, 896 (1988).

103) K. Hida, J. Phys. Soc. Jpn. 57, 1544 (1988).

104) P. Prelovsek, Phys. Lett. A126, 287 (1988).

105) E. Y. Loh, T. Martin, and P. Prelovsek, Phys. Rev. B38, 2494 (1988).

106) Y. Chang, M. Onellion, D. W. Niles, R. Joynt, G. Margaritondo, N. G. Stoffel, and J. M. Tarascon, Solid State Commu. 63, 717 (1987).

107) J. Ruvolds, Phys. Rev. B35, 8869 (1987).

108) V. Z. Kresin, J. Mater. Res. 2, 793 (1987).

109) V. Z. Kresin, Solid State Commu. 63, 725 (1987), and Phys. Rev. B35, 8716 (1987).

110) V. Z. Kresin, and Morawitz, Physica C153-155, 1327 (1988).

111) S. Perkowtiz, Solid State Commu. 64, 721 (1987).

112) Z. Schlesinger, R. L. Greene, J. G. Bednorz, and K. A. Mueller, Phys. Rev. B35, 5334 (1987).

113) Y. Kuramoto and T. Watanabe, Solid State Commu. 63, 821 (1987).

114) A. S. Alexandrov, Phys. Rev. B38, 925 (1988).

115) L. J. deJongh, Solid State Commu. 65, 961 (1988), and Physica C152, 171 (1988).

116) H. Zhengh, Phys. Rev. B 38, 11865 (1988).

117) A. Bussmann-Holder, A. Simon, and H. Buettner, Phys. Rev. B 39, 207 (1989).

118) A.S. Alexandrov, Physica C 158, 273 (1989).

119) S. Mazumdar, Phys. Rev. B36, 7190 (1987) and Phys. Rev. Lett. 59, 26171 (1987).

120) J. A. Wilson, J. Phys. C:Solid State Phys. 20, L911 (1987).

121) R. F. Wood and M. A. Abdel-Raouf, Solid State Commu. 74, 371 (1990).

122) H. Kamimura, S. Matsuno and R., Saito, Solid State Commu. 67, 363 (1988).

123) R. F. Wood, M. Mostoller, and J. F. Cooke, Physica C 165, 97 (1990).

124) K. Yuon and M. Francois, Z. Phys. B76, 413 (1989).

125) R. Beyers and T. M. Shaw, Solid State Phys. 42, 135 (1989).

126) R. J. Cava, B. Batlogg, R. B. van Dover, D. W. Murphy, S. Sunshine, T. Siegrist, J. P. Remeika, E. A. Rietman, Z. Zahurak, and G. P. Espinosa, Phys. Rev. Lett 58, 1676 (1987).

127) P. M. Grant, R. B. Beyers, E. M. Engler, G. Lim, S. S. Parkin, M. L. Ramirez, V. Y. Lee, A. Nazzal, J. E. Vazquez, and R. J. Savoy, Phys. Rev. B35, 7242 (1987).

128) W. R. McKinnon, J. M. Tarascon. L. H. Greene, G. W. Hull, and D. A. Huang, Phys. Rev. B35, 7245 (1987).

129) W. J. Gallaghar, R. L. Sandstrom, T. R. Dinger, T. M. Shaw, and D. A. Chance, Solid State Commun. 63, 147 (1987).

130) D. G. Hinks, L. Soderholm, D. Capponc II, J. D. Jorgensen, and I. K. Schuller, Appl. Phys. Lett. 50, 1688 (1987).

131) E. Takayama, Muromachi, Y. Uchida, Y. Matsui, and K. Kato, Jpn. J. Appl. Phys. 26, 476 (1987).

132) Y. Syono, M. Kikuchi, K. Oh-Ishi, K. Hiraga, H. Arai. Y. Matsui, N. Kobayashi, T. Sasaoka, and Y. Muto, Jpn. J. Appl. Phys. 26, L498 (1987).

133) S. B. Qadri, L. E. Toth, M. Osofshy, S. Lawrence, D. U. Gubser, and S. A. Wolf, Phys. Rev. B35, 7235 (1987).

134) T. Siegrist, S. Sunshine, D. W. Murphy, R. J. Cava and S. M. Zahurak, Phys. Rev. B35, 7137 (1987).

135) F. Beech, S. Miraglia, A. Santoro, and R. S. Roth, Phys. Rev. B35, 8778 (1987).

136) M. A. Beno, L. Soderholm, D. W. Capone II, D. G. Hinks, J. D. Jorgensen, J. D. Grace, and I. K., Schuller, Appl. Phys. Lett. 51, 57 (1987).

137) W. David, W. Harrison, J. Gunn, O. Moze, A. Soper, P. Day, J. D. Jorgensen, D. Hinks, M. A. Beno, L. Soderholm, D. Capone II, I. K. Schuller, C. Segre, K. Zhang, and J. D. Grace, Nature (London) 327, 310 (1987).

138) M. Francois, E. Walker, J. Jorda, K. Yuon, and O. Fischer, Solid State Commun. 63, 1149 (1987).

139) J. E. Greedan, A. H. O'Reilly, and C. V. Stager, Phys. Rev. B35, 8770 (1987).

140) J. D. Jorgensen, M. A. Beno, D. G. Hinks, L. Soderholm, K. J. Volin, R. L. Hitterman, J. D. Grace, I. K. Schuller, C. V. Segre, K. Zhang, and M. S. Kleefisch, Phys. Rev. B36, 3608 (1987).

141) B. Rupp, P. Fischer, E. Porschke, R. Arons, P. Meuffels, Physica C 156, 559 (1988).

142) W. Schafer, E. Jansen, G. Will, J. Faber, B. Veal, Mater. Res. Bull. 23, 1439 (1988).

143) A. Sequeira, H. Rajagopal, and J. V. Yakhmi, Solid State Commun. 65, 991 (1988).

144) D. E. Cox, A. R. Moodenbaugh, J. J. Hurst, and R. H. Jones, J. Phys. Chem. Solids, 49, 47 (1988).

145) M. Francois, A. Junod,K. Yuon, A. Hewat, J. Capponi, P. Strobel, M. Marezio, and P. Fischer, Solid State Commun. 66, 1117 (1988).

146) A. Williams, G. H. Kwei, R. B. Von Dreele, A. C. Larson, I. D. Raistrick, and D. L. Bish, Phys. Rev. B37, 7960 (1988).

147) G. Calestani and C. Rizzoli, Nature 328, 606 (1987).

148) G. Roth, B. Renker, G. Heger, M. Herviеu, B. Domenges, and B. Raveau. Z. Phys. B69, 53 (1987).

149) S. Sato, I. Nakada, T. Kohara, and Y. Oda, Acta Crystallogr. C44, 11 (1988).

150) A. W. Hewat, J. J. Capponi, C. Chaillout, M. Marezio, and E. A. Hewat, Solid State Commun. 64, 301 (1987).

151) Q. W. Yan, P. Zhang, Z. Shen, J. Zhao, Y. Ren, Y. Wei, C. Liu, T. Ning, K. Sun, and S. Niu, Phys. Rev. B37, 5845 (1988).

152) A. Santro, S. Miraglia, F. Beech, S. Sunshine, D. W. Murphy, L. F.

Schneemeyer, and J. Waszczak, Mater. Res. Bull. 22, 1007 (1987).

153) R. Beyers, G. Lim, E. M. Engler, R. J. Savoy, T. M. Shaw, T. R. Dinger, W. J. Gallagher, and R. L. Sandstorm, Appl. Phys. Lett. 50, 1918 (1987).

154) G. Van Tendeloo, H.W. Zandbergen, and S. Amelinckx, Solid State Commun. 63, 603 (1987).

155) I. K. Schuller, D. G. Hinks, M. A. Beno, D. W. Capone II, L. Soderholm, J. P. Locquet, Y. Bruynseraede, C. U. Segre, and K. Zhang, Solid State Commun. 63, 385 (1987).

156) R. Beyers, G. Lim, E. M. Engler, V. Y. Lee, M. L. Ramirez, R. J. Savoy, R. D. Jacowitz, T. M. Shaw, S. LaPlaca, R. Boehme, C. C. Tsuei, S. I. Park, M. W. Shafer, and W. J. Gallagher, Appl. Phys. Lett. 51, 614 (1987).

157) P. K. Gallagher, H. M. O'Bryan, S. A. Sunshine, and D. W. Murphy, Mater. Res. Bull. 22, 995 (1987).

158) P. P. Freitas and T. S. Plaskett, Phys. Rev. B36, 5723 (1987).

159) E. D. Specht, C. J. Sparks, A. Dhere, J. Brynestad, O. Cavin, D. Kroeger, and H. Oye, Phys. Rev. B37, 7426 (1988).

160) S. Massida, J. Yu, A. J. Freeman, and D. D. Koelling, Phys. Lett. A122, 198 (1987).

161) W. Y. Ching, Y. Xu, G. L. Zhou, K. W. Wong, and F. Zandiehnadem, Phys. Rev. Lett. 59, 1333 (1987).

162) F. Herman, R. V. Kasowski, and W. Y. Hsu, Phys. Rev. B36, 6904 (1987) and Phys. Rev. B38, 204 (1988).

163) W. T. Temmerman, G. M. Stocks, P. J. Durham, and P.A. Sterne, J. Phys. F; Met. Phys. 17, L135 (1987).

164) Y. Xu, W. Y. Ching, and K. W. Wong, Phys. Rev. B37, 9773 (1988).

165) B. A. Richert and R. E. Allen, Phys, Rev. B37, 7869 (1988).

166) H. Krakauer, W. E. Pickett, and R. E. Cohen, J. Supercond. 1, 111 (1988).

167) K. T. Park, K. Terakura, T. Oguchi, A. Yanase, and M. Ikeda, J. Phys. Soc. Jpn. 57, 3445 (1988).

168) W. A. Harrison :Electronic Structure and Properties of Solids, W. H. Freeman and Co., San Francisco, 1980.

169) B. Feuerbacher, B. Fitton and R. F. Willis, Editors, Photoemission and the Electronic Properties of Surfaces, Wiley, N.Y. (1978).

170) M. Cordona and L. Ley, Editors, Photoemission in Solids, Springer-Verlag, Berlin, Vols. 1 and 2, (1978).

171) C. S. Fadley, Review in Electron Spectroscopy: Theory, Techniques and Applications, C. R. Brundle and A. D. Baker, Editors, Academic Press, London, Vol. 2, Ch.1, (1978).

172) C. S. Fadley, Review of Angle Resolved X-ray Photoelectron Spectroscopy (in progress), Surf. Sci., edited by S. G. Davidson, Pergamon Press, New York, 16 (1985), No.3.

173) A. Einstein, Ann. Phys. 17, 132, (1905), Springer, Berlin, (1981).

174) C. S. Fadley, Basic Concept of X-ray Photoelectron Spectroscopy, in Electron Spectroscopy: Theory, Techniques and Applications, C. R. Brundle and A. D. Baker, Editors, Academic Press, London, Vol. 2, (1978).

175) A Modern Photoelectron Spectrometer With Multi-Techniques Surface Analysis Capability. A report prepared by Electron Spectroscopy Group in Department of Physics, University of Petroleum and Minerals, Dhahran, Kingdom of Saudi Arabia, (1986).

176) C. E. Kuyatt and J. A. Simpson, Rev. Sci. Instrum, 38, 103 (1967).

* M. P. Seah, Review in Surf. Interface Anal., 2, 222 (1980).

* C. S. Fadley, Review in Electron Spectroscopy: Theory, Techniques and Applications, C. R. Brundle and A. D. Baker, Editors, Academic Press, London, Vol. 2, Ch.1, (1978).

* R. C. G. Leckey, J. Electron Spectrosc. Related Phenom., 43, 183 (1987).

177) D. Briggs and P. M. Seah, Practical Surface Analysis by Auger and X-ray Photoelectron Spectroscopy, John Wiley & Sons, Chichester, U.K., (1983).

178) M.T.Anthony and P. M. Seah, Surface Interface Anal. 6, 95(1984).

179) D. A. Shirley, in: Photoemission in Solids I, Ch. 4, Springer, Berlin (1978).

180) H. Verweij, Solid State Commun. 64, 1213 (1987).

181) T. Takahashi, F. Maeda, H. Katayama-Yoshida, Y. Okabe, Y. Suzuki, A. Fujimori, S. Hosoya, S. Shaamoto, and M. Sato, Phys. Rev. B 37, 9788 (1987).

182) J. Halbritter, P. Walk, H.-J. Mathes, B. Haeuser, and H. Rogalla, Z. Phys. B 73, 2771 (1988).

183) A. D. Shirley, Phys, Rev. B 5, 4709, (1972).

184) A. Proctor and Sherwood PMA, Analytical Chemistry 54, 13 (1982).

185) A. Savitzky and Golay MJE, Anal. Chem. 36, 1627-1639 (1964), corrected in: J. Steiner, Y. Termonia and J. Deltour, Analytical Chemistry 44, 1906-1909 (1972).

186) A. Proctor and Sherwood PMA, Analytical Chemistry 52, 2315-2321 (1980).

187) Z. Shen, J. W. Allen, J. J. Yeh, J.-S. Kang, W. Ellis, W. Spicer, I. Lindau, M. B. Maple, Y. D. Dalichouch, M. S. Torikachvili, J. Z. Sun, and T. H. Geballe, Phys. Rev. B36, 8414 (1987).

188) N. G. Stoffel, J. M. Tarascon, Y. Chang, M. Onellion, D. W. Niles, and G. Margaritondo, Phys. Rev. B36, 7, 3986 (1987).

189) N. G. Stoffel, Y. Chang, H. K. Kelly, L. Dottl, M. Onellion, P. A. Morris, W. A. Bonner, and G. Margaritondo, Phys. Rev. B37, 7952 (1988).

190) T. Takahashi, F. Maeda, H. Arai, H. Katayama-Yoshida, Y. Okabe, T. Suzuki, S. Hosoya, A. Fujimori, T. Shidara, T. Koide, T. Miyahara, M. Onoda, Shamoto and M. Sato Phys. Rev. B36, 10, 5686 (1987).

191) M. Tang, N. G. Stoffel, Q. B. Chen, D. LaGraffe, P. A. Morris, W. A. Bonner, G. Margaritondo, and M. Onellion, Phys. Rev. B38, 1, 897 (1988).

192) P. Steiner, V. Kinsinger, I. Sander, B. Siegwart, S. Hufner, C. Poilitis, Z. Phys. B67, 19, (1987).

193) P. D. Johnson, S. L. Qiu, L. Jiang, M. W. Ruckman, M. Strongin, S. L. Hulbert, R. F. Garrett, B. Sinkovic, N. V. Smith, R. J. Cara, C. S. Jee, D.Nichols, E., Kaczanowicz, R. E. Salomon, and J. E. Crow, Phys. Rev. B35, 16, 8811 (1987).

194) Z. Iqbal, E. Leone, R. Chin, A. J. Signorelli, A. Bose, and H. Eckhardt, J. Mater. Res. 2 (6),768 (1987).

195) D. Van der Marel, J. Van Elp, G. A. Sawatzky, and D. Heitmann, Phys. Rev. B37 (10), 5136 (1988).

196) A. Samsavar, T. Miller, T.-C. Chiang, B. G. Pazol, T. A. Friedmann and D. M. Ginsberg, Phys. Rev. B37 (10), 5164 (1988).

197) J. A. Yarmoff, D. R. Clarke, W. Drube, U. O. Karlsson, A. Taleb-Ibrahimi and F. J. Himpsel, Phys. Rev. B36 (6), 3967 (1987).

198) E. Z. Kurmaevand and L. D. Finkelstein, Int. J. Mod, Phys. B3 (7), 973 (1989).

199) P. Steiner, S. Hufner, A. Jungmann, V. Kinsinger, and I. Sander, Z. Phys. B74, 173 (1989).

200) R. G. Egdell, W. R. Flavell, and M. S. Golden, Supercond. Sci. Technol. 3, 8 (1990).

201) A. J. Arko, R. S. List, R. J. Bartlett, S.-W. Cheong, Z. Fisk, J. D. Thompson, C. G. Olson, A.-B.Yang, R. Liu, C. Gu, B. W. Veal, J. Z. Liu, A. P. Paulikas, K. Vandervoort, H. Claus, J. C. Campuzano, J. E. Schriber, and N. D. Shinn, Physica Scriptra T31, 282 (1990).

202) T. J. Wagener, Y. Gao, H. M. Meyer III, I. M. Vitomirov, C. M. Aldao, D. M. Hill, J. H. Weaver, B. Fladermeyer, and D. W. Capone II, AIP Conf. Proc. 165, 368 (1988),

203) Y. Sakisaka, T. Komeda, T. Maruyama, M. Onchi, H. Kato, Y. Aiura, H. Yanashima, T. Terashima, Y. Bando, K. Iijima, K. Yamamoto, and K. Hirata, Phys, Rev. B39 (4), 2304 (1989).

204) R. S. List, A. J. Arko, R. J. Bartlett, C. G. Olson, A.-B. Yang, R. Liu, C. Gu, B. W. Veal, J. Z. Liu, K. Vandervoort, A. P. Paulikas, and J. C., Campuzano, J. Mag. Mater. 81, 151 (1989).

205) J. M. Mariot, V. Barnole, C. F. Haque, G. Vetter and F. Queyroux, Z. Phys. B75, 1 (1989).

206) A. J. Arko, R. S. List, R. J. Bartlett, S.-W. Cheong, Z. Fisk, J. D. Thompson, C. G. Olson, A.-B.Yang, R. Liu, C. Gu, B. W. Veal, J. Z. Liu, A. P. Paulikas, K. Vandervoort, H. Claus, J. C. Campuzano, J. E. Schriber, and N. D. Shinn, Phys, Rev. B40 (4), 2268 (1989).

207) K. Soda, T. Mori, T. Ishil, K.T. Park, K. Terakura, T. Takabatake,

and M. Isikawa, Physica C 161, 219 (1989).

208) R. L. Kurtz, AIP Conf. Proc. 165, 222 (1988),

209) J. Redinger, J. Yu, A. J. Freemann, S. Massidda, Phys, Lett A 124 (8), 469 (1987).

210) M. Onellion, Y.Chang, D. Nils, R. Joynt, G. Margaritondo, N. G. Stoffel, and J. M. Tarascon, Phys. Rev. B36, 819 (1987).

211) C. Calandra, F. Manghi, and T. Minerva, Physica C 165, 461 (1990).

212) L. E. Matheiss and D. R. Hamann, Solid State Commu. 63, 395 (1987)

213) S. Massidda, J. Yu, A. J. Freeman, D. D. Koelling, Phys. Lett A 122, 198 (1987).

214) J.J. Yeh and I. Landau, Atomic Data and Neuclear Data Tables 32, 1(1985).

215) A. Fujimori, Solid State Commu. 63, 857 (1987).

216) F. J. Himpsel, G. V. Chandrashekhar, A. Taleb-Ibrahimi, A. B. McLean, and M. W. Shafer, AIP Conf. Proc. 182, 289 (1989).

217) D. Majumdar, D. Chatterjee, and G. Pav-Pujalt, Physica C 158, 413 (1989).

218) G. Wiendin, J. de Physique, Colloq. C 9, 48, 1157 (1987).

219) P. Adler, H. Buchkremer-Hermanns, and A. Simon, Z. Phys. B 81, 355 (1990).

220) W. R. Flavell and R. G. Egdell, Supercond. Sci. Technol. 1, 118 (1988).

221) H. Ihana, M. Jo, N. Tevanda, M. Hirabayashi, H. Oyangi, K. Murata, Y. Kimura, R. Sugise, I. Hayashida, S. Ohashi, and M. Akimoto, Physica C 153-155, 131 (1988).

222) B. Dauth, P. Sen, B. Rupp, W., Gudat, Ch. Ziegler, and W. Gopel, Z. Phys. B79, 169, (1990).

223) T. Gouricux, G. Krill, M. Maurer, M. F. Ravet, A. Menny, H. Tolentino, and A. Fontaine, Phys. Rev. B37, 13, 7516 (1988).

224) B. Dauth, T. Kachel, P. Sen, and K. Fischer, Z. Phys. B68, 407

(1987).

225) D. E. Ramaker, in "Thin Film Processing and Characterization of High Temperature Superconductors" (J. M. E. Harper, R. J. Colton and L. C. Feldman, eds.), AIP Conf. Proc. No.165, p.284, AIP, New York, (1988).

226) J. H. Weaver, H. M. Meyer III, T. J. Wagener, Phys, Rev. B38, 4668 (1988).

227) J. W. Rogers, Phys. Rev. B38, 5021 (1988).

228) Y. Dai, Phys. Rev. B38, 5091 (1988).

229) C.D.Wagner, Handbook of X-ray Photoelectron Spectroscopy,(1 ed. G.E. Muilenberg,(1979).

230) G. Van der Laan, C. Westra, C. Haas, and G. A. Sawatzky, Phys. Rev. B23, 4362 (1981).

231) J. C. Klein, C. P. Li, D. M. Hercules, and J. F. Black, Appl. Spect. 38 (5), 729 (1984).

232) A. Fujimori, E. Takayama-Muromachi, Y. Uchida, and B. Oki, Phys. Rev. B35, 8814 (1987).

233) L. C. Davis, J. Appl. Phys. 59, R25 (1986).

234) A. Bianconi, A. Congiu Castellano, M. DeSantis, P. Delogu, A. Gargano, and Giorgi, Solid State Commu. 63, 1135 (1987).

235) N. G. Stoffel, P. A. Morris, W. A. Bonner, D. LaGraffe, M. Tang, Y. Chang, G. Margaritondo, and M. Onellion, Phys. Rev. B38, 213 (1988).

236) D. E. Ramaker, N. Turner, J. Murday, L. Toth, M. Osofsky, and F. Huston, Phys. Rev. B36, 5672 (1987).

237) A. Rosebewaig and G. K. Wertheim, J. Electron Spectrosc. Relat. Phenom. 1, 493 (1972).

238) G. Van der Lann, J. Zaonen and G. A. Sawatzky, Phys, Rev. B 33, 4253 (1986).

239) A. Bianconi, Int. J. Mod. Phys. B 1, 205 (1987).

240) J.-M. Mariot, V. Barnole, C. Hague, V. Geiser, and H.-J. Guntherodt, Solid State Commu. 64, 1203 (1987).

241) Ch. Ziegler, G. Frank, and W. Goepl, Z. Phys. B81, 349 (1990).

242) X. D. Wu, A. Inam, M. S. Hegde, T. Venkatesan, C. C. Chang, E. W. Chase, B. Wilkens, and J. M. Tarascon, Phys. Rev. B 38, 9307 (1988).

243) F. Werfel, M. Heinonen, and E.Suoninen, Z. Phys. B70, 317 (1988).

244) H. M. Meyer III, D. M. Hill, T. J. Wagener, and J. H. Weaver, J. Appl. Phys. 65 (8), 3130 (1989).

245) C. C. Chang, M. S. Hegde, X. Wu, B. Dutta, A. Inam, T. Venkatesan, B. J. Wilkens, and J. B. Wachtman, Jr., Appl. Phys. Lett. 55 (16), 1680 (1989).

246) C. C. Chang, M. S. Hegde, X. Wu, B. Dutta, A. Inam, T. Venkatesan, B. J. Wilkens, and J. B. Wachtman, Jr., J. Appl. Phys. 67, (12), 7483 (1990).

247) H. M. Meyer III, D. M. Hill, T. J. Wagener, Y. Gao, J. H. Weaver, D. W. Capone, and K.C. Goretta, Phys. Rev. B38 (10), 6500 (1988).

248) S. Myhra, P. R. Chalker, P. T. Moseley, and J. C. Riviere, Physica C 165, 270 (1990).

249) Y. Fukuda, M. Nagoshi, T.Suzuki, Y. Namba, Y. Syono, and M. Tachiki, Phys. Rev. B39 (16), 11494 (1989).

250) R. Liu, C. G. Olson, A.-B. Yang, C. Gu, P. W. Lynch, A. J. Arko, R. S. List, R. J. Bartlett, Phys. Rev. B40 (4), 2650 (1989).

251) A. G. Schratt, S. L. Cohen, T. R. Dinger, F. J. Himpsel, J. A. Yarmoff, K. G. Frase, S. I. Park, and R. Purtell, AIP Conf. Proc. 165, 349 (1988).

252) H. M. Meyer III, Y. Gao, T. J. Wagener, D. M. Hill, J. H. Weaver, B. K. Flandermeyer,and D. W. Capone II, AIP Conf. Proc. 165, 254 (1988).

253) D. C. Miller, D. E. Fowler, C. R. Brundle, and W. Y. Lee, AIP Conf. Proc. 165, 336 (1988).

254) F. Stuckl, P. Bruesch, and T. Baumann, Physica C 153, 200 (1988).

255) D. E. Fowler, C. R. Brundle, J. Lerczak, and F. Holtzberg, Physica C 162-164, 1303 (1989).

256) R. P. Vasquez, B. D. Hunt, dand M. C. Foote, Appl. Phys. Lett. 53

(26), 2692 (1988).

257) R. P. Vasquez, M. Foote, and B. Hunt Appl. Phys. Lett. 54, 1060 (1989).

258) H. Guyot, L. Schmidt, R. Cinti, P. L. Reydet, and J. Marcus, Physica C 162-164, 1305 (1989).

259) J. Halbritter, P. Walk, H.-J. Mathes, B. Haeuser, H. Rogalla, Physica C 153-155, 127 (1988).

260) H. Van Doveren, and J. A. TH. Verhoeren, J. Electron, Spec. Relat. Phenom. 21, 265 (1980).

261) M. F. Koenig and J. T. Grant, Appl. Surf. Sci. 20, 481 (1985).

262) W. V. Lampert, K. D. Rachocki, B. C. Lamartine, and T. W. Haas, J. Electron, Spec. Relat. Phenom. 26, 133 (1982).

263) H. Fjellvage, P. Karen, A. Kjekshus, and J. Grepstad, Solid State Commu. 64, 917 (1987).

264) M. Cini, Solid State Commu. 20, 605 (1976).

265) G. A. Sawatzky, Phys. Rev. Lett. 39, 504 (1977).

266) S. Larrson and M. Graga, Chem. Phys. Lett. 48, 596 (1977).

267) A. Balzarotti, M. De Crescenzi, N. Motta, F. Patella, and A. Sgarlata, Phys. Rev. B38, 6461 (1988).

268) W. K. Ford, C. T. Chen, J. Anderson, J. Kwo, S. H. Liou, M. Hong, G. V. Rubenacker, and J. E. Drumheller, Phys. Rev. B37, 7924 (1988).

269) P. A. Thiel, and T. E. Madey, Surf. Sci. Rep. 7, 211 (1987).

270) S. L. Qiu, M. W. Ruckman, N. B. Brookes, P. D. Johnson, J. Chen, C. L. Lin, and M. Strongin, Phys. Rev. B37, 3747 (1988).

271) R. L. Kurtz, R. Stockbauer, T. Madey, D. Mueller, A. Shih, and L. Toth, Phys. Rev. B37, 7936 (1988).

272) J. Kirz, D. Attwood, B. Henke, M. Howells, K. Kennedy, K. Kim, J. Kortright, R. Perera, P. Pianetta, J. Riordan, J. Scofield, G. Stradling, A. Thompson, J. Underwood, D. Vaughan, G. Williams, and H. Winick, X-ray Data Booklet, (1985).